

**CZECH TECHNICAL
UNIVERSITY
IN PRAGUE**

**FACULTY
OF MECHANICAL
ENGINEERING**



**MASTER' S
THESIS**

2018

**MICHAL
HAUBNER**



MASTER'S THESIS ASSIGNMENT

I. Personal and study details

Student's name: **Haubner Michal** Personal ID number: **397050**
Faculty / Institute: **Faculty of Mechanical Engineering**
Department / Institute: **Department of Instrumentation and Control Engineering**
Study program: **Mechanical Engineering**
Branch of study: **Instrumentation and Control Engineering**

II. Master's thesis details

Master's thesis title in English:

Commissioning of a vacuum system for measurements of electron stimulated desorption at cryogenic temperatures

Master's thesis title in Czech:

Zprovoznění vakuové aparatury pro měření elektronově stimulované desorpce za kryogenních teplot

Guidelines:

1. Write a literature research of the current state of the problem with emphasis on basic research
2. Explain and discuss the principles of laboratory measurement of electron stimulated desorption
3. Describe the commissioning procedure of the prepared experimental vacuum setup, characterize its components and specify your own contribution to this process
4. Evaluate the verification measurements with the experimental setup and analyze the first measured data

Bibliography / sources:

Jousten, Karl, ed. Handbook of vacuum technology. John Wiley & Sons, 2016.
Weston, George Frederick. Ultrahigh vacuum practice. Elsevier, 2013.
Yates Jr, John T. "Experimental innovations in surface science." Springer, New York 27 (1998): 181-0013.
Tratnik, Herbert. Electron stimulated desorption of condensed gases on cryogenic surfaces. No. CERN-THESIS-2006-038. 2005.

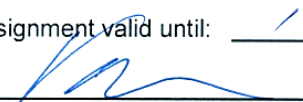
Name and workplace of master's thesis supervisor:

doc. Ing. Václav Vacek, CSc., Department of Physics, FME


Name and workplace of second master's thesis supervisor or consultant:

Date of master's thesis assignment: **18.04.2018** Deadline for master's thesis submission: **15.06.2016**

Assignment valid until: _____


doc. Ing. Václav Vacek, CSc.
Supervisor's signature

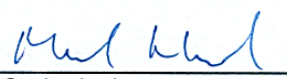

Head of department's signature


prof. Ing. Michael Valášek, DrSc.
Dean's signature

III. Assignment receipt

The student acknowledges that the master's thesis is an individual work. The student must produce his thesis without the assistance of others, with the exception of provided consultations. Within the master's thesis, the author must state the names of consultants and include a list of references.

18.4.2018
Date of assignment receipt


Student's signature

Prohlášení

Prohlašuji, že jsem tuto diplomovou práci vypracoval samostatně a při vypracování jsem použil pouze podklady uvedené v seznamu na konci této práce. Nemám závažný důvod proti užití tohoto školního díla ve smyslu § 60 zákona č. 121/2000 Sb., o právu autorském, o právech souvisejících s právem autorským a o změně některých zákonů (autorský zákon), pokud tak bude učiněno po dohodě s autorem práce.

V Praze dne: 15.6.2018

Michal Haubner

Michal Haubner

Acknowledgements

I would like to express my sincere gratitude to my supervisors and teachers for sharing their professional outlook and providing me an insightful guidance throughout different scientific fields.

I have special thanks to say to the VSM section of the CERN Technology department for the provided equipment and the exceptional learning opportunity. The work done throughout this Technical studentship was an enriching experience in terms of exploring a captivating field of science, developing new competences and especially pleasant and productive international collaboration. I equally thank to the staff of the Faculty of mechanical engineering at CTU in Prague for understanding and making this student internship possible.

Just as importantly, I wish to thank my family and friends for supporting me in every way possible during the course of my long studies.

Anotační list – Annotation

- Autor/Author: Bc. Michal Haubner
- Téma: Zprovoznění vakuové aparatury pro měření elektronově stimulované desorpce za kryogenních teplot
- Title: Commissioning of a vacuum system for measurements of electron stimulated desorption at cryogenic temperatures
- Academic year: 2017 – 2018
- Field of study: Instrumentation and control engineering
- Department: Department of instrumentation and control engineering
- Thesis supervisor: Doc. Ing. Václav Vacek, CSc.
- Bibliographic data: 68 pages, 6 tables, 46 graphics
- Anotace: Práce popisuje zprovoznění vakuové aparatury pro absolutní měření koeficientu elektronově stimulované desorpce (ESD) za kryogenních teplot. Je zpracována literární rešerše na zadanou problematiku s důrazem na částicové urychlovače, především kryogenní sekce LHC v CERNu. Vakuová komora z mu-metalu, tekutým heliem chlazený manipulátor, hmotnostní spektrometr a SCADA systém jsou charakterizovány a seřizeny pro měření ESD. Elektronové dělo ELG-2 je zautomatizováno pomocí LabVIEW. Dávkování plynů je nakalibrováno skrze analýzu křivky teplotně programované desorpce. Po zprovoznění jsou naměřena první data na měděném substrátu pokrytém $200 \cdot 10^{15} \text{ N}_2/\text{cm}^2$, ostřelovaném 50-2000 eV elektrony. Předběžná analýza udává ESD koeficient v jednotkách N_2/e^- , což se dobře shoduje s dostupnými zdroji.
- Klíčová slova: velmi vysoké vakuum, zprovoznění měřicí aparatury, elektronově stimulovaná desorpce, chlazení tekutým heliem, instrumentace pro UHV, automatizace elektronového děla
- Abstract: The commissioning is described of a new UHV facility for absolute measurement of electron stimulated desorption (ESD) yield at cryogenic temperatures. Literature is reviewed on relevant problematics, focusing on accelerator physics and especially cryogenic sections of the LHC at CERN. Instruments and components, as mu-metal UHV chamber, LHe-cooled manipulator residual gas analyser and SCADA system are characterised and set-up for ESD measurements. Electron gun ELG-2 is automated in LabVIEW. Gas dosing is calibrated by analysis the temperature programmed desorption curve. Preliminary data is measured for 50–2000 eV electrons impinging $200 \cdot 10^{15} \text{ N}_2/\text{cm}^2$ coverage on Cu substrate. ESD yield is in units of N_2/e^- . Partial and final results are well cross-validated against literature resources.
- Keywords: ultra-high vacuum, vacuum measurement, setup commissioning, electron stimulated desorption, liquid helium cryocooling, UHV instrumentation, electron gun automation

Contents

1	Introduction.....	9
1.1	Motivation	9
1.2	Synchrotron radiation and electron cloud.....	9
1.3	Dynamic vacuum	11
1.4	Objectives of the thesis.....	13
2	Electron stimulated desorption	14
2.1	Basic mechanism	14
2.2	ESD yield evaluation.....	15
2.3	Principle of ESD measurement.....	16
2.4	Factors affecting ESD yield	18
2.4.1	Materials and surface treatments.....	19
2.4.2	Coatings	20
2.4.3	Temperature	20
2.4.4	Electron energy.....	21
2.5	Adsorbate	21
2.5.1	Adsorbate morphology	22
2.5.2	Chemistry	23
2.6	Simulation	23
2.7	Findings of the theoretical part.....	24
4	Experimental setup description	25
4.1	Target design parameters.....	25
4.2	Scheme of the experiment	26
4.2.1	Arrangement of instruments	27
4.4	Mu-metal vacuum chamber.....	29
4.5	Cryogenic manipulator	30
4.6	Vacuum generation.....	32
4.6.1	Turbomolecular pump.....	32
4.6.2	Getter pump.....	33
4.6.3	Analysis of the pump-down curve.....	34
4.7	Bakeout procedure	35
4.7.1	Bakeout realisation.....	36
4.7.2	Bakeout results analysis.....	37
4.7.3	Mass spectrum comparison.....	38
4.8	Liquid Helium cooling.....	39
4.8.1	Cryo-pumping effect.....	41
4.9	Gas injection and dosing system.....	42
4.9.1	General layout	42
4.9.3	Pumping speed measurement	43
4.9.5	Gas dosing.....	46
4.9.6	Dosing system	47
4.9.7	Temperature programmed desorption.....	47
4.10	Bayard-Alpert vacuum gauge	48

4.12	Quadrupole mass spectrometer	51
4.12.1	Principle of operation	51
4.12.2	Secondary electron multiplier characteristics.....	52
4.12.3	RGA calibration by gas injection.....	53
4.12.4	Fragmentation patterns comparison to NIST database	54
4.13	Data acquisition system	55
5	Electron gun	57
5.1	Principle of operation	57
5.1.1	Parameter space	58
5.2	Electron source	59
5.2.1	Electron beam current levelling using the grid.....	60
5.3	Electrostatic optics	61
5.4	Deflection plates	63
5.5	Beam parameters	64
5.5.1	Current on Faraday cup vs. bias.....	66
5.6	LabVIEW control	67
5.6.1	Implementation of additional functions.....	68
5.7	Verification of functionality	70
6	Commissioning measurements	71
6.1	Preliminary measurements at cryogenic temperature	71
6.2	Data evaluation	72
6.2.1	Phosphorescence in N ₂	73
7	Summary and conclusions.....	74
7.1	Findings of the theoretical part.....	74
7.2	Results of the commissioning.....	74
7.3	Summary of the experimental results.....	75
7.4	My contribution	76
7.5	Conclusion of the thesis.....	76
7.6	Application of results and suggestion for further study.....	76
8	References.....	78
9	List of figures.....	83
10	List of tables.....	84
11	Appendix A – Enclosed CD.....	84
12	Appendix B – P&ID drawing of the entire setup	85
13	Appendix C – Photograph of entire experimental setup.....	86

Nomenclature

k	sensitivity of RGA and BAG; relative, absolute	[1],[A.mbar ⁻¹]
k_B	Boltzmann constant	[J·K ⁻¹]
\dot{N}	number of particles per unit time	[1.s ⁻¹]
q_e	elementary charge	[C]
T	thermodynamic temperature	[K]
S	effective pumping speed	[1.s ⁻¹]
c	proportionality coefficient	[V.eV ⁻¹]
η_e	electron stimulated desorption yield (in molecules/e ⁻)	[1]
I_e	electric current	[A]
\dot{Q}_{gas}	gas load	[mbar.l.s ⁻¹]
p	pressure	[mbar]
M	molar mass	[g.mol ⁻¹]
C	conductance	[1.s ⁻¹]
D	diameter	[mm]
V	volume	[l]
V	voltage	[V]
A	area	[cm ²]
E_k	kinetic energy	[eV]

Abbreviations

BAG	Bayard-Alpert gauge
BG	background
CF	ConFlat flange
CERN	European Organization for Nuclear Research
DAQ	data acquisition
DN	diameter nominal
ESD	electron stimulated desorption
FC	Faraday cup
FWHM	full-width at half-maximum
I/O	input/output
LHC	large hadron collider
LHe	liquid Helium
ML	mono-layer
NC	normally closed
NEG	non-evaporative getter
NIST	US National Institute of Standards and Technology
OFHC	oxygen-free high thermal conductivity
P&ID	pipng and instrumentation diagram
PSD	photon stimulated desorption
RGA	residual gas analyser
RV	rotary vane pump
SCADA	supervisory control and data acquisition
SEY	secondary electron yield
SEM	secondary electron multiplier
TC	thermocouple
TPD	temperature programmed desorption
UHV	ultra-high vacuum

1 Introduction

Accelerator physics is a specific branch of science which in some way incorporates many other fields of applied and theoretical physics, together with numerous other disciplines. Successful operation of a high-energy accelerator complex, along with its injection and transfer lines, experimental vacuum chambers and many other pieces of equipment, requires a broad portfolio of state-of-the-art engineering solutions pushed to the very limits possible. One of such fields is the vacuum physics, which provides a tool necessary for circulation of highly energetic particles inside the accelerator storage ring with the least possible interference with the surrounding matter.

The creation and sustaining of ultrahigh vacuum inside an accelerator during its nominal operating conditions is by itself a challenging task. The phenomenon of so-called dynamic vacuum has quickly become one of the main limiting factors and indeed, this problem has been addressed since the dawn of accelerator science. As a result, very effective and sophisticated methods have been developed for the purpose of mitigating and controlling the dynamic vacuum. The dynamic vacuum problematics remains a challenge and needs to be addressed accordingly, as today's accelerators are being continuously upgraded and new accelerators are being designed at the same time, pushing the limits to even higher energies and intensities.

1.1 Motivation

Modern particle accelerators generally consist of several kinds of magnets, most of which are cooled to cryogenic temperatures in order to reach superconductive state. Superconductivity allows more intense magnetic fields, resulting in smaller radius of curvature, thus making the accelerator more compact and at the same time reduces electric power consumption due to zero intrinsic electrical resistance of magnet's winding. As a by-product, the beam tube is operated at cryogenic temperature as well and its cold surface is effectively cryo-pumping the residual gas, creating a layer of adsorbed gas on the inner surface of the beam tube. The interaction of this cold surface with the conditions created by highly energetic particle beam needs to be studied and optimised for successful operation of accelerators. In turn, there is a strong motivation to study the effects influencing dynamic vacuum under laboratory conditions, approaching those of real accelerators in a precisely controlled manner. The study of processes governing the dynamic vacuum phenomena will allow for a control over them, as it is one of the main keys for effective operation of current accelerators and development of new and better ones.

1.2 Synchrotron radiation and electron cloud

There are thousands of particle accelerators throughout the world, out of which a great number is built in a circular arrangement. Leaving the physics

reasons for this aside, there remains a price to pay for such circular accelerators in the form of synchrotron radiation. This type of radiation is emitted when a beam of charged relativistic particles is deviated, typically by a magnetic field. The synchrotron radiation emitted by these particles then inevitably impinges the inner wall of the beam tube and emits electrons via photoelectric effect, while simultaneously desorbing gases. The gas particles degrade the ultra-high vacuum, decrease life-time of the circulating beam and in extreme cases lead to a beam loss, magnet quenches etc.

The spectrum of synchrotron radiation varies strongly with the energy of particles and their acceleration. An example of radiation spectra for the case of a dipole magnet of the Large Hadron Collider is shown in Figure 1., as published by v. Baglin et al. [1]. The peak of photon energy for the LHC and HL-LHC is in the range of 1 eV to 10 eV. The energy required to extract electrons from common materials, so called work function, is in the range of units of eV. Direct comparison of these values indicates that the photoelectric effect caused by synchrotron radiation has to be considered for LHC-type of machines.

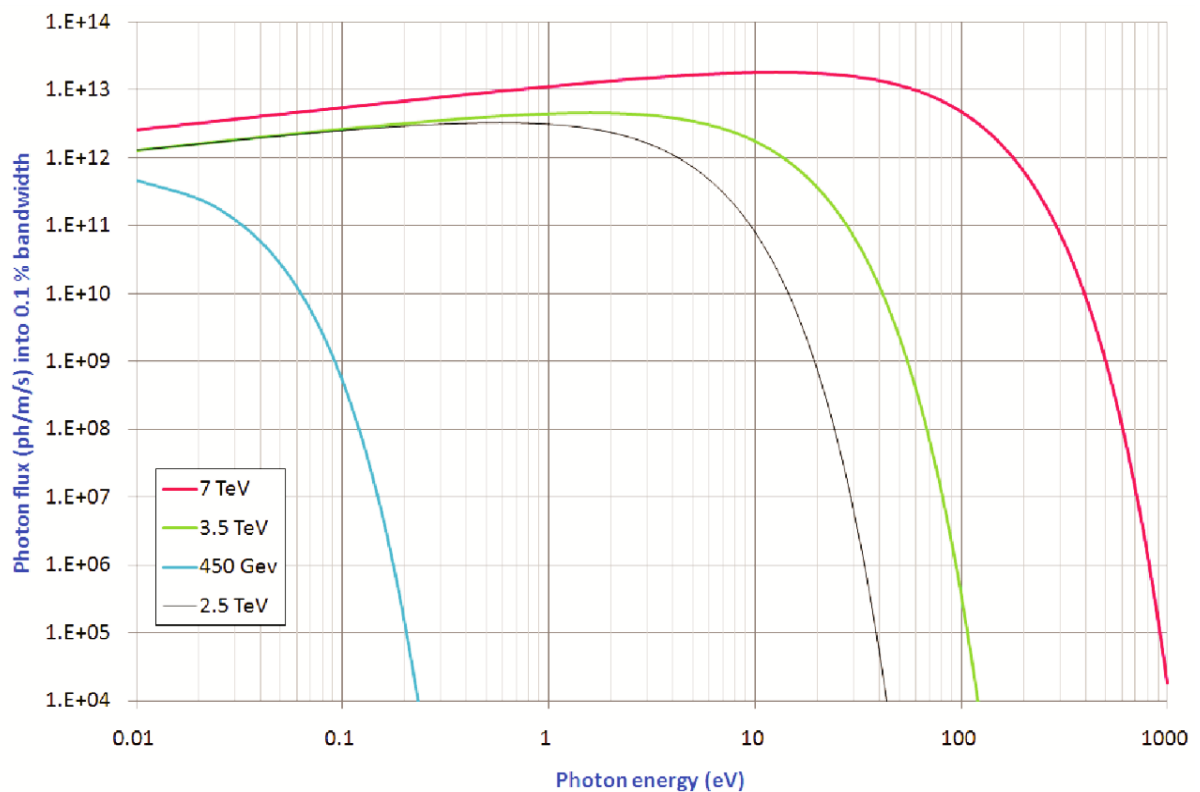


Figure 1. Calculated synchrotron radiation spectra for LHC dipole magnet at energies from injection to nominal. Image kindly reproduced after V. Baglin et al. [1].

The synchrotron radiation induces photoelectric effect on the surface of beam tube and extracts electrons. These photoelectrons are then accelerated by interaction with the circulating beam. The closed geometry of the beam tube leads to an inevitable collision of electrons with the inner surface and possible extraction of secondary

electrons from the surface is underway. This effect of electron multipacting results into an electron cloud in the beam tube.

The plot in Figure 2 presented by Cimino et al. [6] shows a secondary electron yield (SEY), which is the number of created secondary electrons per each incident electron. The number of secondary electrons varies not only with the energy of incident electrons, but equally with the total accumulated dose of electrons already received. This conditioning effect is commonly known as electron scrubbing and is widely used in practice. The plot shows a factor of 2 reduction of SEY for fully conditioned copper surface. SEY less or equal to 1 means that no runaway of electron cloud is to be expected. The SEY is a subject to other variables, which are not illustrated, such as material or microgeometry.

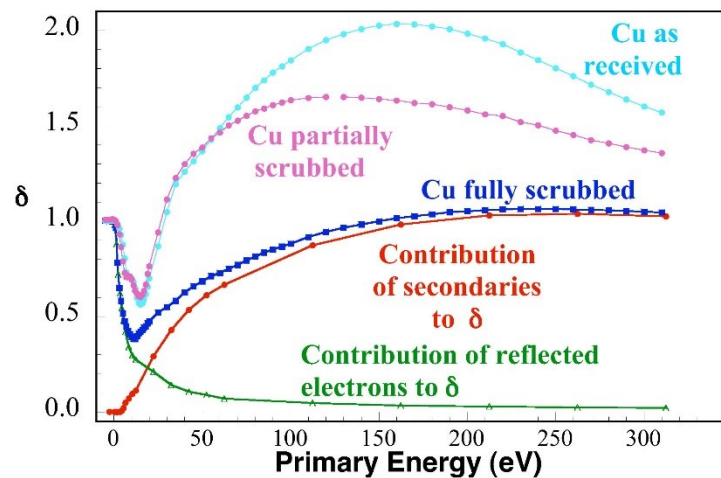


Figure 2: Secondary electron yield as a function of incident electron energy. The Cu surface exhibits a conditioning effect of the accumulated dose of electrons. Image credit: [6].

Detailed analysis of the electron cloud problematics in relation to LHC operation can be found for example in [1]-[6], along with its effects on accelerator operation. It has been carefully studied and analysed in a variety of materials, surface treatments and conditions.

1.3 Dynamic vacuum

The ultimate vacuum of a vacuum chamber, i.e. the base pressure is given by a simple balance between an outgassing rate and a pumping speed. The beam tube forms such a vacuum chamber and the pumping speed is a combination of different pumping effects, whatever they are in the given context of a specific part of the beam tube. When different forms of radiation strike the beam tube, they stimulate gas desorption from its inner surface. This imposes additional gas load on the pumping and causes the pressure to increase, because the pumping speed remains limited. Thus, the dynamic vacuum rises and falls with the presence of synchrotron radiation and electron cloud. The vacuum recovers back to its original base pressure after the irradiation disappears.

A photon, electron and ion stimulated desorption can be distinguished depending on the primary energetic particle, as opposed to thermal outgassing, which occurs naturally as a result of thermal movement of molecules. The basic desorption mechanisms are visualised in Figure 3, originally published in [6] for the purpose of dynamic vacuum simulation software. Synchrotron radiation, which was previously emitted by a circulating proton beam, advances from the left side of the figure. This radiation strikes the surface and extracts photoelectrons. These secondary electrons are accelerated by the passing proton beam and hit the wall again, which results into extraction of even more electrons, creating an electron cloud. This electron cloud can equally desorb gases from the surface of the beam tube. In addition, residual gas present in the non-perfect vacuum of the beam tube undergoes scattering with the proton beam and creates positively charged ions. Once more, these ions impinge the surface and desorb other species. All these distinct mechanisms can engage in the phenomenon of so called dynamic vacuum and are depicted in the schematics.

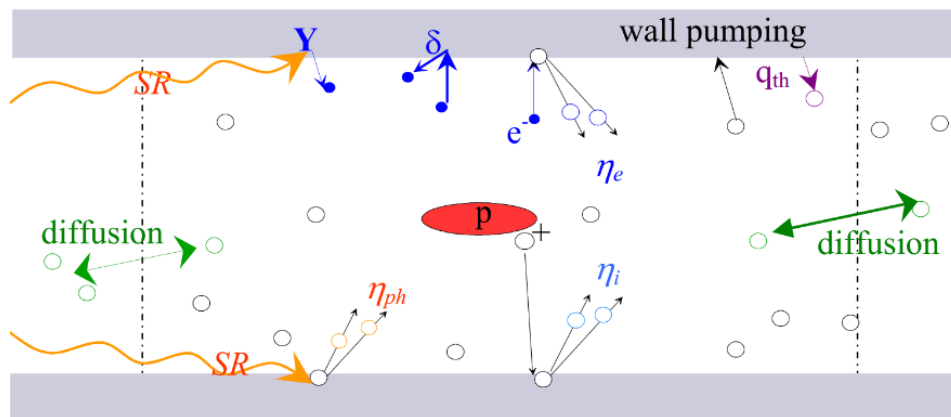


Figure 3. Scheme of basic desorption mechanisms within a beam tube. Image credit: [7].

This excitement of particles within the beam tube slowly dissipates and does not become a problem, as long as there is long enough period between passing proton bunches. If this is not the case, there can be a runaway of the number of particles interfering with the beam and the pressure and temperature will increase above any constraints. This leads to a loss of beam, activation of surrounding matter and other consequences, such as magnet quenches. It can be inferred from presence of the electron cloud, that the main desorption mechanism shall be the electron stimulated desorption, hereafter abbreviated as ESD. Consequently, thorough understanding of the ESD mechanism and its variation with material, surface treatment and environmental conditions is necessary. A sound understanding of the stimulated desorption phenomenon will enable its optimization, leading to sustaining of the dynamic vacuum in a controlled way. This will mitigate one of the main limits of modern high-energy accelerators.

1.4 Objectives of the thesis

It has been decided to devise an experimental apparatus for thorough investigation of electron stimulated desorption, which should be capable of characterisation of materials and coatings under different types of irradiation and with condensate layers created at cryogenic temperatures. The acquired experimental dataset is expected to broaden the understanding of dynamic vacuum and support efficient operation and design of accelerators.

I was given a special opportunity of participation in the commissioning process of such an experimental setup, which was executed under the supervision and with the help of CERN's TE-VSC-VSM team. The major milestones will be described throughout this thesis. Accent will be placed on components that are essential to the ESD measurement process, as the complexity and number of subsystems exceeds the range of a thesis. Calibration measurements will be presented and the first data will be analysed to verify the effectivity of the commissioning process. This technical part shall be preceded by a literature review of the current state of problematics and its relation to accelerator physics and other basic research fields.

2 Electron stimulated desorption

2.1 Basic mechanism

The goal of this experiment is to study the process of desorption stimulated by electrons under controlled conditions. A desorption process is schematized in Figure 4. Suppose that an electron beam strikes a material surface and gradually depletes its energy within the bulk. Some of the primary electrons are elastically backscattered, but the rest of the electron beam energy dissipates into the bulk, where the primary electrons create an avalanche of secondary electrons. This results in a volume of excitation and its size is dependent on many factors. This includes the primary electron energy, atomic number and density of the bulk material. These energetic secondary electrons can in turn excite atoms or molecules of gases, which are normally adsorbed on the surface. If these molecules gain enough energy from the underlying processes they can desorb and enter the vacuum of the chamber.

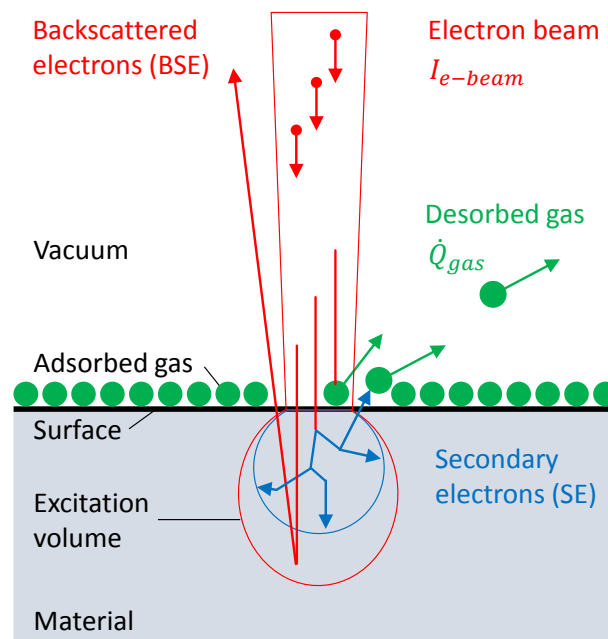


Figure 4: Idealized scheme of the electron stimulated desorption phenomena.

The underlying processes which take effect on a nanoscale will not be further discussed. Yet, they result in desorption which is an effect well observable on the macroscopic scale as a pressure rise in a vacuum vessel. The rate of desorption is strongly dependent not only on the properties of the electron beam, but also on the material, its surface treatment or adsorbate on its surface. It is worth noting that there is almost inevitably a layer of adsorbed gas deposited from the residual gas in the vacuum vessel at cryogenic temperatures. Its thickness can vary significantly from sub-monolayer to multilayer coverages, depending on many factors. A coverage

of 1 monolayer is depicted for simplicity in a way as it is defined by IUPAC [8] to be a “single tightly packed layer of gas”. It shall be possible to precisely control the composition and coverage of this adsorbate in this newly commissioned setup.

2.2 ESD yield evaluation

A quantitative definition of desorption phenomena is needed to compare different measurement conditions. The most practical and widely used quantitative measures of the ESD, which is applicable on the macroscopic level, is a ratio between the number of incoming electrons and the amount of desorbed gas particles. Or simply the average number of gas particles desorbed by an incoming electron. The definition can also be extended to desorption stimulated by other types of particles, such as photons or ions. This ratio is commonly known as desorption yield. It can be assumed, that at any moment the number of desorbed gas molecules per second \dot{N}_{gas} is proportional to the number of impinging electrons \dot{N}_{e-} . Hence a simple relation of these two numbers by a factor of electron desorption yield η_e as follows:

$$\dot{N}_{gas} = \eta_e \cdot \dot{N}_{e-} \quad [1/s] \quad (2.1)$$

The equation is expressed in the form differentiated with respect to time, making it useful in the measurement process itself, which deals with flows rather than absolute quantities. Solving for the electron desorption yield, which can be expressed as a ratio:

$$\eta_e = \dot{N}_{gas} / \dot{N}_{e-} \quad [1] \quad (2.2)$$

The number of electrons \dot{N}_{e-} per unit time is commonly measured as electrical current. Hence, we obtain the number of electrons entering the process dividing the current by the electron’s elementary charge q_e :

$$\dot{N}_{e-} = q_e \cdot I_e \quad [1/s] \quad (2.3)$$

Equally, the flow of desorbed gas molecules can be expressed in terms of a gas load as follows. The k_B stands for the Boltzmann’s constant and T for thermodynamic temperature. The setup is operated at ambient temperature, which thermalizes gas molecules to a temperature of about 300 K upon their impact on the wall.

$$\dot{N}_{gas} = \frac{\dot{Q}_{gas}}{k_B \cdot T} \quad [1/s] \quad (2.4)$$

Now plugging both expressions into the ESD yield equation we obtain:

$$\eta_e = \frac{\dot{Q}_{gas}}{k_B \cdot T} \bigg/ \frac{q_e}{I_e} \quad \left[\frac{Pa \cdot m^3 \cdot s^{-1} \cdot C^{-1}}{J \cdot K^{-1} \cdot K \cdot A^{-1}} = 1 \right] \quad (2.5)$$

As it is electrons that impinge a sample, the flow of these incoming charged particles can be directly and precisely measured by the electric current arriving on a sample.

The situation becomes far more complicated for the quantity of desorbed gas, because it is a difficult task to measure a flow of inert gas in vacuum. The gas load can be determined indirectly for a given gas specie j . The background signal is subtracted from the measurement, hence the Δ sign. Knowing a pressure rise Δp_j above the background pressure $p_{0,j}$ of the vacuum chamber with a pumping speed S_j , we obtain:

$$\dot{Q}_j = S_j \cdot \Delta p_j \quad [1/s] \quad (2.6)$$

The pumping speed S_j is presumed to be independent on pressure p_j for vacuum pumps used in the setup in the given UHV pressure range. A mass spectrometer is used to measure partial pressures of gas species. The mass spectrometer is commonly referred to as a residual gas analyser (RGA), which indicates its general purpose in the vacuum science. It is possible to convert the current measured on the RGA to a partial pressure, if its sensitivity is known for a given gas. The sensitivity coefficient k_j linearly relates the ion current ΔI_j collected and measured in the mass spectrometer and the partial pressure Δp_j of a gas.

$$k_j = \Delta I_j / \Delta p_j \quad [A/mbar] \quad (2.7)$$

The partial pressure of a gas as converted from the current of mass spectrometer:

$$\Delta p_j = \Delta I_j / k_j \quad [mbar] \quad (2.8)$$

Writing explicitly for the background subtraction:

$$p_j - p_{0,j} = (I_j - I_{0,j}) / k_j \quad [mbar] \quad (2.9)$$

An injection of a given gas is done prior to each measurement to assess spectrometer's absolute sensitivity as a function of partial pressure and also to measure the effective pumping speed of this gas. As the measurement of gas load \dot{Q}_j is an indirect measurement, all sorts of imprecisions can intervene in its quantification.

2.3 Principle of ESD measurement

The basic layout of an ESD measurement could be the following. A sample of a material is placed in the vacuum chamber on an electrically insulated holder. An electron gun faces a sample and emits a beam of electrons with a current I_{e-beam} , which hits the sample and results into various scattering processes. Some electrons are elastically backscattered and leave the sample with almost the same energy as the primary electrons, whereas other electrons dissipate their energy within the bulk by creating secondary electrons. These secondary electrons have low energy, which is normally in the range of 0 ÷ 50 eV, with the peak well under 20 eV. Other energy dissipation processes may also occur, such as excitation of Auger electrons, creation

of radiation and heat. These will be neglected in the further examination, as they are not of primary interest.

The sample has an electrical potential given by a bias voltage V_{bias} referenced to the ground and is to be user-defined for the given context of experiment. Positive bias on the sample ensures that secondary electrons are attracted back to the sample. The biasing power supply is connected to an ammeter that measures the current collected by the sample I_{sample} , so the measured current I_{sample} represents the majority of electrons, which stimulate gas desorption upon their impact on the sample. Hence, we have obtained a direct measure of electron current for Equation 2.3.

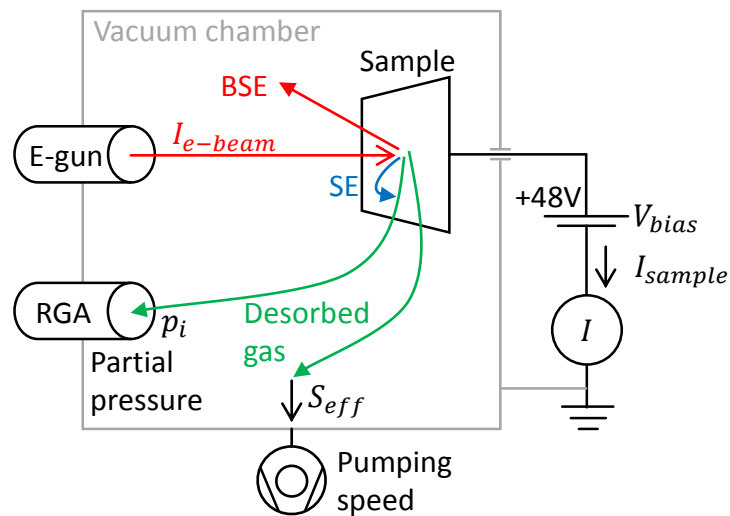


Figure 5: Measurement of the sample current using a bias voltage and current amplifier.

Gas molecules which are desorbed by the electron bombardment enter the volume of the vacuum chamber and are measurable as a pressure increase. The total pressure in the chamber is measured by a Bayard-Alpert ionisation gauge and the partial pressure is measured by a mass spectrometer.

To summarize, different variables in the Equation 2.5 stand for different instruments in the setup. Electron current I_e comes from the electron gun and is measured by a current amplifier. Gas load \dot{Q}_{gas} is measured using a vacuum gauge and the residual gas analyser and knowing the pumping speed S . Temperature T is measured by a thermocouple placed on the vacuum chamber.

The following literature research lists desorption studies, which use different ways to quantify the results, depending on the measurement method, purpose of the measurement, etc. Frequently seen and the least quantitative approach is the usage of “arbitrary units”, allowing only for a relative comparison of measurements within the same setup and conditions. Better approach is to quantify the result in some way, e.g. by calculating the ESD yield.

2.4 Factors affecting ESD yield

ESD yield varies over many degrees of magnitude, depending on the nature of a surface, its treatments, coatings, condensates, microgeometry, etc. These variables can be divided into distinct classes. The first class of influencing factors characterizes the substrate material and its intrinsic properties, such as composition, density and atomic number, which define its stopping power and are all important for the energy dissipating processes within the bulk. The surface also plays an important role, its microgeometry and composition which can be different from the bulk. The second class represents the nature of incoming particles, their energy spectrum, angle of incidence, quantity and total dose that was already accumulated in the substrate. All these characteristics are significant input variables for ESD processes and as such are to be precisely controlled, if a solid investigation of ESD is to be done. The situation changes entirely if layers of gas particles are condensed on the surface of the substrate. Such adsorbate generally increases the ESD yield, as it is composed of atoms and molecules with relatively low binding energies, thus easy to excite and desorb into the surrounding vacuum.

ESD measurement is a resource-demanding process, which is costly in terms of time and hi-end equipment, so any measurements are usually done with a clear practical purpose under way. As a result, the literature lacks a systematic library of reliable ESD properties measured in a broad range of conditions, which would be accessible to general community. Instead, many piecewise measurements are scattered over different journals and applications ranging from electron microscopy to astrophysics. The portfolio of materials, that have been punctually characterized in terms of ESD is relatively small and involves materials used for construction of UHV appliances. These are most frequently metals, such as stainless steel, copper and aluminium. Given the construction purpose, they usually come with some form of surface treatment or annealing process, which should make them UHV-compliant. This usually involves electrical and chemical treatments, vacuum or air firing and in-situ bake-out, followed by a getter activation, if any. Such treatments leave the final surface with a relatively small amount of particles that can be desorbed or outgassed. Such series of processes is further followed by conditioning in the case of accelerator components.

A detailed work on ESD principles and measurements was published by Ramsier and Yates [9]. They put forward a detailed scientific description of desorption derived from binding energies and electronic transitions. Then they discuss underlying physical processes with a particular focus on surface chemistry and crystallography. They also describe measurement methods and provide a very extensive literature research. Other works covering these principles are those of Menzel [10] and Melius et al. [11]. An article covering the dawn of ESD problematics was summarized by Redhead [12].

2.4.1 Materials and surface treatments

Malyshev, Hogan and Pendleton [13] investigated ESD yield reduction of vacuum-fired and surface-polished 316LN stainless steel, as the main construction material of accelerator components. They used a setup dedicated to measurement of ESD at high electron energies and doses. They confirmed the high effectivity of these surface treatments. They measured H₂ desorption yield from 10⁻¹ to 10⁻² molecules/e⁻ at low electron dose, depending on the treatment. For CO, CO₂ and CH₄ they observed values from 10⁻² to 10⁻⁴ molecules/e⁻. Trace amounts of O₂, H₂O and Ar were also detected, but remain negligible behind the other species.

Ding and Williams [14] have investigated surface-treated Al prior to Malyshev et al. They observed a rising energy-dependence of ESD yield for energies up to 1.5 keV, as well as conditioning effect of the total accumulated dose. The nominal values of ESD are in agreement with works of Malyshev. Moreover, they discuss the positive effect of glow discharge treatment on the ESD yield and compare their experimental results to their previous works on surface-treated aluminium.

A solid investigation of ESD induced by 20 ÷ 300 eV electrons from polycrystalline OFHC copper was presented by Billard et al. [15]. The yield for 300 eV electrons at ambient temperature ranges from 20 H₂/e⁻ to 2·10⁻² CO/e⁻ and decreases, as the surface is conditioned by an accumulated electron dose. Besides that, the yield increases linearly as electron energy rises from 20 eV to 300 eV.

Kúkol'ová presented in her thesis [16] ESD yields of common gases for both baked and unbaked Copper for 300 eV and 500 eV electrons. This is complemented by measurements done on unbaked SS. A conditioning effect is also observed for cumulative doses up to 10¹⁹ electrons/cm². ESD yields of all common gases are from 10⁻³ to 10⁻¹ molecules /e⁻ before the conditioning takes a severe effect.

Nishiwaki et al. [17] measured the ESD yield of chemically-etched oxygen-free copper subjected to 15 keV electron bombardment and measured the desorption of various gas species and its evolution with accumulated dose. Their results are in the order of 10⁻² molecules/e⁻ and are complemented by the analysis of surface composition by Auger electron spectroscopy. Effects of etching and chemical passivation are discussed.

The dissertation of G. Vorlaufer [18] is a very thorough work and covers the effect of treatment of copper samples with nitrogen and oxygen free radicals. This treatment brings a significant improvement of about 1 order of magnitude of ESD yield at low electron doses, as compared to non-treated surface, but this advantage disappears at higher accumulated doses. The ESD yield for electron energy of 300 eV starts at 3·10⁻¹ H₂/e⁻ for low dose and decreases to 10⁻³ H₂/e⁻ when fully conditioned. Other gas species exhibit similar behaviour, but are off-set to lower yields. These measurements are then supported by surface analysis of treated samples and finally used in numerical models of dynamic vacuum in accelerator application.

2.4.2 Coatings

An effect of surface coatings on ESD yield was extensively studied, as many parts of the CERN accelerator complex are coated or are foreseen to be coated in the future. Coatings are generally applied to the inner surface of the beam tube in order to reduce its SEY and ESD yields. That is to reduce the amount of secondary electrons extracted by energetic particles and/or to provide additional pumping. Various coatings are used, ranging from amorphous carbon to non-evaporative getters based on Ti, Zr and V. Activation of such getter coatings is done by its in-situ bakeout.

The effect of carbon coating on the ESD was presented in [19] and [20]. Results were evaluated for 4 different gases: H₂, CO, CO₂ and CH₄ at temperatures from ambient to 250 °C and compared to a treated SS without coating. The ESD yield for carbon coated sample was generally lower than 10⁻² molecules/e⁻ for all followed gases.

Another type of thin Ti-Zr getter coating was examined by Benvenuti et al. [21] and showed moderate values of ESD ranging from 10⁻³ to 10⁻² molecules/e⁻, depending on the gas. Their measurements were done with 500 eV electrons and for getter activated at different temperatures ranging from 120 °C to 400 °C.

A study of a Ti-Zr-Hf-V getter-coated vacuum-fired stainless steel was also done by Malyshev et al. [22] and showed very low values of ESD as compared to materials without coatings and treatments. The yield was in the range of 10⁻⁴ molecules/e⁻ for H₂ and CO and even lower for CH₄ and CO₂.

The same phenomena, along with PSD, was addressed in the dissertation of Pimpec [23] for the case of electro-polished Copper and NEG-coated Copper. The results comply to the rest of presented studies in terms of the ESD yield and its conditioning with accumulated 300 eV electron dose up to 10²¹ electrons/cm². The desorbed gas is equally dominated by H₂ molecule and is lower for NEG-coated Copper than for electro-polished Copper. The experimental dataset is then used for generation of regression curves and simple models, which fit the data more or less accurately.

2.4.3 Temperature

Malyshev and Naran [24] conclude that the ESD yield does not change critically in temperature range from -15 °C to 70 °C. They state that dependence of ESD yield on temperature is margining the detection limit of the setup. However, the paper does not state how or whether the temperature influence on conductivity and therefore the effective pumping speed is accounted for.

Another research group [25] increases temperatures even further and measures ESD yields at 40 °C and at 200 °C of SS 316 LN, OFHC Copper and anticorodal Aluminium, which were all baked out prior to measurements. ESD yields of H₂, CH₄, CO and CO₂ were commonly between 10⁻⁴ to 10⁻² molecules/e⁻. Yields of all gases from SS and Cu were observed to be about twice as high for at 200 °C than for 40 °C. Conversely,

Aluminium exhibited lower yields at high temperature. As usual, a conditioning effect was observed with accumulated dose.

2.4.4 Electron energy

Malyshev et al. [26] have observed that the ESD yield has a rising tendency in a wide spread of electron energies from 10 eV to 5 keV. A conditioning effect was observed to be about 1 order of magnitude of ESD yield per decade of absorbed electron dose, which well agrees with measurements performed previously on their experimental setup.

Malyshev et al. [27] also performed similar experiment on baked aluminium alloy and Al coated stainless steel and published results slightly higher than those for surface-treated SS. They also observed a linear dependency of ESD yield on electron energy from 40 eV to 5 keV.

2.5 Adsorbate

A research, which is probably the most closely-related to the subject of this thesis was performed by Tratnik and published in his dissertation [28] and research paper along with Hilleret and Stori [29]. They measure ESD in layers of gas condensed at cryogenic surfaces and investigate wide range of conditions in terms of energy, coverage and condensate composition. The thesis provides an extensive dataset of ESD yields for common vacuum gasses H₂, N₂, CH₄, CO and CO₂ as well as noble gases He, Ne, Ar, Kr and Xe. Measurements are taken for a range of energies 40 ÷ 1000 eV, coverages 0.1 ÷ 5000 ML and doses 10¹³ ÷ 10²⁰ e⁻/cm² and result into ESD yields ranging from 10⁻¹ to 10⁺⁴ molecules/e⁻. They also estimate uncertainties of their measurements to be around 30 %.

Measurements of SEY on the same experimental setup are presented in a paper [30], conference proceeding [31] and in the thesis of Kuzucan [32] and the ESD yield is calculated as a by-product. Condensate layers of N₂, CO, CO₂ and CH₄ are evaluated to have yield about 2·10⁻² molecules/e⁻. The same yield is claimed irrespective of the substrate material.

Schou et al. [33] measured ESD in thick layers of hydrogen for electron energies from 300 eV to 2 keV using a quartz microbalance, as opposed to a classical measurement by a pressure rise in an UHV chamber. They investigated the influence of metal substrate and energy dissipation processes eventually governing the ESD yield. Excessively high yields between 2·10² H₂/e⁻ and 7·10³ H₂/e⁻ are presented for thick H₂ coverages of 70 ÷ 1500 ML. A thorough analysis of results is presented and possible effects discussed.

An ESD yield measurement done by Ellegard et al. employed a microbalance in [34] to evaluate the amount of N₂ and O₂ gases, that were previously condensed on a cold surface to form thick multilayer coverage around 100 ML. This adsorbate was then desorbed by electrons with energies from 1 keV to 3 keV at an ESD yield between

1 and 4 molecule/e⁻. Ellegaard et al. [35] also measured ESD for energies from 800 eV to 3 keV in thick Argon films on Gold substrate at temperatures around 5 K. Desorption yield of 2 ÷ 3 Ar/e⁻ was measured for 3 keV electrons and was observed to saturate for coverages larger than 2000 ML. Coverages around 20 ML thick had a yield only 0.2 Ar/e⁻. They also use their data to derive a characteristic diffusion length of an excitation to be 200 ÷ 300 nm. The former works [33]-[35] were amongst others summarized in the dissertation of Schou [36].

Besides that, Svendsen et al. [37] present a study on desorption yield of solid deuterium stimulated by 2 keV electrons. They vary the deuterium thickness in the range of 100 ÷ 4000 ML. As a result, the yield changes between 2 ÷ 30 D₂/e⁻ in a U-shaped manner, which is difficult to explain. All results presented in [33]-[37] were measured using a microbalance, which is rather a non-traditional approach and is therefore important for cross-validation of results.

The effect of substrate crystal orientation was investigated by Outlaw et al. [38] for Platinum covered by oxygen and bombarded with low energy electrons of 100 eV. The results are well developed but a figure for ESD yield is not presented, as all plots are normalized or with arbitrary units.

Arakawa and Tuzi [39] investigated desorption of H₂ condensed on a Xenon substrate. Electrons with 200 eV desorbed from units to hundreds of H₂/e⁻, depending on the conditions of this complicated experimental layout.

Adachi et al [40] publish ESD and PSD measured on the surface of solid Krypton for 220 eV electrons. They measured the ESD yield to be rising from 10⁻² to 10⁻¹ atoms/e⁻ for coverages ranging from sub-monolayer to thick multilayers. They also measure the energy dependence of ESD to be rising between 50 eV and 320 eV, producing a yield in the same range in the case of 100 monolayer coverage. They also assess the uncertainty to be within ±33% of the order of magnitude.

2.5.1 Adsorbate morphology

Sieger and Orlando [41] investigated desorption of deuterium from D₂O, i.e. heavy water films condensed on a Platinum substrate in a temperature window from 90 to 180 K using a pulsed 100 eV electron beam. They go even further in [42] and use ESD as a method to probe the morphology of water ice, which was deposited on Pt(111) at temperatures around 120 K. They observe and discuss various morphology effects associated to temperature and thickness of adsorbed D₂O, but do not present a value for ESD yield.

Orlando and Grieves [43] focused on the effect of porosity in ices. They suggest that higher porosity and higher density of defects lead to higher ESD yields. These works of Orlando et al., despite being related to astrophysics and lacking absolute yield numbers, provide a valuable insight into the problematics of thick condensate layers at cryogenic temperatures.

Azria et al go further in [44]-[46] and condense molecular oxygen on D₂O films and observe similar effects with strong dependence on condensation temperature. They use very slow electrons between 6 eV and 20 eV, but they do not present the ESD yield for exact comparison either.

The effect of morphology of the substrate is studied by [47] and developed introducing a simple parametric model. Again, this is an important aspect, as technical surfaces exhibit large range of microscopic surface types and these have to be taken into account.

2.5.2 Chemistry

The energetic particles can also induce chemical reactions, such as dissociation in the first place. This effect is also extensively studied, often with respect to astrophysics, and is well covered in a summarizing report presented by Arumainayagam et al [48], or by Bass and Sanche [49].

2.6 Simulation

A Monte-Carlo simulation software CASINO, developed by [50] is frequently used to model interaction of a charged-particle beam with solid phase. This is useful in particular in the field of electron microscopy, but can also provide a valuable insight into the problematic of ESD. A summary put forward by Suga et al. [51] features a good visualisation of CASINO simulation of such interaction between impinging electrons and a silicon sample.

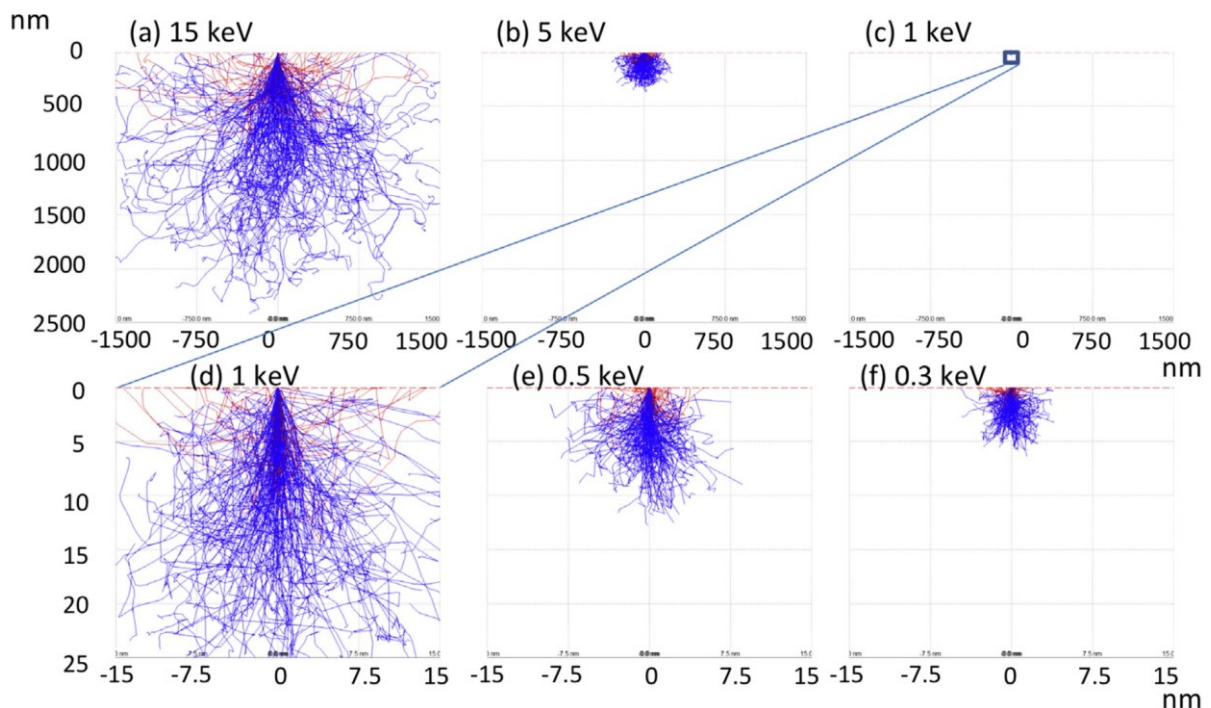


Figure 6: A simulation in CASINO [50] kindly reproduced from the work of Suga et al. [51].

The depth of energy depletion is dependent on the energy of incoming electrons. Red traces represent backscattered electrons, whereas blue are true secondary electrons. The penetration depth is in the range of tens of nm for electrons slower than 1 keV. This provides a clue on the ESD phenomena. Lower ESD yields are often observed for higher electron energies, which can be explained by energy depletion deeper in the bulk. Note the scale in nm for the sub-1keV electrons.

2.7 Findings of the theoretical part

It is worth noting here that the ESD measurements find application not only in accelerator science, or electron microscopy, but also in the astrophysical context, which also deals with high-energy particles and their interaction with condensed matter. This literature review briefly summarizes ESD research, particularly with respect to accelerator science. ESD was studied only in a relatively small amount of materials and in a normal range of conditions. Reliable systematic information on ESD is generally unavailable, especially at cryogenic temperatures.

It can be inferred both from the theoretical analysis and from experimental results, that the ESD yield increases if the energy is transferred to surface-bound molecules, or to the molecules in the vicinity of the surface. It is also safe to say that the ESD yield is higher for weakly bounded molecules, whichever they may be in the given context of an experiment. Despite of this, it is problematic to make further conclusions and to infer about the dependence on geometry, substrate, condensates, morphology, etc., as different experiments produce results, that are not easily comparable.

4 Experimental setup description

4.1 Target design parameters

There are two distinct goals, which combine into a list of requirements on the setup:

1. Reproduce in a controlled way conditions similar to those in accelerators in terms of pressure, temperature, electron energy and residual gas composition.
2. Provide clean experimental environment to investigate desired processes. This is ensured by ultrahigh vacuum, which corresponds to long monolayer formation times.

These goals are superimposed to obtain a list of target process and design parameters that shall be aimed for during the design and installation process of the setup. The Table 1. summarizes and puts concrete values on these parameters.

Table 1. Target process and design parameters of the experimental setup.

Quantity	Target range	Unit
Temperature range of material sample	10 ÷ 500	K
Ultimate base pressure	5 · 10 ⁻¹¹	mbar
Monolayer formation time	24	hours
Electron gun energy range	10 ÷ 2000	eV
Magnetic shielding factor	130	1

The temperature range extends as low as 10 K, in order to reproduce temperature of the on the LHC beam screen and to adsorb gases which otherwise do not condense, but at such low temperatures. The low base pressure of 5 · 10⁻¹¹ mbar serves to simulate ultrahigh vacuum present in the beam pipe, which ensures the least possible interaction of energetic particles with the surrounding matter and in this case prevents deterioration of the investigated surface by impinging gas molecules. This low pressure corresponds to a long monolayer formation time in the order of hours. Such time span is long enough so that a sample surface can be investigated without changing its properties during the measurement.

The following quantities are bound specifically to the studied phenomena. Electrons with relatively low energies of 10 ÷ 2000 eV should simulate the electron cloud action on a surface of the beam tube. Given the low energy of electrons in the investigated processes, a magnetic shielding is required to prevent the geomagnetic field from acting on the slow electrons and deviating them. As a result, the main vacuum chamber was chosen to be constructed from a thick permalloy material, commonly called mu-metal for its high permeability. The manufacturer states, that the chamber provides a magnetic shielding factor of 130 at the measurement point.

The cold surface of a beam tube in cryogenic magnets is a subject to cryo-pumping, which means that the residual gas is likely to stick to the surface due to the long sojourn time, remain adsorbed and form a condensate layer. The thickness and composition of such coverage is of course dependent the temperature of the surface, on the residual gas pressure and composition and on the exposition time. Coverages from sub-monolayer to multilayer are all to be subject of investigation for common gasses such as the listed ones. Injection possibility of various gases is also a must for further measurements. Gasses of interest that are common in vacuum science are H_2 , N_2 , CO , CO_2 , CH_4 , C_2H_6 , Ar and H_2O .

4.2 Scheme of the experiment

A simplified scheme of the setup is shown in Figure 7 to explain the basic concept of desorption measurement and its essential subcomponents. A sample of a material is fixed on the manipulator facing an electron gun, which bombards a small area of the sample surface with electron beam of known characteristics. This electron bombardment results into gas desorption and can be measured as a pressure rise in the vacuum chamber. The quantity and quality of released gas is then analysed via hot cathode Bayard-Alpert ion gauge (BAG) and by a quadrupole mass spectrometer, in vacuum science commonly referred to as residual gas analyser (RGA). After the electron bombardment stops, the pressure in the mu-chamber decays back to the ultimate base pressure of the chamber.

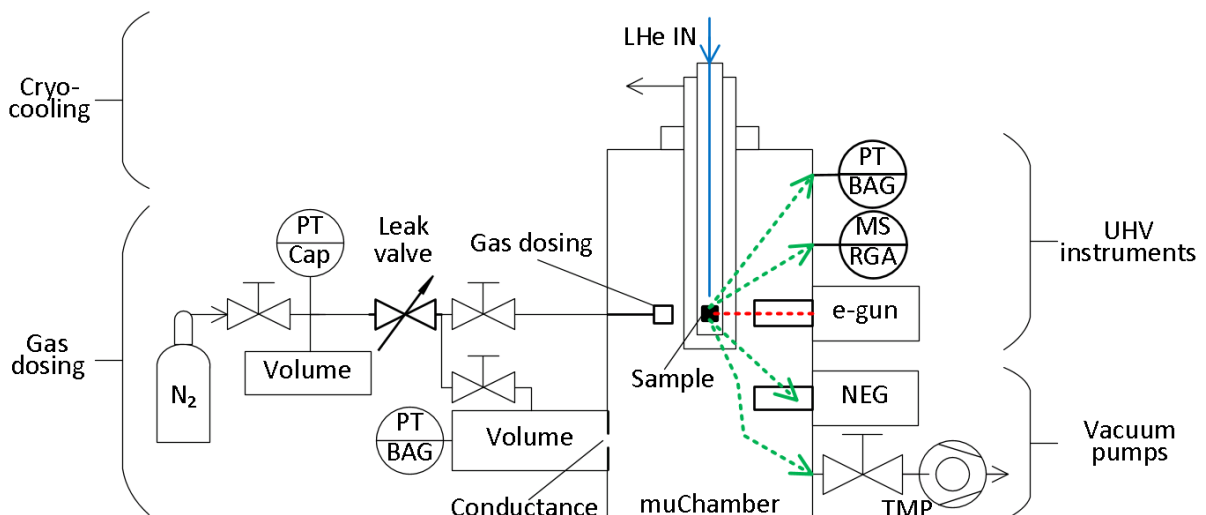


Figure 7: Simplified scheme of the experimental setup: Helium cooled sample with a layer of condensed gas is bombarded by electrons. Desorbed gas (green dashed line) is measured by the mass spectrometer and Bayard-Alpert gauge. Pumping is done by a turbopump and a getter.

The sample can be cooled to a temperature as low as 10 K using liquid Helium in an open cycle cooling loop or heated up to 500 K using resistive heating. The range

of temperatures $10 \div 90$ K is low enough to allow gases such as O_2 , N_2 and H_2 condense on the cold surface of the material sample. The injection of gases into the chamber and onto the sample is realised by a gas dosing system, which releases gas from the closed volume through a leak valve into the UHV of the mu-chamber. The gas is then sprayed over the sample using a retractable gas dosing tube which is placed closely over the sample surface. The amount of gas dosed into the chamber can be estimated from a measured pressured drop in a known volume measured by a capacitance gauge. Another approach to determine the exact coverage of the gas, which was effectively adsorbed onto the cold sample, is by analysis of a temperature programmed desorption curve.

To conclude, the ESD measurement requires faultless parallel operation of many subsystems and their stable and precisely controlled performance. The critical systems are in particular:

- Ultra-high vacuum generation
- Liquid helium cooling
- Electron gun operation
- Residual gas analyser
- Data acquisition system

Other support systems are:

- PLC controlled bake-out system
- Load-lock mechanism for sample insertion
- Electro-pneumatic interlocking system

4.2.1 Arrangement of instruments

The arrangement of the main components within the mu-metal chamber is shown in Figure 8. The cryomanipulator descends into the chamber from the top and features two sample-holding positions. Both holders are electrically insulated from the rest, so it can be floating at different electric potential and electron current from the sample can be easily measured.

Sample in the 1st position is held on a copper block which ensures thermal contact with the liquid helium and with a resistive heater. It is also equipped with thermal shield that opens to insert a sample and then closes to optimize thermal conditions of the sample. The sample holder in the 2nd position serves for calibration purposes and does not have the possibility of controlled cooling or heating. The other side of the cryomanipulator holds 2 concentric faraday cups also serving as calibration targets for the electron gun.

The adjacent wobblestick is used to open the thermal shield while inserting a sample and to tighten the sample in the holder for good thermal contact. Another manual manipulator transfers samples linearly and extends from the left side. With a 1 m long stroke it extends through an all-metal gate valve on the right side of the main

chamber, reaches into the storage chamber and brings a sample in. A bayonet lockout mechanism ensures a tight grip around the flag-style holder of the sample while manipulating it.

The electron gun faces the cryomanipulator from the front, so a sample can be placed in position and brought to precise alignment with the gun's axis. Another faraday cup is pivoting around the nozzle of the gun and can be manually closed when needed.

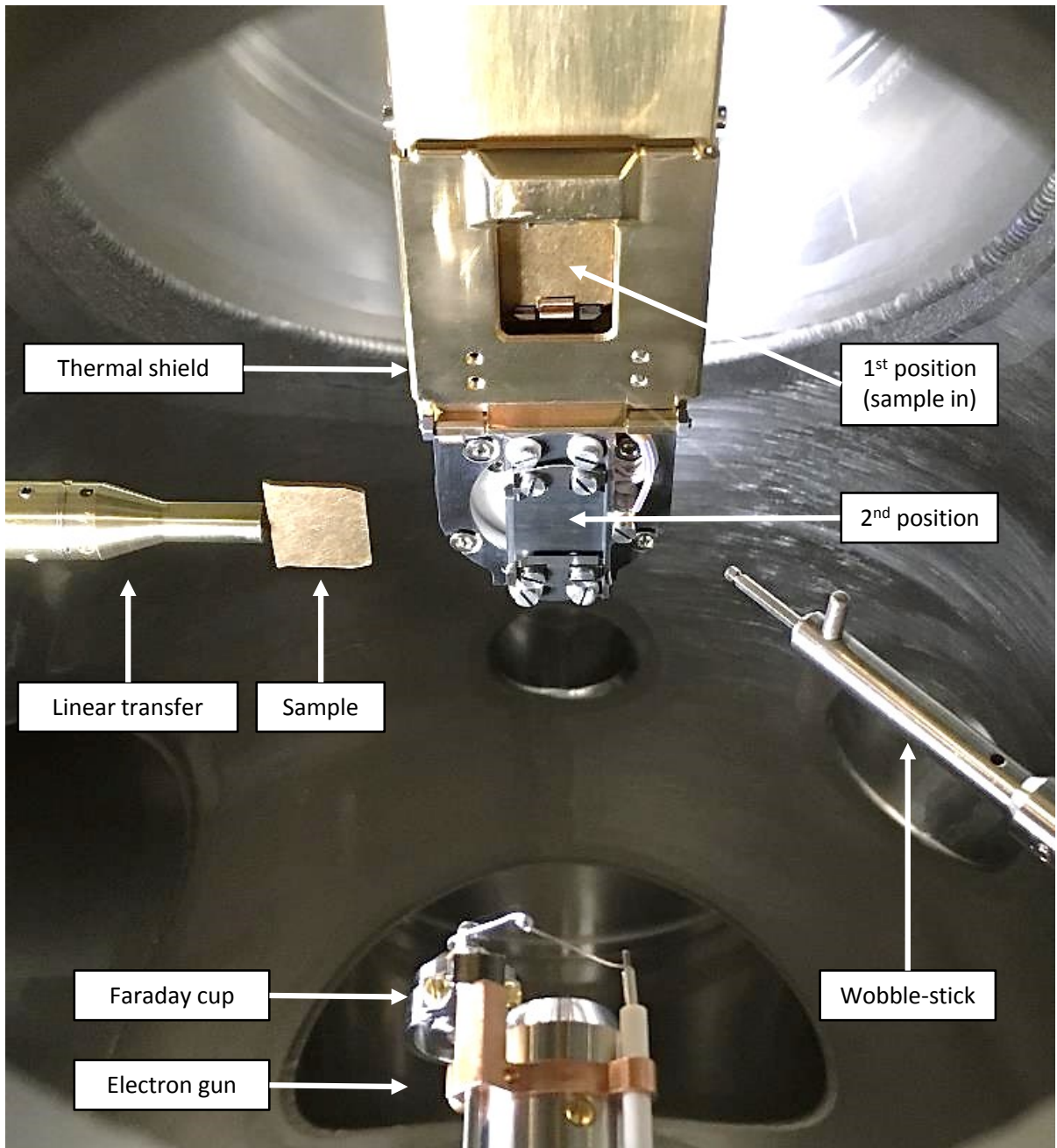


Figure 8: Instruments' arrangement of the experimental mu-metal vacuum chamber.

4.4 Mu-metal vacuum chamber

The key component of this setup is the vacuum chamber. This chamber was designed specifically to meet the needs of this experiment. It is constructed from mu-metal, which is a nickel-iron alloy with exceptionally high permeability [52] that shields the inside from static or low-frequency magnetic fields.

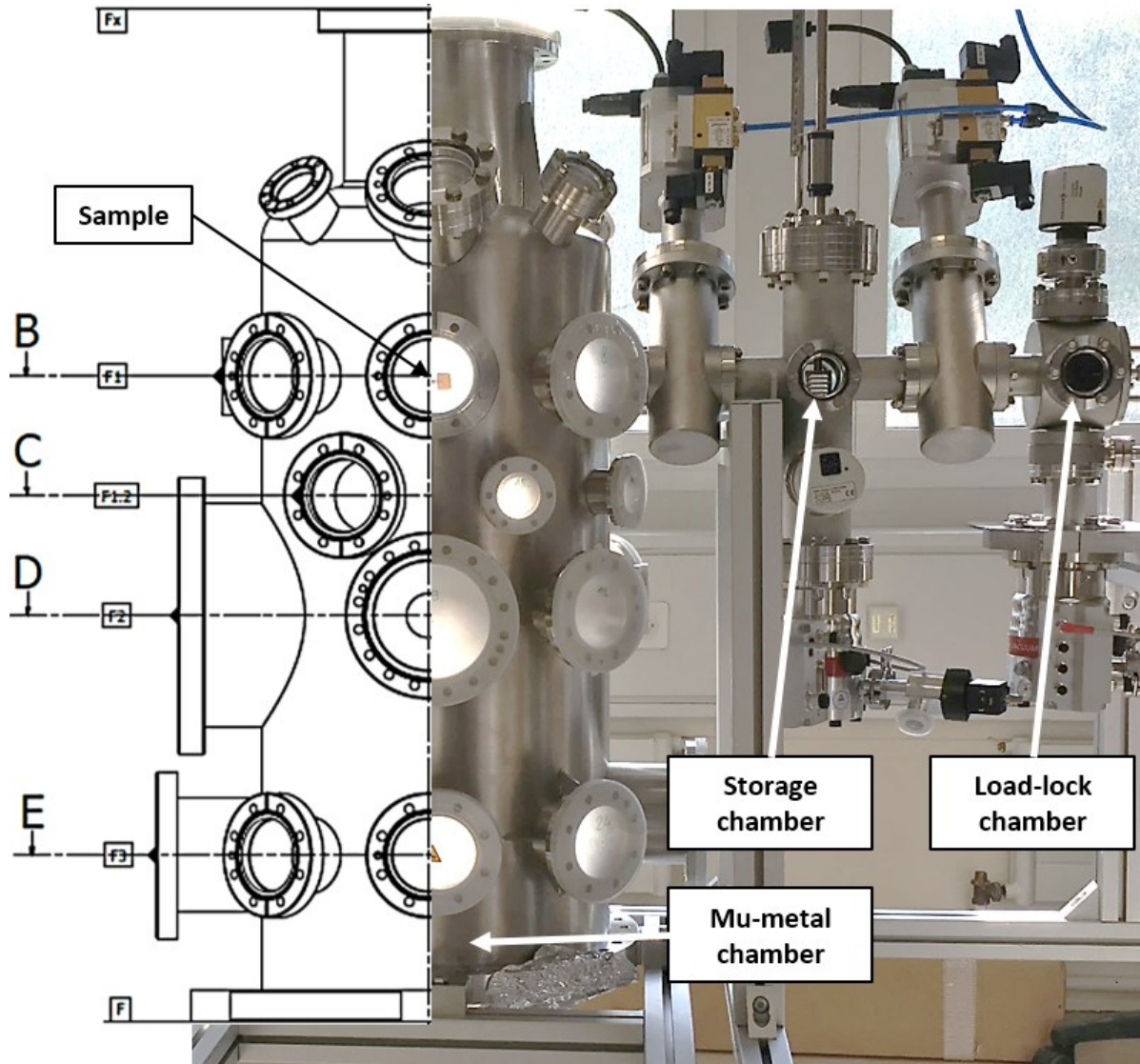


Figure 9: The mu-metal vacuum chamber during its installation into the setup. The 2 stage Load-lock system is assembled on the right side of the image. Note that flanges are positioned within the chamber in 4 principal planes marked B to E.

The chamber has 27 ConFlat (CF) flanges of different sizes from DN40CF to DN300CF to accommodate various instruments, which are positioned in a radial arrangement in 4 major horizontal planes. This layout is designed to complement the range of movement of the cryogenic manipulator, which is mounted on the top DN150CF flange. Planes marked as B, C and D in Figure 9 are placed within reach of the cryomanipulator and thus house instruments that need to be in direct view

or even contact with the samples, such as the wobble stick, gas dosing system or the electron gun. Plane B being the main one is in line with the sample insertion assembly, which is marked on the right side as Storage and Load-Lock chambers. The linear transfer is also mounted in this plane, it extends from the left and transfers samples from the storage chamber into different positions on the cryomanipulator. Plane marked as E is dedicated to support systems, which do not need to be within reach, such as pressure gauges, vacuum pumps, venting valve and a burst-disc. The top part of the chamber is equipped with flanges skewed by 45° from the vertical axis, which are fitted with viewports to have a visual frame of reference while manipulating samples. The 2-stage Load-lock assembly equally has viewports for this purpose.

4.5 Cryogenic manipulator

Another essential part of the setup is the cryomanipulator, which holds the sample and cools it down to 10 K. Such cryogenic temperatures are achieved using liquid helium cooling. Customized cryogenic manipulator was designed and built specifically for this purpose. The cryomanipulator is capable of a precise motorized and manual motion in 3 linear axes and 1 rotational axis as depicted in Figure 10. The range of vertical movement in the Z axis is 300 mm, the X and Y axes in the horizontal plane move by ± 12 mm. The angular range of the Rz rotational axis is limited to $\pm 176^\circ$.

This range of movements was chosen with regards to the design of the vacuum chamber, which has instruments arranged radially in 4 different planes, out of which 3 are accessible by this manipulator. The bottom plane which remains inaccessible is dedicated for pumps, pressure sensors, venting valve and other parts that do not need to be within reach. A set of 4 stepper motors which are actuating the manipulator axes is powered by controllers supplied by the manufacturer. These controllers provide a feedback control over the motors' motion and offer advanced functions such as cycling motion and an anti-backlash compensation. It was verified that the anti-backlash system effectively improves the repeatability of positioning in the X, Y and Rz axes.

The actuators and guiding rods are placed in the exterior of the manipulator, so the movement has to be transferred into the ultrahigh vacuum. This is done using bellow tubes for the 3 linear axes. The rotational movement is transferred through a differentially pumped rotating flange. The differential pumping is done in two stages separated by rubber seals. The outer stage is pumped to a low vacuum by an Edwards RV-12 oil pump and the inner stage operates at high vacuum created by a turbomolecular pump Pfeiffer HiPace80. Such engineering solution works very effectively and almost no pressure bursts are observed in the ultrahigh vacuum of the chamber while rotating the flange or when moving linearly in X, Y and Z axes.

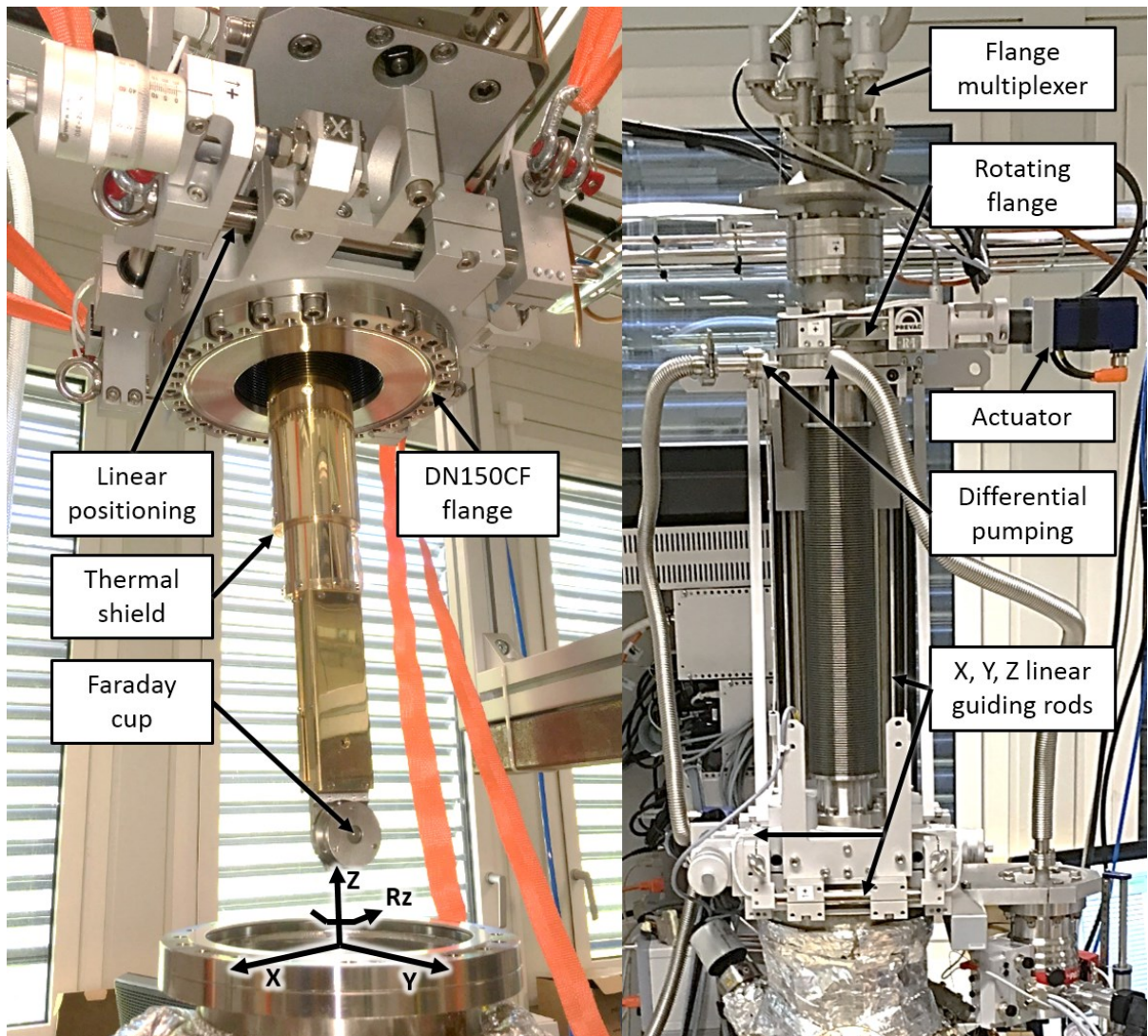


Figure 10: Cryomanipulator during installation and in place on top of the vacuum chamber.

Various parts of the cryomanipulator are electrically insulated using ceramic or polymer interpieces, except for the cryocooled sample holder, which sits on a sapphire plate. This allows to not only bias different components to different potentials, but also to measure an electrical current that they collect or emit. When a positive potential is applied on a component with respect to the grounded frame, electrons are collected on its surface. Conversely, negative potential can be applied to repel electrons, secondaries included, if required by each specific measurement.

The top part of the manipulator has a flange multiplexer, which houses vacuum feedthroughs with BNC-type connectors, that conduct the electrical current across the atmosphere-vacuum boundary. These BNC connectors then lead further to the DAQ chain, which consists of biasing batteries, current amplifiers and voltage analogue-digital converters.

4.6 Vacuum generation

The ultimate pressure of an ultrahigh vacuum chamber is given by the ratio of gas load and effective pumping speed. Pumping speed in a vacuum system is costly and technically limited to couple thousand l/s at the maximum. On the other hand, outgassing of materials spans over many magnitudes. As a result, choice of materials with very low outgassing is a must in order to achieve an ultrahigh vacuum. This indeed has to be complemented by appropriate vacuum pump and enhanced by other tricks to lower the ultimate pressure, such as a bakeout. The limiting factor in case of a baked UHV chamber is the thermal outgassing in front of the others.

There are different sources of gas load in a vacuum system, which are well explained in literature regarding UHV, such as Weston [54] and Jousten [55]. Other invaluable resource is Yates [56] who summarizes a great amount of UHV know-how related to everything from maintenance, or motion transfer to instrument's operation.

4.6.1 Turbomolecular pump

The vacuum chamber is pumped by Pfeiffer HiPace300, which is a large turbomolecular pump with a drag stage offering an ultimate pressure lower than 1.10^{-10} mbar and a large pumping speed of 270 l/s of N_2 equivalent. This turbopump is then backed with an oil rotary vane pump Edwards RV-12, which is roughing the fore-vacuum to an ultimate pressure of 5.10^{-3} mbar. The vacuum system has roughly 70l of volume and 2 m^2 of surface area and this combination of pumps is capable of evacuating it from an atmospheric pressure of 10^3 mbar down to 10^{-6} mbar range within 1 day, depending on circumstances. This, however, is not a standard operation as the system does not need to be vented, except for maintenance, and the sample is normally inserted through the 2-stage Load-lock.

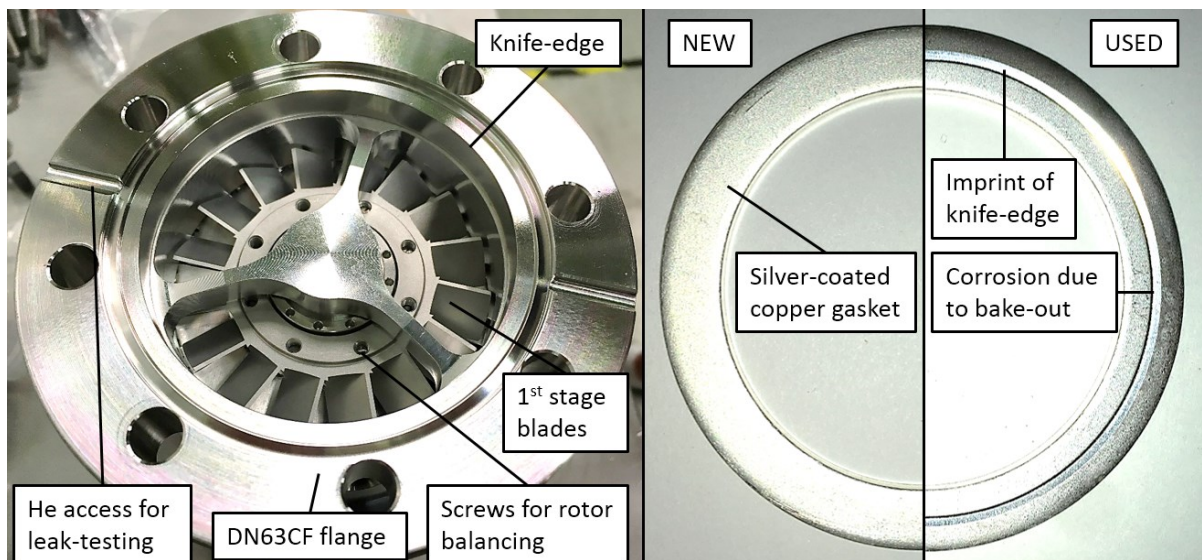
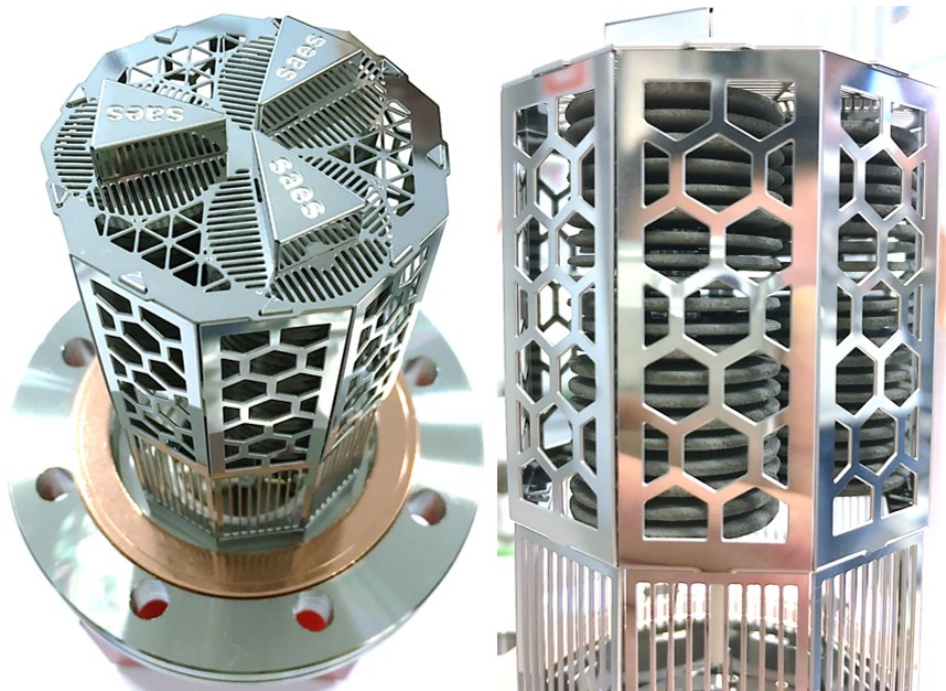


Figure 11: Pfeiffer HiPace80 turbomolecular pump and silver-coated gasket used in CF flanges. The right picture shows a silver-coated gasket used in a CF flange that has undergone a bakeout. Apart from the knife imprint a slight oxidation is visible

on the atmospheric side and is much more profound in non-silver coated gaskets. Besides that, the silver coating allows safe performance during multiple high temperature bakeouts.

4.6.2 Getter pump

A non-evaporative getter (NEG) pump was later added into the setup to be used preferably before the turbomolecular pump in the UHV region for its maintenance-free operation. Getter pumps use the principle of absorption of gases into the bulk material. Non-evaporative getter material is usually either sputter-deposited on parts, or sintered from powder metal into form of pellets, which are then stacked into a cartridge. This widely used type of pump comes in many forms ranging from simple coatings, deposited on inner surface of a chamber, to combined pumps as seen in Figure 18. Model NEX Torr 500 was used in the setup, which is a NEG pump combined with small ion pump offering a pumping speed of 500 l/s for hydrogen. As getters only adsorb some gases, a small complementary ion pump is incorporated in the body of the NEX Torr pump to capture CH_4 and noble gases.



*Figure 12 : NEX Torr 500: a NEG pump combined with small Ion pump.
Cartridge filled with sintered metal pellets is visible on the right.*

Activation procedure is required for the pump to begin operation. This is done by heating up the getter material to activation temperature of hundreds of degrees Celsius, when passivated surface layer is diffused into the bulk or pumped by another type of pump. The getter pump does not need any further energy supply after activation for it to work. This makes them very reliable component with extremely low operational and maintenance cost. However, additional pumps need to be present in the system, as getters can only start pumping in the high vacuum region and need to be pumped on during their activation.

4.6.3 Analysis of the pump-down curve

Pump-down of a vacuum system is by itself an interesting process, which can provide a valuable information about technical state of a setup, especially when supported by an RGA spectra.

Comparison of such pump-down curves is plotted in Figure 13. The first stage of pump-down consists of a rapid volumetric displacement of the most part of the gas and is governed by viscous flow relations. The viscous flow regime is then replaced by a molecular flow regime at around 10^{-3} mbar, when the mean free path of a molecules extends enough to be comparable to the size of the vacuum vessel. The curve then decreases at much slower rate, which is plotted as a line in a log-log chart and represents exponential dependency of degassing from inner walls of the vessel. The blue line represents a maiden pump-down of the mu-metal chamber and features small bumps caused by variation of thermal outgassing with room temperature. The green curve shows how the system was vented with N_2 for a quick maintenance and pumped-down again. The much faster decay of the green curve as compared to the blue one is thanks to a memory effect of the vacuum chamber's outgassing. Finally, the red curve depicts a pump-down after installation of the cryo-manipulator, which is similar to the first pumping of the chamber alone.

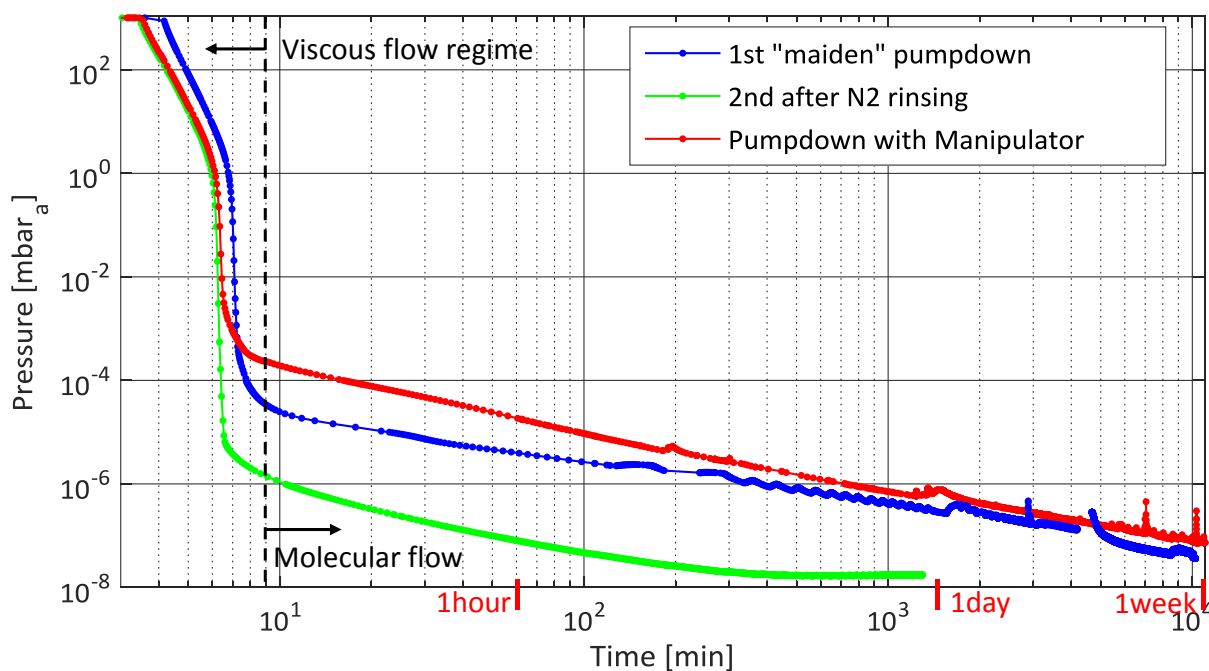


Figure 13: Measured pump-down curve of the newly assembled setup. Note the log-log scale.

Note that the pumping is less efficient and that decreasing base pressure of the system by 1 order of magnitude requires 1 more order in the time-scale. This imposes a need of other means of decreasing the base pressure than bare pumping of the setup at ambient temperature. Since installation of additional pumps is costly, further reduction of pressure is achieved by a bakeout.

A Helium leak-test was done over the entire chamber after it was pumped down under 10^{-6} mbar. The test showed no measurable leaks up to the background of $4 \cdot 10^{-10}$ mbar.l/s and is considered satisfactory. Other indication on leak-tightness of the setup comes from the mass spectra of the residual gas, which is analysed later.

4.7 Bakeout procedure

A so-called bake-out is a procedure commonly used as an effective way to decrease the ultimate pressure of all-metal vacuum chamber by temporarily elevating the temperature of the whole setup. The temperature rise stimulates desorption of molecules normally bound to the surface with a long sojourn time and it also provides a qualitative improvement of the vacuum in terms of the residual gas composition.

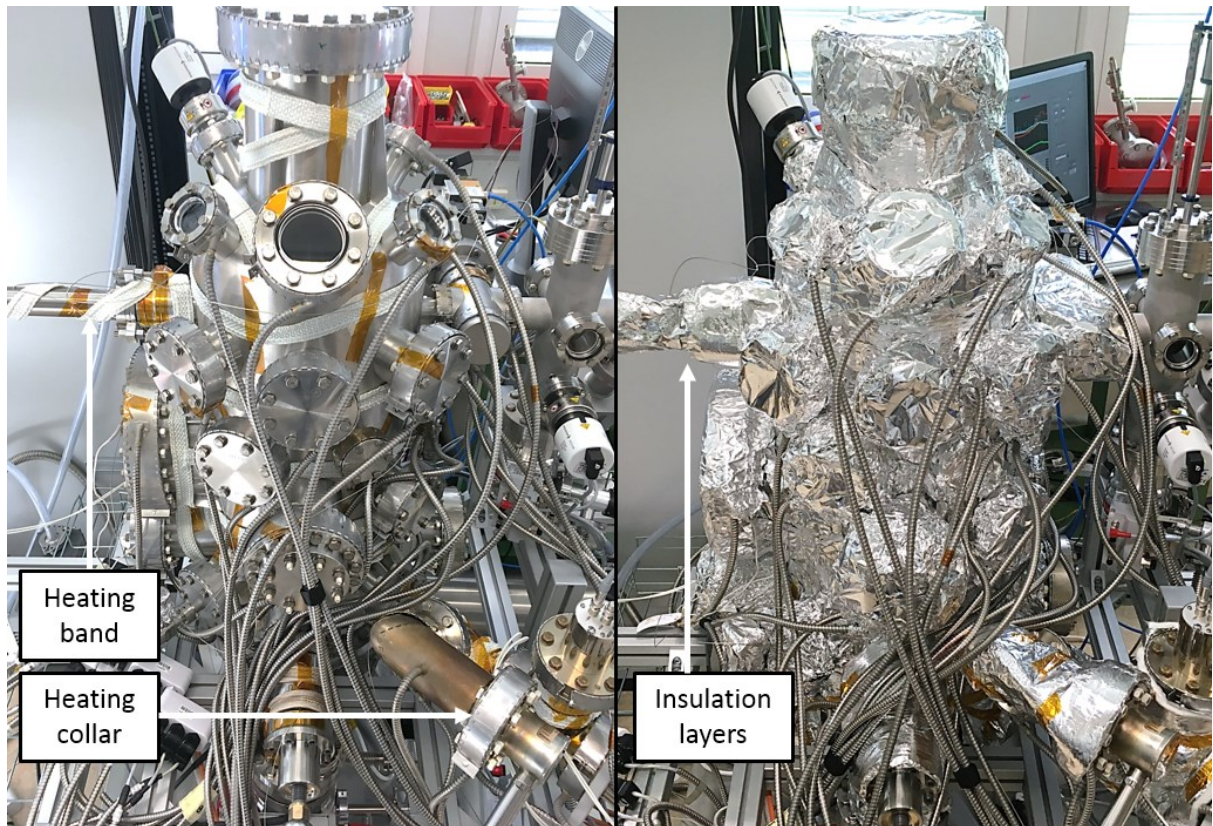


Figure 14: View of the experimental vacuum chamber during bakeout equipment installation.

A considerable improvement of the base pressure is observed after the bakeout once the system is at room temperature again. It also cleans the setup from remnants of detergent, oil traces, water and other possible contaminants. All molecules which are desorbed from the heated surface are either pumped away from the system by a vacuum pump, or re-adsorbed at parts which are kept at lower temperature. Another goal is to clean and degas vacuum gauges from contaminants that they adsorbed during their exposition to a humid atmospheric air. A good bakeout procedure results into a background gas composition dominated by hydrogen, which

is the main residual gas that outgasses from the bulk metal. Shall this not be the case and the residual gas spectra is dominated by water, nitrogen or argon, it may as well indicate a leak, virtual leak or a strongly outgassing component.

4.7.1 Bakeout realisation

A vacuum setup usually consists of numerous parts with different temperature limitations. The following Table 2 lists main parts of the vacuum setup, their respective target temperatures and assigned programs.

Table 2: List of used bakeout programs for different components.

Maximum [°C]	Target [°C]	Ramp [°C/hour]	Components	Program [#]
400	350	80	Hot cathode ion gauges: RGA and BAG	5
300	250	50	Linear transfer	2
250	200	50	Electron gun, wobble-stick All-metal valves, tubes, etc.	8
150	150	50	Mu-chamber (max 250 °C), Cryomanipulator, NEXTorr pump	7

Four different bakeout temperature profiles were created to fit these requirements. This data is then programmed into a PLC-controlled bakeout rack, which comprises of 24 channels operated separately to reach a target temperature given by the assigned program.

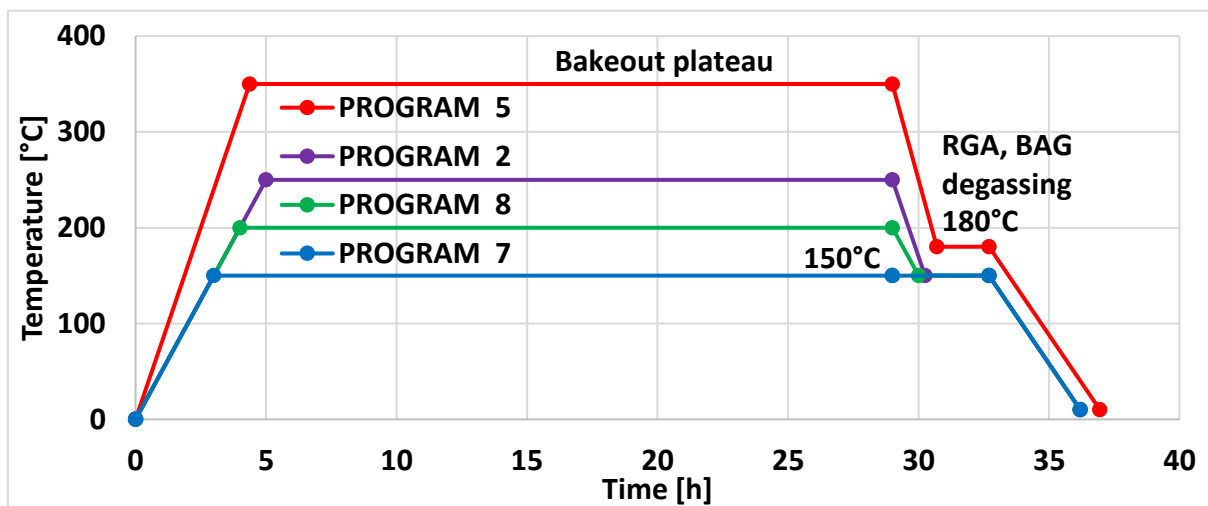


Figure 15: Temperature profile during bakeout and degassing plateau. Note that UHV instruments are always the hottest part of the whole setup to ensure cleanliness.

The temperature is measured by a type E thermocouple placed under each heating element. Two-position regulation is done by a relay, that switches heating elements ON and OFF as needed. The heated mass of a component has a large thermal inertia, thus averages these discrete regulation cycles and follows the desired temperature profile.

The end of a bakeout is usually followed by degassing of UHV instrumentation, such as RGA, BAG and by activation of NEG pump if any. Pressure bursts resulting from such degassing can be seen in Figure 16 at the end of a bakeout plateau.

4.7.2 Bakeout results analysis

The evolution of pressure and temperature of the mu-chamber during a simple bakeout is plotted in Figure 16. The temperature ramps up at a given rate to the target temperature, which is at least 150 °C. The temperature rise enhances desorption and outgassing from the entire inner surface of the setup, which is being baked out. This is followed by a pressure rise by 2 orders of magnitude, as the pumping speed of the turbomolecular pump is constant in this range, but the gas load increases considerably. The pressure slowly decays during the 1 day-long bakeout plateau, as the surface gets gradually depleted of impurities.

The bakeout is stopped when the pressure decay is negligible and its slow improvement is not worth the extra time. The temperature is then ramped down to a short plateau at 150°C, where UHV instruments are turned on and degassed. The RGA and BAG are both hot cathode gauges, which are formed by a heated tungsten filament and a grid. Gas particles are evaporated from the surface, when the filaments is heated up and electrons start bombarding the grid. This effect is followed by a short pressure burst during the cool down.

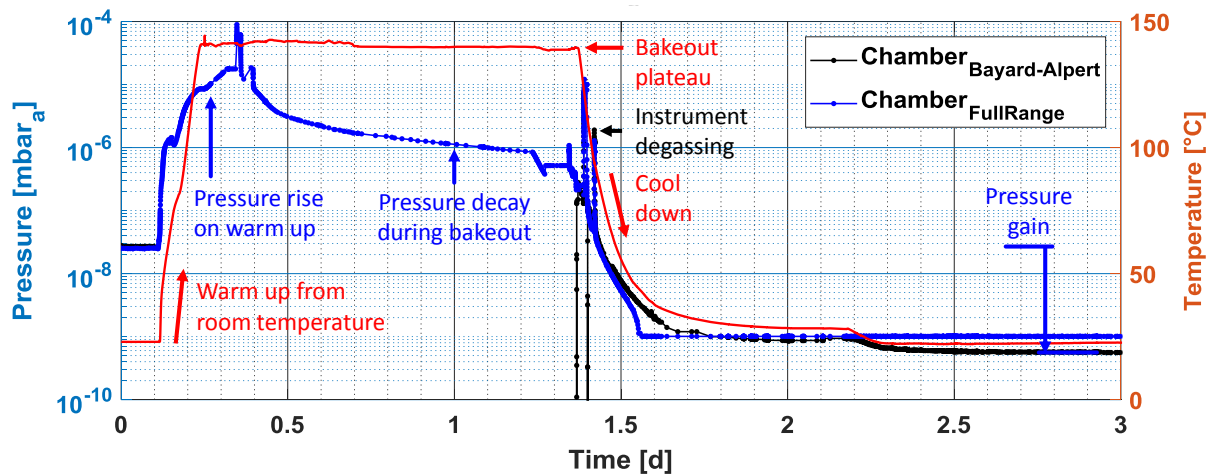


Figure 16: Evolution of pressure and temperature during 1 day long bakeout at 150 °C. Note the semi-log scale and the pressure gain of roughly 1.7 orders of magnitude.

Finally, the base pressure of the setup is severely reduced, when the system cools down back to the room temperature. The bakeout procedure resulted into a reduction of pressure by a factor of 150 in this particular case. Such pressure and residual gas composition would be hardly achieved without a bakeout. Any alternative solution without a bakeout would be costly in time or resources, as it would imply either extensive pumping time or installation of excessive pumping speed.

4.7.3 Mass spectrum comparison

The vacuum chamber was vented prior to the bakeout for equipment installation, meaning that atmospheric gases, such as N_2 , O_2 , H_2O , CO_2 and Ar entered the volume. Most of the gas species are easy to pump away with a turbomolecular pump, unlike the H_2O molecule. It is difficult to get rid of due to its a long sojourn time, caused by its relatively high binding energy and low temperature.

Residual gas analyser was used here to investigate the bakeout efficiency in improving the vacuum both quantitatively and qualitatively. Mass spectra was taken prior and after the bakeout process. Figure 17 overlays both spectra for better comparison and marks the most dominant residual gases. The blue spectrum was taken before bakeout, that is at high pressure, using the RGA in Faraday mode.

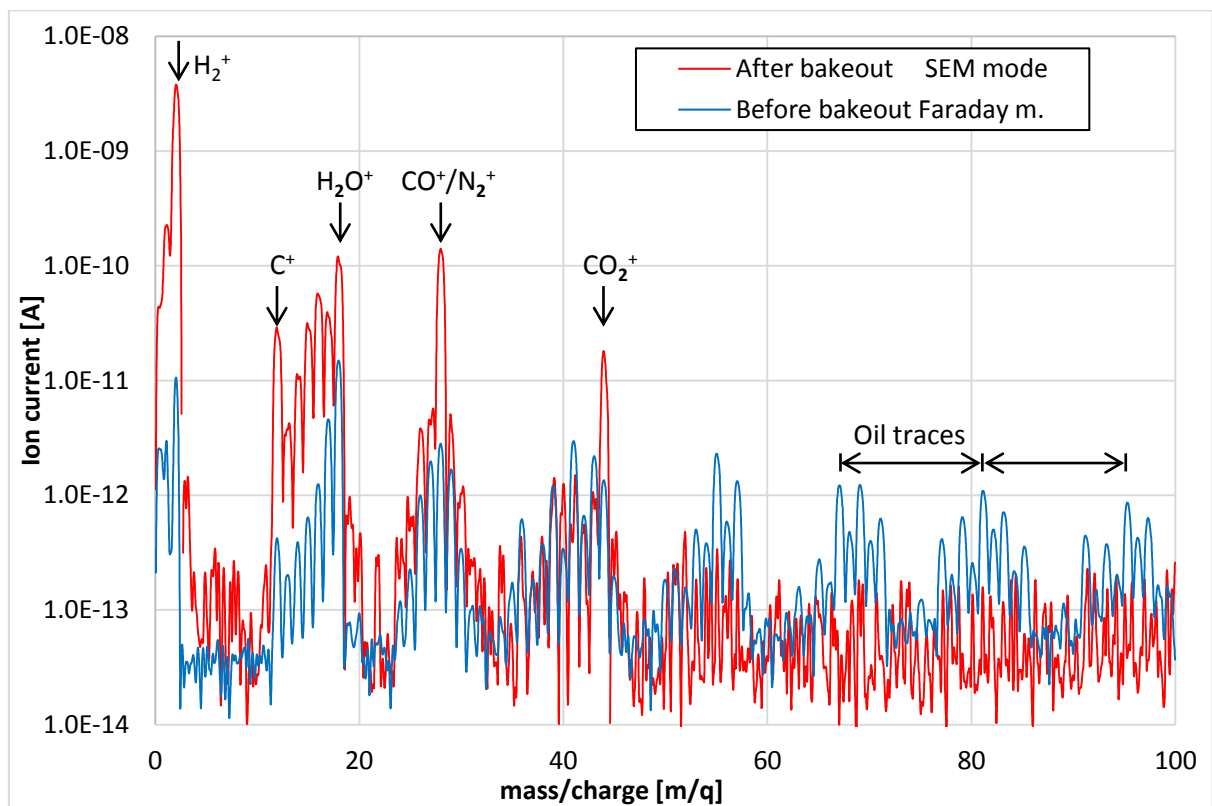


Figure 17: Mass scan before and after a bakeout. Note that the dominant residual gas is H_2O before bakeout and H_2 afterwards.

The pre-bakeout spectrum is dominated by H_2O , due to its long sojourn time. If the temperature is elevated during a bakeout, the sojourn time of any molecule decreases, making the molecules more mobile and easier to pump away from the vacuum system. The sojourn time of water decreases by several orders of magnitude just by heating the setup from ambient temperature to $150\text{ }^\circ\text{C}$.

The same effect applies to oil traces that are present at higher masses between 50 and 100 m/q. Hydrocarbon are composed of linearly attached units $-CH_2-$ units, which have a mass 14 g/mol. Hence the characteristic groups of peaks with a periodicity of 14 m/q, which are a sign of residual pollution after components cleaning.

The red colour traces a spectrum of the residual gas taken after a 150 °C bakeout lasting for 24 hours. This temperature and time was enough for sticky gas species to desorb and be pumped away by the turbomolecular pump. The spectrum was measured with a secondary electron multiplier (SEM) set to 1600 V, which enhanced the RGA's sensitivity in the UHV region by several orders of magnitude. This is why the red signal is much higher, despite the much lower pressure at which it was taken. As the H₂O effectively disappears from the spectra, it becomes dominated by other gas species which outgas from the chamber walls, such as mostly H₂, but also CO₂ and its fragments.

4.8 Liquid Helium cooling

A choice had to be made between open and closed cooling cycle, each bearing its advantages and disadvantages. The closed cycle helium cooling in laboratory applications usually has the form of Gifford-McMahon cycle [53], which uses a reciprocating piston. In spite of undoubtful advantages of such systems, such as easy operation, the moving piston is a potential source of vibrations in the measurement setup and as such undesirable. As a result, an open cycle liquid Helium cooling is used to cool the sample to cryogenic temperatures using a custom-built cryogenic manipulator.

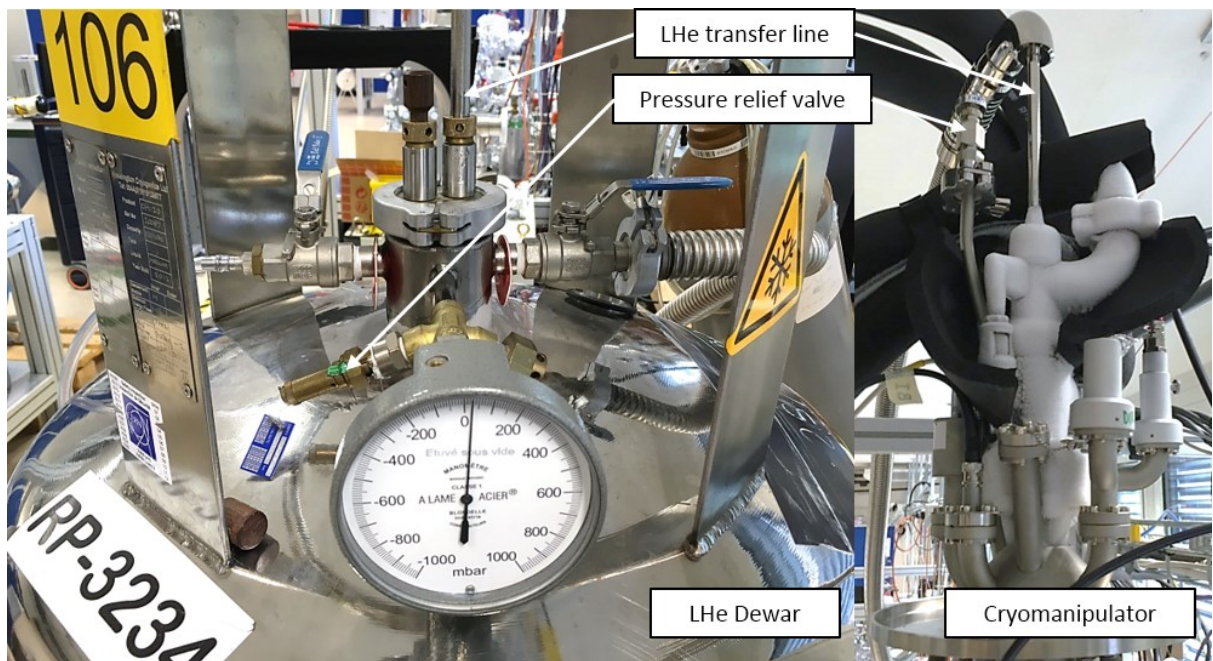


Figure 18: View of LHe Dewar and cryomanipulator with a transfer line in between.

The material sample is mounted on the cryomanipulator via a holder that has dielectric sapphire plate attached on an OFHC copper block. This copper block has a diode temperature sensor placed within and serves for conducting the heat towards the SS tubing, where the liquid Helium evaporates. The saturation temperature is 4.2K at the pressure of 1.0 bar_a, but thermal impedance causes the sample to be warmer

than that, with a minimum temperature of about 10 K. Figure 18 shows the setup in operation, note the icing on the flange multiplexer on the top of cryomanipulator.

The cooling circuit of the experiment is schematised in piping and instrumentation diagram in Figure 19. The liquid Helium is supplied to the experiment from a Dewar container, which is also used for transport. It is transferred into the cryogenic manipulator through a vacuum-insulated line, which reaches from the bottom of the Dewar and conducts all the way to the bottom of the cryomanipulator.

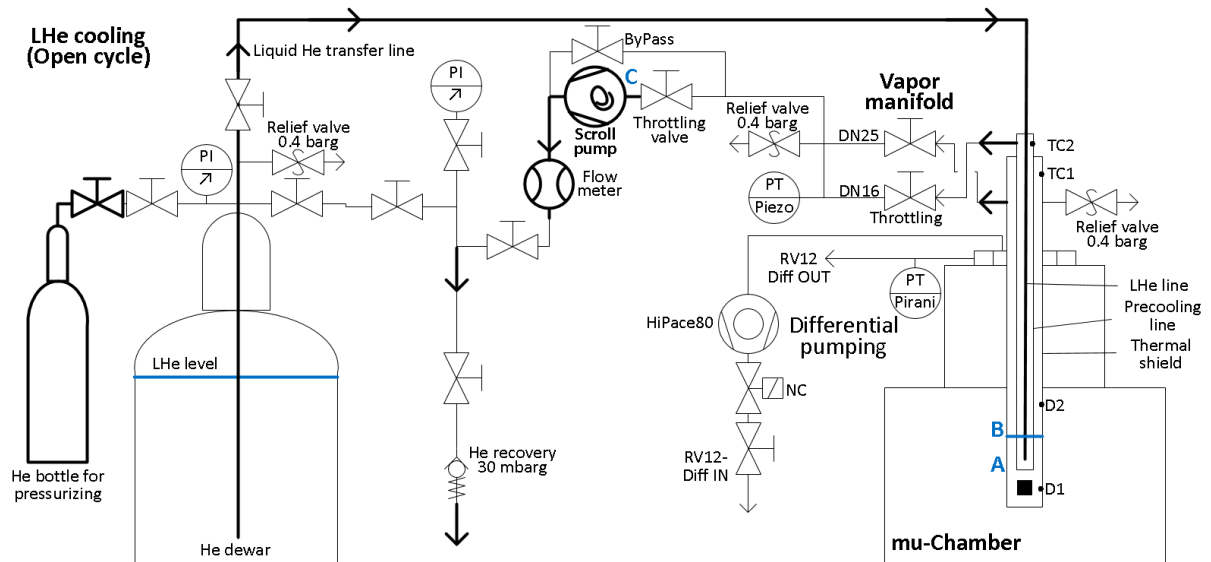


Figure 19: Piping and instrumentation diagram of the open cycle liquid Helium cooling.

The evaporated Helium is then channelled through a tube, which forms a thermal shield for the inner liquid transfer line. The inner liquid line also has another concentric tube around that serves for precooling. Two valves are present on the vapor outlet to control the flow of helium through the thermal shield or the precooling tube. The vapor exiting the insulated part has temperature around 100 K when it reaches the flange multiplexer at the top of the manipulator.

Two modes of operation of the open-loop cooling were examined. The first mode involves over-pressurising the Dewar container to $p_D = 1.2 \text{ bar}_a$, to create pressure difference forcing Helium through transfer lines and cryomanipulator into the helium recuperation piping. This regime of operation is difficult to control as the Dewar has to be closed and pressurized from an external Helium bottle and any valve manipulation changes pressures and temperatures within the circuit.

Another mode of operation was developed using a scroll pump to create the pressure difference, while keeping the Dewar container open to the recuperation line, thus maintaining it at $p_D = p_{liq} = 1.03 \text{ bar}_a$. The scroll pump placed on the vapour outlet generates an under-pressure needed to drive the Helium from Dewar through the cooling circuit. Resulting decrease in evaporation pressure also implies slight decrease of evaporation temperature by about 0.4 K, as seen in pressure-enthalpy diagram in Figure 20.

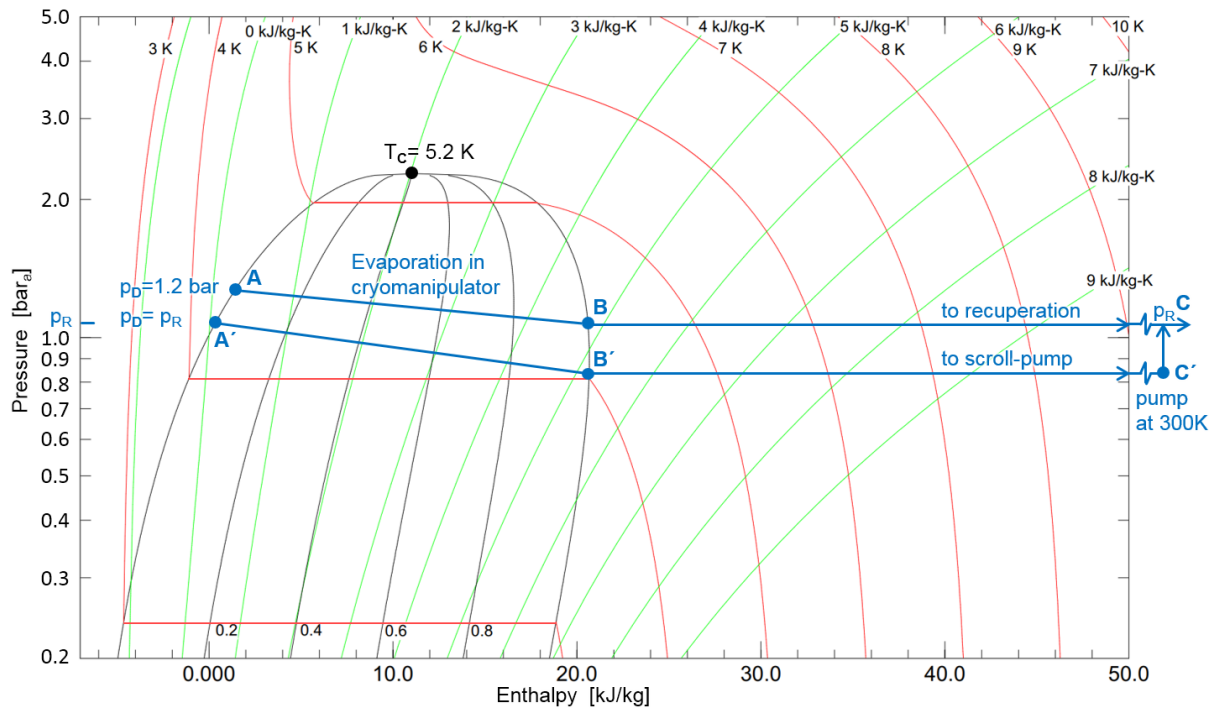


Figure 20: Refrigeration diagram of open cycle LHe cooling. Adapted from NIST RefProp [58].

Such cooling arrangement is safer, as the Dewar does not have to be pressurized, and has more stable performance, which is easily controlled via pump's user interface. It also results into a slightly faster cool-down and a severe reduction of liquid helium consumption in nominal operating conditions at 10 K. A safety by-pass valve and pressure-relief valves were added to the circuit to prevent pressure build-up in case of the scroll pump malfunction.

4.8.1 Cryo-pumping effect

A strong cryo-pumping effect was observed after cooling the cryomanipulator to temperatures lower than 20 K. Particles of the residual gas including H₂, N₂, CO are condensed and trapped on the cold surface. Gas injection manifold was used to inject nitrogen through a known conductance and measure the total effective pumping speed for to be around 4000 l/s of N₂ equivalent. This additional pumping speed resulted into decrease of the vacuum chamber's base pressure from 10⁻¹⁰ mbar range to 10⁻¹¹ mbar range. Such effective reduction of background is indeed desirable for measurement purposes. The pressure is expressed in N₂ equivalent according to the norm, despite that the dominating residual gas is H₂.

4.10 Gas injection and dosing system

4.10.1 General layout

The injection manifold composes of a known volume, a capacitance pressure sensor and a variable leak valve, as schematized in Figure 21. The volume is firstly evacuated below 10^{-6} mbar by an adjacent turbomolecular pump. The pump is then shut off by a valve, hermetically closing the volume. Another valve is used to inject a given gas into the volume up to a certain pressure, which depends on the desired amount to be injected.

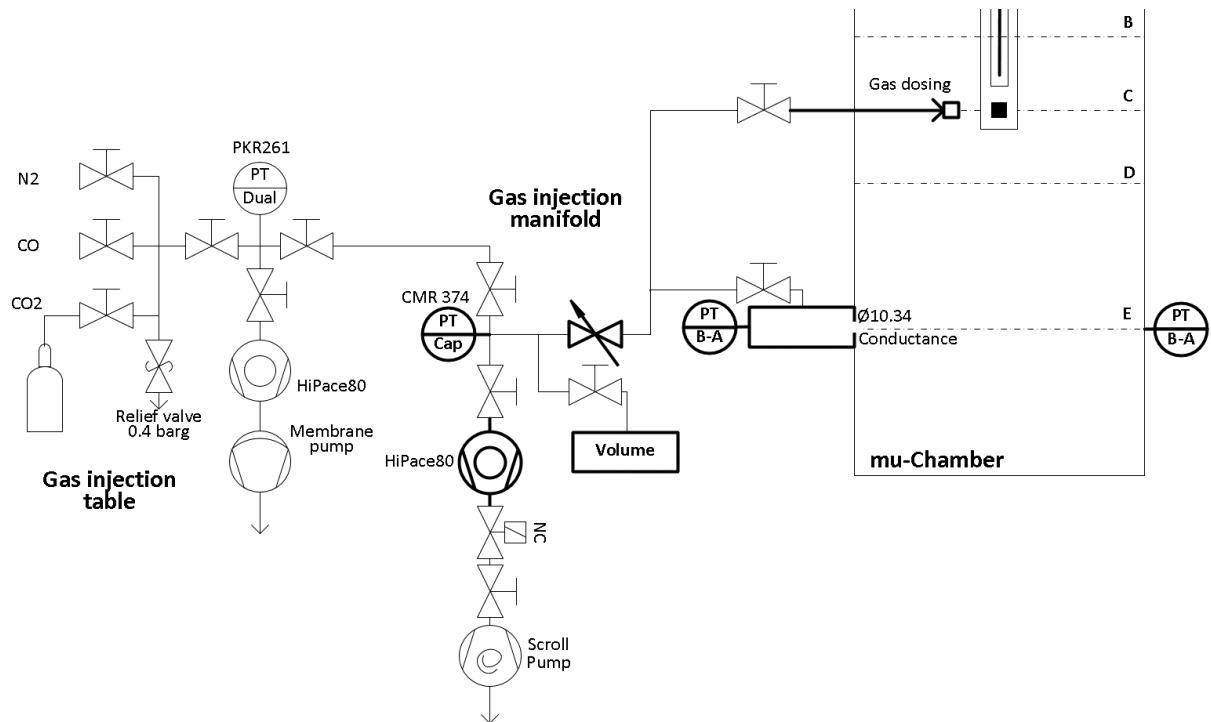


Figure 21: Piping and instrumentation diagram of installed gas dosing system.

The known volume now entraps a precise amount of gas, whose pressure is known, so the number of molecules is equally known. The variable leak valve doses small amounts of gas into the chamber, either through a known conductance equipped with a vacuum gauge, or by means of the retractable gas dosing tube.

4.10.2 Pumping speed measurement by gas injection

The gas injection manifold also serves for pumping speed measurement. Suppose that a nitrogen is injected through an orifice and the pressure is measured on both sides of an orifice by a calibrated vacuum gauge. The pressure is by much higher at one side of the orifice during an injection, so it can be assumed that the gas moves only in one direction from the high-pressure side to lower one. As presented in [55], the conductance C_j is calculated using the cross-sectional area A of the orifice and the mean thermal velocity of gas molecules. The conductance then expresses how

many litres of a gas with mass M_j at given temperature T cross the orifice per unit time.

$$C_j = A \cdot \sqrt{\frac{k_B T}{2\pi M_j}} \quad [l/s] \quad (4.1)$$

The injected gas flow can be determined knowing the pressure difference and the conductance of this orifice. The orifice is constructed from a thin sheet with a circular hole of a diameter $D = 10.34$ mm. The conductance is a function of the impinging rate of gas molecules on a surface. This imping rate depends on particles' mean square velocity, which is a function of particles' mass and temperature. Note that it scales with the square root of temperature divided by molar mass, as many other phenomena in vacuum science. This dependence is plotted in Figure 22. It shows the calculated conductance of an orifice for different molar masses and temperatures. This means that at 300 K, the conductance is 38 l/s for H_2 with mass 2 g/mol but only 10 l/s for N_2 or CO with mass 28 g/mol. This value is further reduced e.g. for CO_2 with mass 44 g/mol to about 8 l/s.

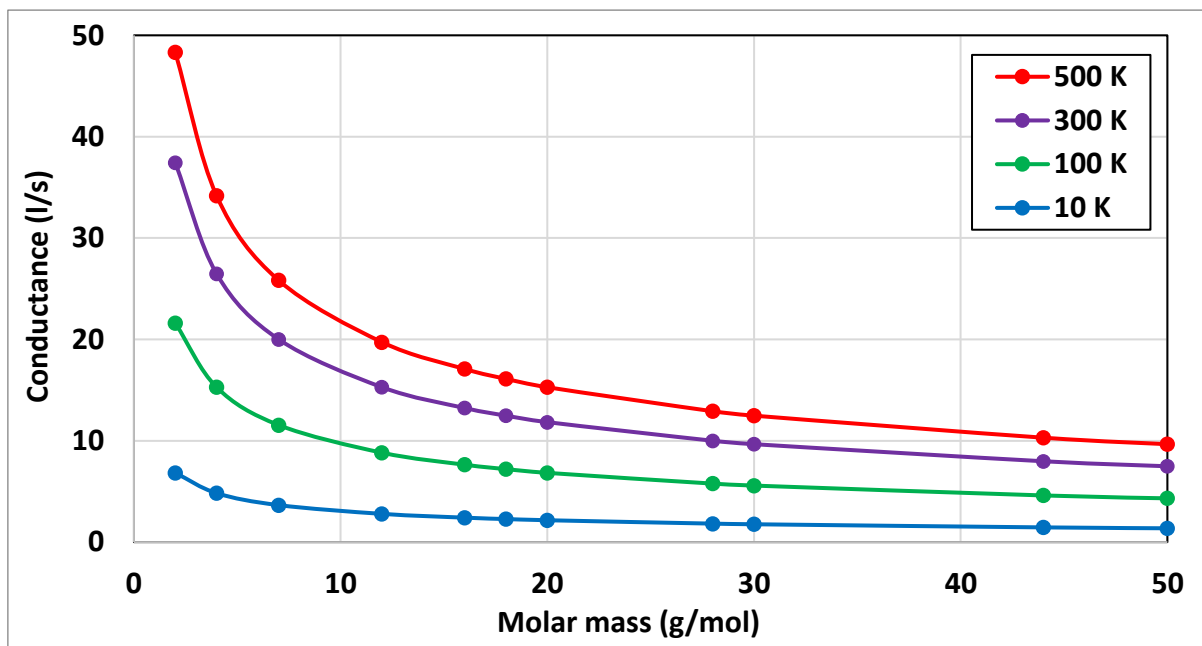


Figure 22: Vacuum conductance of a thin 10.34 mm circular orifice calculated for different masses and temperatures.

4.10.3 Pumping speed measurement

Measurement was done to assess the effective pumping speed when the setup is at ambient temperature and when the cryomanipulator is at 10 K. Nitrogen was injected through the circular orifice with conductance $C_{N_2} = 10$ l/s. This resulted

in a pressure rise above the background on both sides of the conductance denoted as Δp_{inj} and a pressure rise Δp_{much} in the mu-chamber itself.

$$S_{eff,N_2} = C_{N_2} \cdot (\Delta p_{inj} - \Delta p_{much}) \quad [1/s] \quad (4.2)$$

Suppose that nitrogen is injected creating a pressure difference Δp above the background. Entire setup is at ambient temperature.

$$\begin{aligned} p_{much}^{BG} &= 4.0 \cdot 10^{-10} \text{ mbar} & p_{inj}^{BG} &= 6.0 \cdot 10^{-10} \text{ mbar} \\ p_{much} &= 5.2 \cdot 10^{-9} \text{ mbar} & p_{inj} &= 5.2 \cdot 10^{-8} \text{ mbar} \\ \Delta p_{much} &= 4.8 \cdot 10^{-9} \text{ mbar} & \Delta p_{inj} &= 5.1 \cdot 10^{-8} \text{ mbar} \end{aligned} \quad (4.3)$$

Calculating the gas load Q injected into the chamber through the conductance C_{N_2} :

$$\dot{Q} = C_{N_2} \cdot (\Delta p_{inj} - \Delta p_{much}) \quad [\text{mbar} \cdot \text{l/s}] \quad (4.4)$$

$$\dot{Q} = 10 \cdot (5.1 \cdot 10^{-8} - 4.8 \cdot 10^{-9}) \quad [\text{mbar} \cdot \text{l/s}] \quad (4.5)$$

$$\dot{Q} = 4.7 \cdot 10^{-7} \quad [\text{mbar} \cdot \text{l/s}] \quad (4.6)$$

The effective pumping speed for N_2 is expressed as the ratio of gas load Q being pumped at the pressure p_{much} .

$$S_{eff,N_2} = \frac{\dot{Q}}{p_{much}} \quad [l/s] \quad (4.7)$$

$$S_{eff,N_2} = \frac{4.7 \cdot 10^{-7}}{4.8 \cdot 10^{-9}} \quad [l/s] \quad (4.8)$$

$$S_{eff,N_2} = 97 \text{ l/s} \quad [l/s] \quad (4.9)$$

The same process and calculation is repeated when cryomanipulator is stabilized at 10 K and creates a strong cryo-pumping effect. Note that the rest of the setup is still at ambient temperature, thus the conductance does not change.

$$\begin{aligned} p_{much}^{BG} &= 3.2 \cdot 10^{-11} \text{ mbar} & p_{inj}^{BG} &= 6.9 \cdot 10^{-11} \text{ mbar} \\ p_{much} &= 7.4 \cdot 10^{-10} \text{ mbar} & p_{inj} &= 3.0 \cdot 10^{-7} \text{ mbar} \\ \Delta p_{much} &= 7.1 \cdot 10^{-10} \text{ mbar} & \Delta p_{inj} &= 3.0 \cdot 10^{-7} \text{ mbar} \end{aligned} \quad (4.10)$$

Calculating the gas load \dot{Q} from the known quantities:

$$\dot{Q} = C_{N_2} \cdot (\Delta p_{inj} - \Delta p_{much}) \quad [\text{mbar} \cdot \text{l/s}] \quad (4.11)$$

$$\dot{Q} = 10 \cdot (7.1 \cdot 10^{-10} - 3.0 \cdot 10^{-7}) \quad [\text{mbar} \cdot \text{l/s}] \quad (4.12)$$

$$\dot{Q} = 3.0 \cdot 10^{-6} \quad [\text{mbar} \cdot \text{l/s}] \quad (4.13)$$

Evaluating the combined effective pumping speed for nitrogen S_{eff,N_2} of installed pumps and the cryo-pumping:

$$S_{eff,N_2} = \frac{\dot{Q}}{p_2} \quad [l/s] \quad (4.14)$$

$$S_{eff,N_2} = \frac{3.0 \cdot 10^{-6}}{7.1 \cdot 10^{-10}} \quad [l/s] \quad (4.15)$$

$$S_{eff,N_2} = 4200 \text{ l/s} \quad [l/s] \quad (4.16)$$

The results clearly indicate that the profound cryo-pumping effect increases the effective pumping speed for nitrogen by a factor of 40. This is indeed a desirable effect, as it reduces the background pressure in the chamber and boosts the sensitivity of measurement to smaller ESD yields.

Another method of the gas load measurement is possible. Suppose that nitrogen is trapped in the small volume within the gas injection manifold, that is equipped with a sensitive capacitance gauge Pfeiffer CMR 374. This gas is slowly let through the leak-valve and through the conductance into the vacuum chamber. A pressure decrease Δp_V in a known volume V_{inj} over a period of time Δt_{inj} determines the injected gas load \dot{Q} .

$$\dot{Q} = \frac{\Delta p_V \cdot V_{inj}}{\Delta t_{inj}} \quad [mbar \cdot l/s] \quad (4.17)$$

Suppose that a pressure difference Δp_V of $1.6 \cdot 10^{-3}$ mbar is injected from a volume V_{inj} of 0.1 l during a time period Δt_{inj} of 16 minutes. Evaluation of the formula gives the following nitrogen injection rate:

$$\dot{Q} = \frac{1.6 \cdot 10^{-3} \cdot 0.1}{960} = 1.7 \cdot 10^{-7} \quad [mbar \cdot l/s] \quad (4.18)$$

This can be compared with the gas load \dot{Q} calculated from the pressure drop over the orifice, which is $1.0 \cdot 10^{-7}$ mbar in this particular case. This makes a good cross-check, considering all the possible sources of error. The small difference can be easily accounted for in further calculations.

This measurement procedure also enables parallel measurement of the RGA sensitivity to nitrogen, or any other injected gas and will be addressed further on.

4.10.5 Gas dosing

A custom-built gas dosing system was designed to deliver precise quantities of gas directly onto the sample surface, as well as to create a homogenous coverage of adsorbed gas. The end part is formed into a square extension, which fits the hole in the thermal shield covering the sample. This gas dosing tube was installed into a bellows linear transfer to be retractable. It approaches towards the sample as close as possible when a dosing is needed and then retracts by 10 cm away from the sample when measurements are being made or when a movement of the cryogenic manipulator is needed.

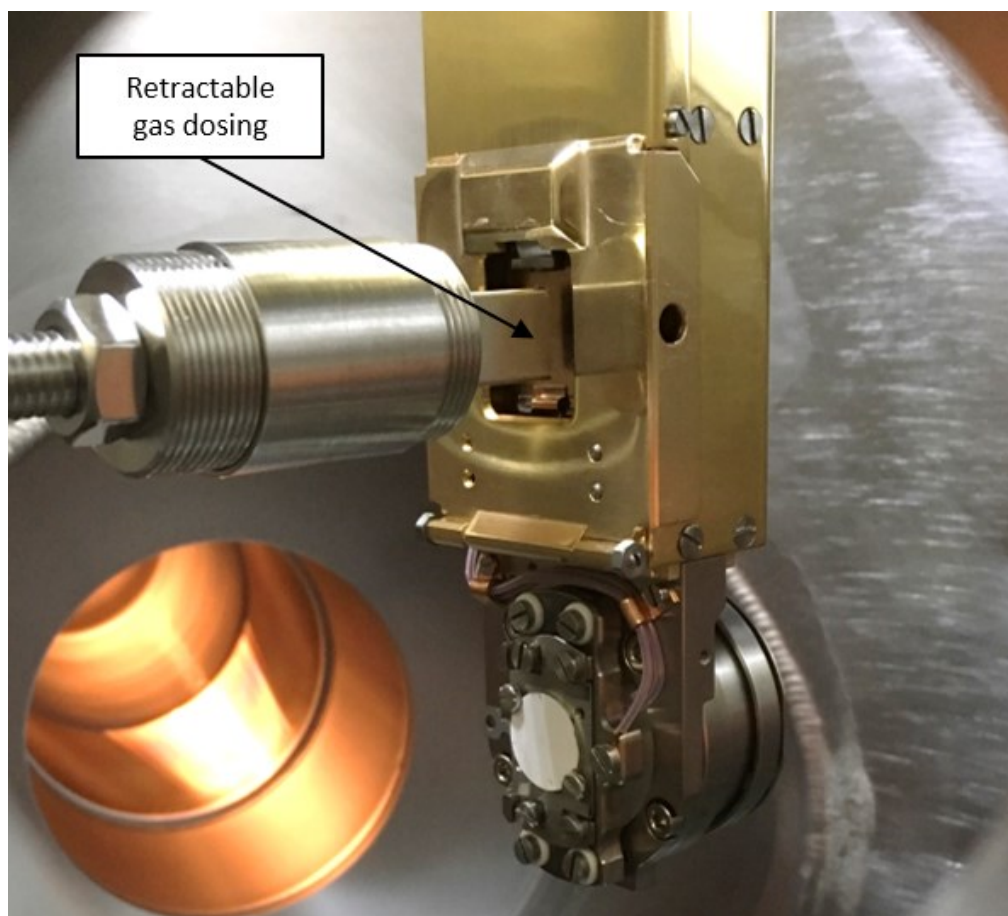


Figure 23: View of retractable gas dosing system approaching closely above the sample.

The inner part of this gas dosing tube contains a two-stage grid homogenizes the flow of gas molecules in such way that their flux is uniform within the cross-section of the square profile. This shall ensure that a uniform thickness of the adsorbate layer is made by such injection. The thickness was investigated directly on different spots of the sample by the means of electron beam scrubbing and it seems to be uniform up to the measurable precision. The temperature programmed desorption (TPD) curve does not indicate any discrepancies in terms of adsorbate thickness either.

4.10.6 Dosing system

The dosing system was commissioned by injecting nitrogen with the sample held at the temperature of 10 K. The leakage current of mass 28 was measured on the RGA to assess the efficiency of such system to condense gases onto the surface without unnecessary losses. Sticking probability is presumed to be effectively close to 1, since gas particles are injected into a closed geometry of the rectangular extension placed directly above the cold and sticky sample. The leakage flow of the gas was measured to be about 1% of the total injected quantity, when the square-shaped extension is just few millimetres above the sample. When the extension is retracted by about 1 cm, the leakage flow increases to roughly 10% of the total flow. These results were then cross-checked by integrating the TPD curve. The integral amount of desorbed gas indeed shows a clear linear correspondence to the amount of gas previously condensed onto the sample. This cross-validates the proper dosing procedure.

4.10.7 Temperature programmed desorption

Gas molecules which are injected through the dosing system are adsorbed on the cold surface of the sample. Thickness of the adsorbed layer is dependent on the quantity of injected gas and on the efficiency of the gas injection part described earlier. A technique called temperature programmed desorption (TPD), is commonly used in surface science to probe the nature of adsorbates and materials not only at cryogenic temperatures. Accessible literature provides theoretical background, such as [60]-[62] and is widely used in basic research, e.g. [63] and [64]. Other papers focus on accelerator-related applications [65]-[66], or investigate effects of surface treatments and coatings on adsorption properties [67].

The TPD technique essentially consists of a partial pressure measurement during a temperature ramp. As the temperature of the sample gradually increases with at a constant rate, thermal energy of molecules on the surface increases. Molecules with binding energy lower than a certain threshold are desorbed and enter the vacuum chamber, where they can be detected by vacuum gauges and residual gas analyser.

Analysis of a TPD curve can indicate the amount of molecules bound in various binding states. This is useful e.g. to tell apart physisorbed and chemisorbed molecules and their respective amounts, or to determine their binding energy. There are several types of desorption which take effect depending on so called "order" of desorption. The zeroth order would correspond to a condensation and first order to non-dissociative adsorption. For example, there is a difference in binding energies between molecules adsorbed on a clean metal surface and molecules condensed later onto this first layer of gas, which eventually form a multilayer coverage. This dissimilarity is an illustration of different desorption orders, that are visible in the TPD curve.

Figure 24 illustrates TPD curves for coverages from 0.5 to 1.4 monolayer (ML). Cold copper sample is heated with a precisely controlled temperature ramp of 10K/min. This rate was used systematically in all measurements, for it is a compromise between time efficiency and the height of the pressure peak, which should not damage the UHV instrumentation. Shape of the TPD curve clearly changes with coverage: a new sharp peak emerges from the background at 25 K, as coverages increase above 1 ML. It can be attributed to a change of desorption order, that is the passage from sub-monolayer to a multilayer coverage. The density of molecules in 1 ML is commonly taken to be about 10^{15} molecules/cm² for most macroscopic technical surfaces. For example, if a porous coating is applied on the surface, its microscopic surface can be enlarged by multiple orders of magnitude.

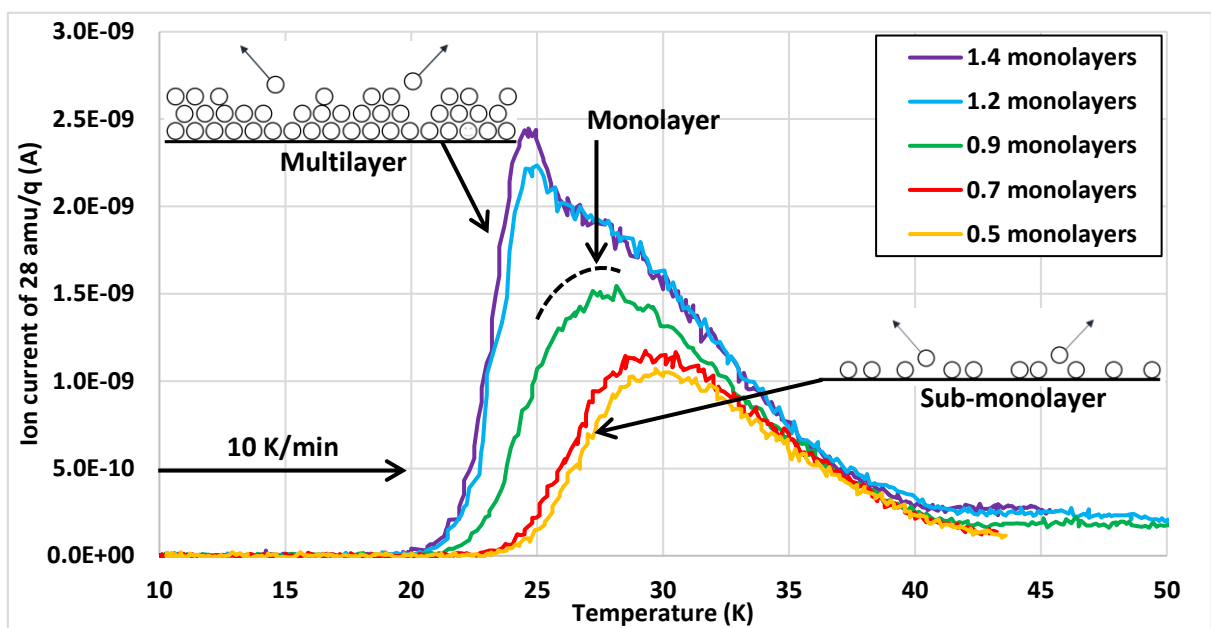


Figure 24: temperature programmed desorption curves measured in N_2 adsorbed on baked Cu surface. Rate of temperature rise is 10 K/min. Background signal was subtracted.

4.11 Bayard-Alpert vacuum gauge

A calibrated hot cathode ionization gauge of the Bayard-Alpert construction, originally presented in [68]. The currently used version upgraded with a modulator was presented by Redhead [69]. This gauge “naked” arrangement is manufactured by a SVT company. Once more, solid theoretical and practical background on partial and absolute pressure measurements is to be found e.g. in Weston [54] and Jousten [55].

The gauge consists of a sparse grid, which is positively biased and electrically attracts electrons emitted from the heated filament. The electrostatic gradient is what gives the electron its power to ionize residual gas molecules. It is an energy field created by the grid, that surrounds it, penetrates it and binds electrons’ motion to it. This

effectively extends electrons' trajectories and the longer they are, the greater the probability of ionization. The newly created ionized molecules are then attracted by the collector, which is biased negatively with respect to the grid. This creates a collector current, which is an indirect measure of the pressure within the vacuum chamber.

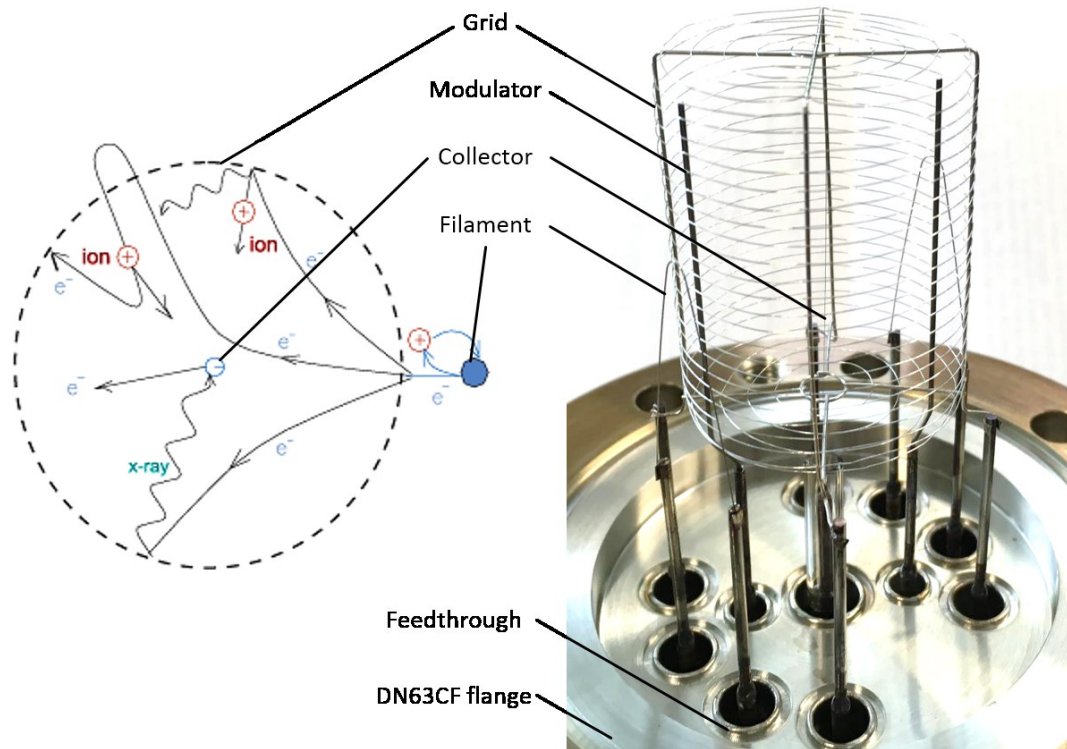


Figure 25: Detailed view of Bayard-Alpert ionization gauge. Note the fine filament in the centre.

The lower limit of the gauge and is defined by X-ray background created by electrons impinging the grid. This can be compensated using the modulator, which sets the limit to about $3 \cdot 10^{-12}$ mbar. The upper limit is $6 \cdot 10^{-4}$ mbar, but interlocking mechanism stops the emission at 10^{-6} mbar preventing the filament from burning.

Pressure measured by the ionization gauge can be expressed in terms of gauge's sensitivity and currents measured on the collector and the filament. Taking a simplistic case with a single gas specie j and a pressure high above the lower X-ray limit:

$$p_j = \frac{I_c}{I_e \cdot k_j} \quad [\text{mbar}] \quad (4.19)$$

The sensitivity S_j can be further decomposed into absolute and relative sensitivity.

$$k_j = k_{abs} \cdot k_{rel,j} \quad [A \cdot \text{mbar}^{-1}] \quad (4.20)$$

The absolute sensitivity k_{abs} is measured for pure N_2 and relates the ion current measured on the collector I_c to pressure p_j . A common value is about 30 mbar^{-1} .

The relative sensitivity $k_{rel,j}$ is a correction that reflects different ionization probability, or the ionization cross-section of a given gas specie relative to nitrogen. The following table summarizes relative sensitivities for some gases of interest, as taken for 150 eV electron energy. This reflects the fact that some gases are easier to become ionized by a passing electron. For example, a pressure measured by the gauge in nitrogen equivalent has to be multiplied about 2 times to obtain the real pressure in a baked UHV chamber dominated by H₂.

Table 3: Sensitivity of the gauge for different gases relative to nitrogen.

Gas	Relative sensitivity k_{rel} [1]
N ₂	1.00
H ₂	0.46
CO	1.05
CO ₂	1.42
H ₂ O	1.12
CH ₄	1.40
He	0.18
Ar	1.29

This vacuum gauge has been calibrated prior to delivery and is taken as a reference for all remaining measurements. There are 3 BAG gauges in the setup, each bearing its custom calibration constants, that are set into its controller and then read by the DAQ. The manufacturer claims 5 % accuracy on the full logarithmic scale and 2% repeatability. The calibration laboratory states a more conservative accuracy of 15 %. The value of this uncertainty is crucial to the measurement process, as the absolute precision of the ESD yield measurement rises and falls along with it, because the BAG is used for absolute calibration of the RGA.

4.13 Quadrupole mass spectrometer

4.13.1 Principle of operation

Mass spectrometers of various types are commonly used in vacuum science as devices for qualitative analysis of the residual gas. Hence comes the term residual gas analyser, hereafter abbreviated as RGA, for it is a widely accepted term. RGA is essentially a vacuum gauge capable of measuring partial pressures of gases at ultrahigh vacuum (very low pressures) by selectively filtering gas molecules by their mass/charge ratio. More detail on RGAs operation and construction is again in Weston [54], Jousten [55] and Yates [56].

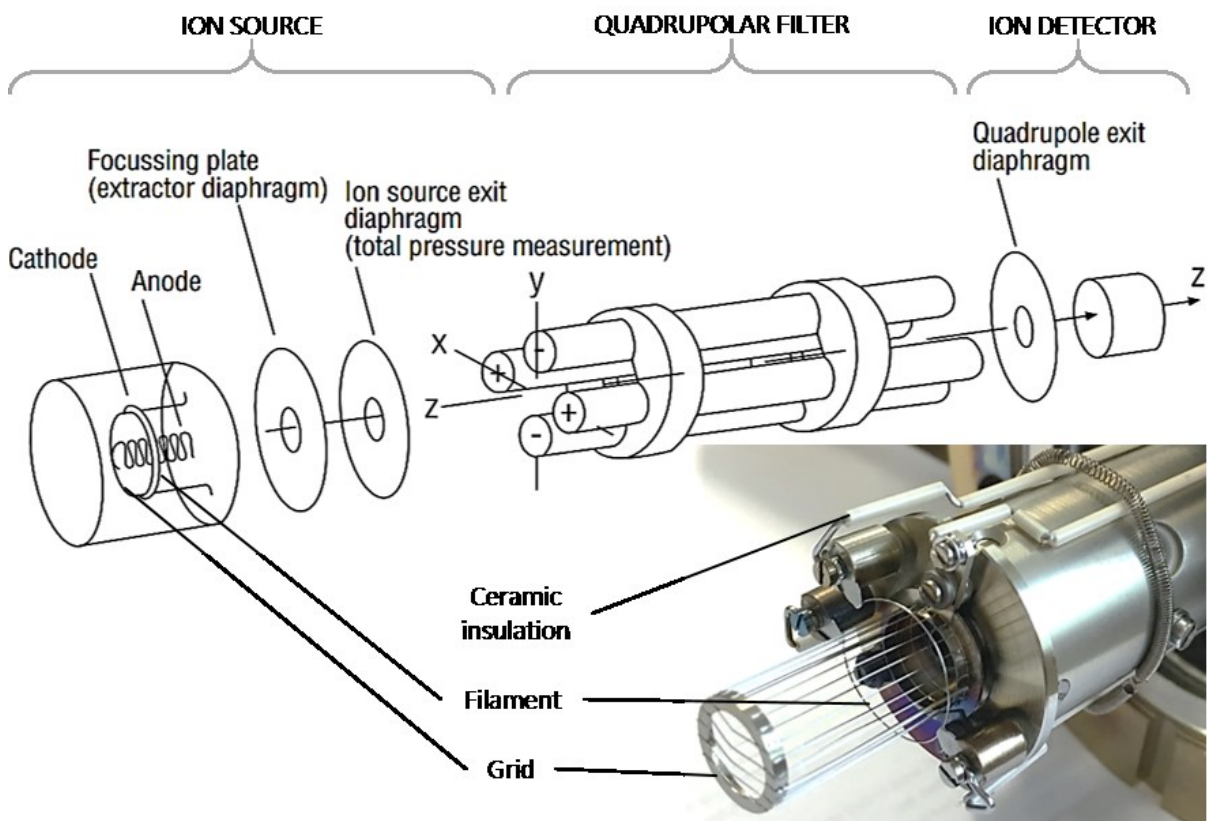


Figure 26: Scheme of quadrupole mass spectrometer in its simplest arrangement. Scheme adapted from Leybold GmbH: *Fundamentals of Vacuum Technology* [57].

The used mass spectrometer model is Pfeiffer QMG 700 and it composes of 3 main functional parts, that is ion source, quadrupolar filter and ion detector, as schematized in Figure 26. The ion source creates ionized atoms and molecules at the front end of the RGA in the very same manner as Bayard-Alpert gauge. The grid is surrounded by a heated tungsten filament, which emits electrons. The electrons travel around the positively charged grid and ionize gas molecules on the way. These negatively charged ions enter an array of hollow diaphragms, which form electrostatic optics that focus ions into a paraxial beam. This ion beam enters a quadrupole mass filter, which is constructed of 4 parallel rods. The rods are electrically insulated from the frame and each pair has a separate supply of an oscillating voltage. The two

pairs of parallel rods act as a low-pass and a high-pass filter. In parallel, they form a narrow band-pass filter, which sorts the previously ionized molecules precisely by specified mass/charge ratio. Ions can pass through this oscillating electric field only if they have a certain mass/charge ratio. All other masses have unstable trajectories that do not intercept the detector behind the filter. The oscillating voltage on the quadrupole is continuously re-adjusted by the controller, so it scans through the mass spectrum at a given rate. It can also be programmed to re-adjust in a discrete manner to follow only certain masses. This is useful in measurements further on, as the whole spectrum is not always interesting, but only following of specific masses is desirable.

4.13.2 Secondary electron multiplier characteristics

This specific RGA model is further equipped with a secondary electron multiplier (SEM), which boosts its sensitivity in the UHV region. At high pressures, the RGA operates in so called Faraday mode, that simply gathers ions that make it through the mass filter. However, the sensitivity of the Faraday cup is not sufficient in the UHV region, so the instrument is switched into a SEM mode, which amplifies the otherwise faint signal. The high voltage supply powering the SEM can be adjusted by the operator to control the amplifier gain. Figure 27 shows dependence of the ion current of chosen masses collected after the SEM as a function of the SEM voltage.

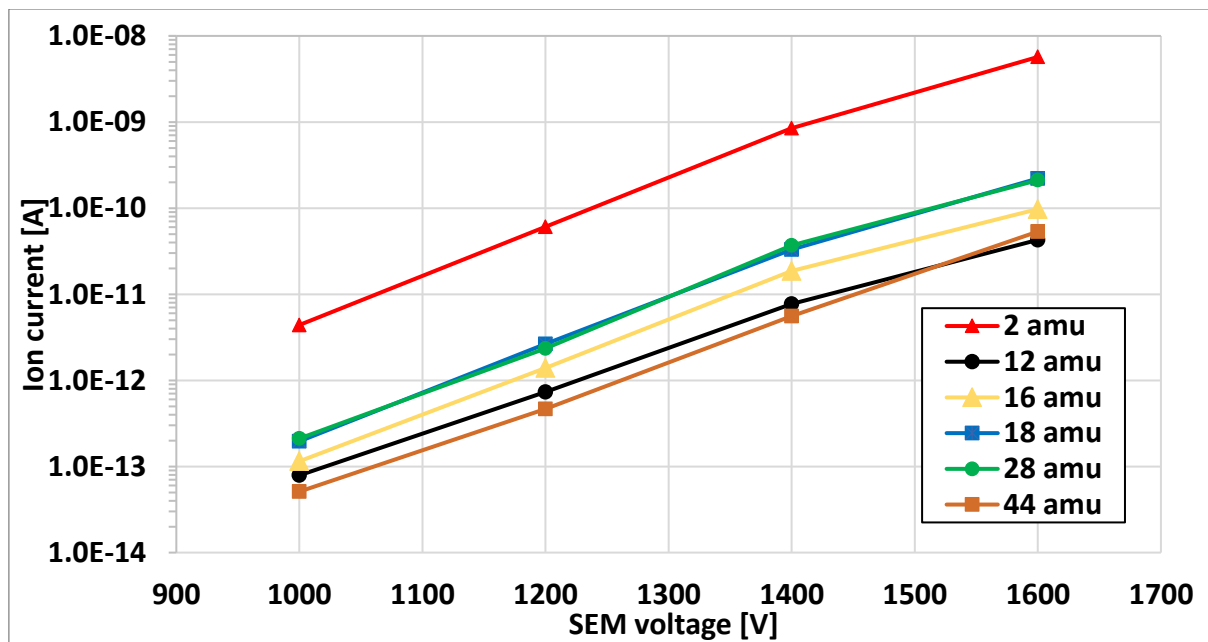


Figure 27: Sensitivity of the gauge as measured by ion current as a function of SEM voltage.

The supply voltage of 1600 V is used systematically in all measurements, as it was used during factory calibration, thus is a good reference. This voltage can be further increased, as the RGA ages and its sensitivity diminishes. This figure was measured using the background signal from the residual gas, which is dominated by H₂.

4.13.3 RGA calibration by gas injection

A series of calibration measurements were done by injecting different to assess the RGA sensitivity. Each gas was injected at different rates to measure the sensitivity as a function of pressure. Each gas injection is followed by a plateau, when a spectrum is taken. Such spectra are plotted on linear scale in Figure 28 and Figure 29 to visualize cracking patterns. The collector current collected by the SEM increases linearly with pressure, as shown for N₂ in following figure. As stated in the introductory chapter, the sensitivity coefficient k_j is determined for the major peak of each gas specie. It relates linearly the ion current ΔI_j collected and measured in the mass spectrometer to the pressure Δp_j of a gas measured by the Bayard-Alpert gauge. The pressure measured by the BAG can be assumed equal to the partial pressure, since this gas is dominant during an injection.

$$k_j = \Delta I_j / \Delta p_j \quad [A.mbar^{-1}] \quad (4.21)$$

This absolute sensitivity is similar to that of BAG ionization gauge, but applies for one mass only. The usual sensitivity for our measurements was 5 A.mbar⁻¹, but it varies slightly each time, so the RGA's absolute sensitivity measurement is done before and after each measurement series.

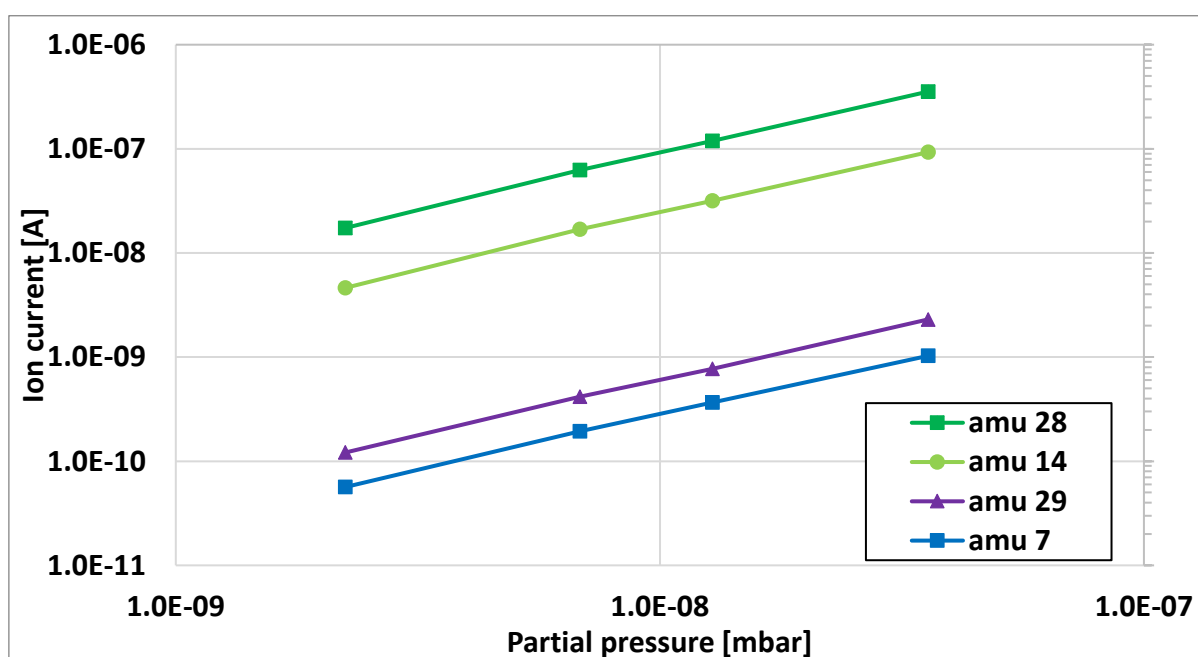


Figure 28: Ion current for various fragments of N₂ as a function of pressure. Background signal was subtracted.

Figure 28 further shows that the major peak of ²⁸N₂ at mass 28 is followed by its ions at mass 14 and 7. Molecule ²⁹N₂ formed with an isotope is also naturally present at mass 29. However, the spectrum is not always unambiguous, as different ions can have the same mass/charge ratio, so a careful analysis is required for a conclusive

idea about the gas composition. For example, simply ionized N₂ and CO both produce a major peak 28 and it is the smaller peaks that serve for identification of the gas. The blue cracking pattern of methane is more complex, as there are many more ways to ionize CH₄ molecule. If N₂ molecule is fully ionized, the cracking patterns shows a peak 14, as seen in green. On the contrary, the CO molecule in red splits into ¹⁶O and ¹²C, that is mass 16 and 12. As shown for N₂, the RGA is sensitive enough that isotopes can be observed as well, e.g. mass 29 can correspond to N₂ molecule with one ¹⁵N, or to CO molecule with either ¹³C or ¹⁷O.

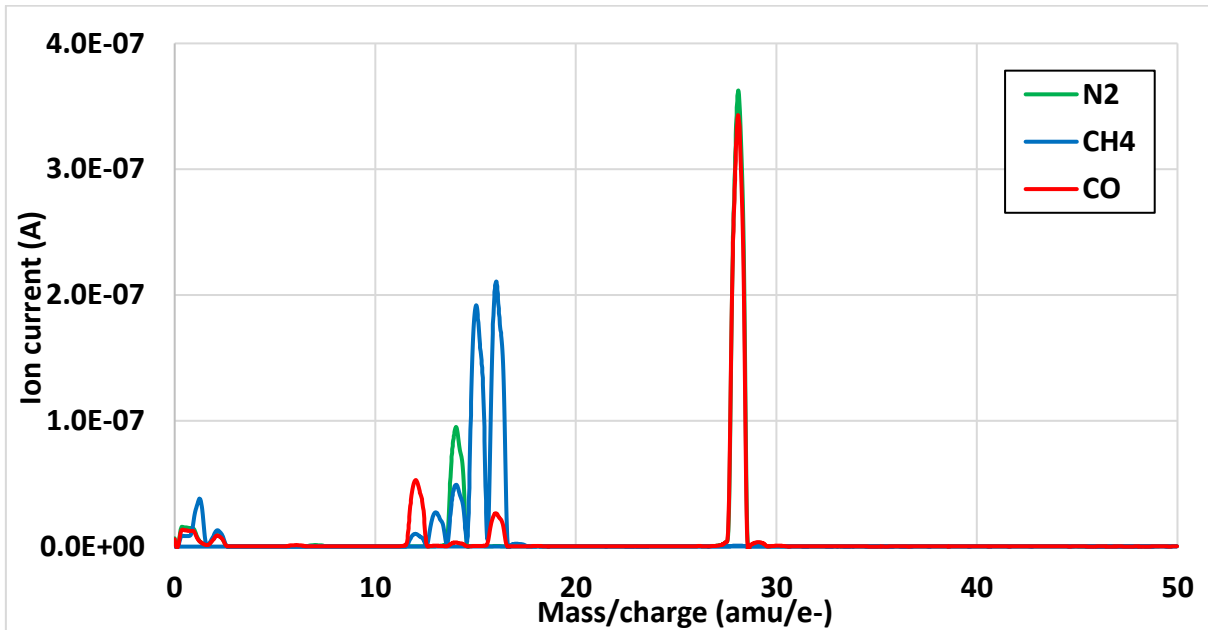


Figure 29: RGA spectra for N₂, CO and CH₄. SEM voltage is set to 1600 V.

4.13.4 Fragmentation patterns comparison to NIST database

Spectra were measured for multiple gases and cracking pattern of each gas was expressed as a fraction of their respective major peaks. This data was then compared to the NIST mass spectrometry database and the results are presented for comparison in the following Table 4. The cracking or fragmentation pattern essentially expresses the probability of creation of different fragments when a molecule is ionized.

Table 4: Measured cracking patterns referenced to NIST mass spectrum library[61].

Gas type	Ion fragment [amu/e ⁻]	Ion current [A]	Ratio to major peak [%]	NIST reference [%]
N ₂	28	3.4E-07	100.0	100.0
	14	9.4E-08	28.0	13.8
	29	2.5E-09	0.7	0.8
CO	28	3.2E-07	100.0	100.0
	16	2.6E-08	8.2	1.7
	12	4.9E-08	15.3	4.7
CO ₂	44	1.5E-07	100.0	100.0
	28	8.8E-08	57.8	9.8
	16	5.6E-08	36.9	9.6
	12	5.3E-08	35.0	8.7

CH4	16	2.1E-07	100.0	100.0
	15	1.9E-07	90.9	88.8
	14	4.9E-08	23.3	20.4
	13	2.7E-08	12.9	10.7
	12	1.0E-08	4.8	3.8
C2H6	30	2.1E-08	21.9	26.2
	29	1.9E-08	19.9	21.5
	28	9.4E-08	100.0	100.0
	27	3.5E-08	37.5	33.2
	26	2.7E-08	28.5	23.3
	15	1.1E-08	11.7	4.4
	14	8.1E-09	8.6	3.0

There is a difference in cracking patterns between our measurements and the database values. This is probably due to systematic error caused by this type of RGA. Jousten [55] suggests that the probability of ion transmission through the quadrupole filter is inversely proportional to its mass and that this transmission factor should be accounted for. This inverse proportionality on mass can be seen in equations of motion of a particle through a quadrupole. Even though, it explains some of the variability, these measured cracking patterns are likely to be taken as inherited from this particular RGA technology.

4.14 Data acquisition system

The data acquisition (DAQ) and eventually supervisory, control and data acquisition (SCADA) is running on an embedded PXI controller from NI. The PXIe-8840 is a modular platform serving a wide scope of laboratory applications.

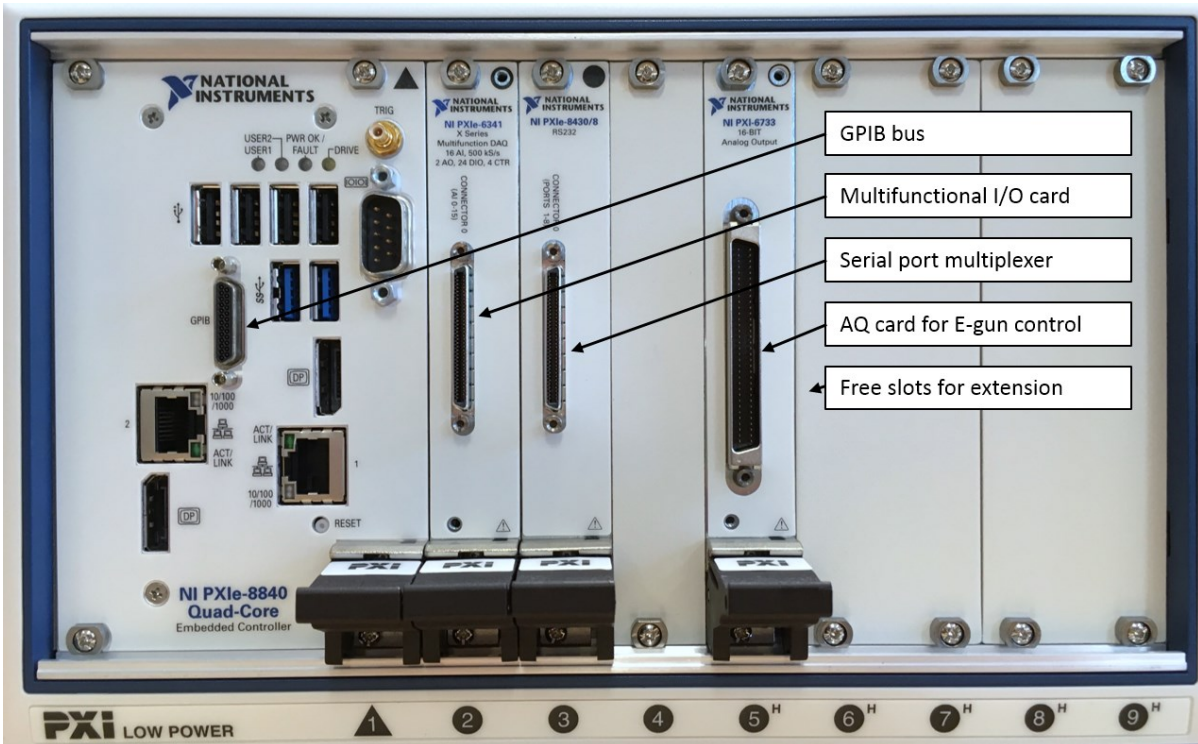


Figure 30: Modular embedded controller NI PXIe-8840 used in the SCADA system.

The PC features slots for various cards providing digital and analogue I/O, that were plugged in and configured for acquisition of data from vacuum gauges, electron gun, thermocouples, flowmeter, pressure sensors and mass spectrometer. The scheme in Figure 31 shows a simplified scheme of the SCADA system. Controllers of instruments are linked to the PXI computer by digital lines ranging from half-duplex RS-232 to ethernet connection. The instrumentation itself is usually connected by some sort of an analogue line.

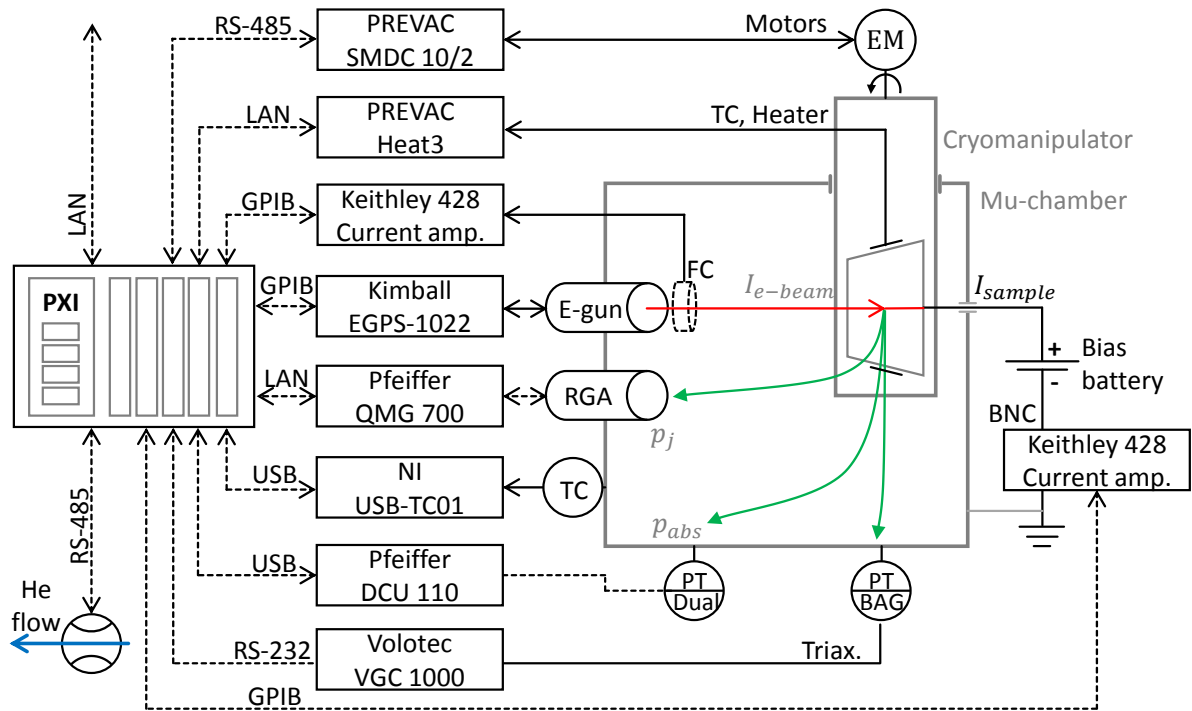


Figure 31: Scheme of the DAQ chain directly related to ESD measurements. Dashed lines are digital, full lines analogue, arrows mark the direction of communication.

The PXI runs a LabVIEW application formerly developed in the laboratory to measure some of various process values via different communication buses. Other instruments, such as the electron gun, RGA and the cryomanipulator are operated by windows applications provided by their respective manufacturers.

Components crucial to the ESD measurement are the RGA, BAG and two Keithley current amplifiers. These have gain up to 10^{11} V/A and a high signal to noise ratio and amplify the faint electrical current collected either on the biased sample or on a Faraday cup. The collected current ranges from nA to μ A, depending on the electron gun settings. The amplified output is normalized to 0÷10 V.

5 Electron gun

The source of electrons for this experiment is a high-end electron gun ELG-2 manufactured by Kimball Physics Inc. It is delivered with a high-voltage power supply EGPS-1022 and a LabView application. The manufacturer states that the gun provides an electron beam with profile that has a gaussian shape and small diameter. The gun comes mounted on an extension rod, which is fixed in a DN40CF flange multiplexer, that houses vacuum feedthroughs for high voltage electrical supply. Internal parts of the gun are not visible, as they are covered in a 0.75" housing tube for the purpose of electromagnetic shielding and mechanical protection. The whole framework is at a ground potential. Note the Faraday cup which caps the nozzle of the electron gun at the right extremity. It is electrically insulated from the frame and allows the measurement of beam current leaving the electron gun. It can be manually rotated into the closed position, or left open in an off-axis position.

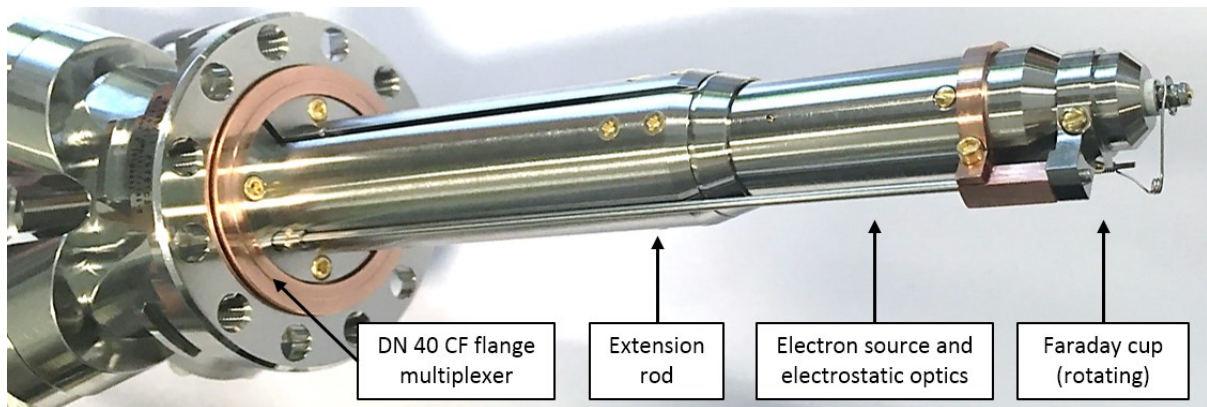


Figure 32: The electron gun before mounting into a DN40CF flange of the experimental chamber.

The following chapter aims to provide a concise summary of the main working principles to a degree that enables a proficient operation of the gun for the purposes of ESD measurements in conductive samples.

5.1 Principle of operation

The internal parts of the electron gun can be formally subdivided into 3 subassemblies according to their functionality: electron source, electrostatic optics and deflection plates. These are optionally followed by a Faraday cup, which enables precise measurement of the electron current leaving the gun. The electron source is used to control the quantity of electrons which are emitted from the gun by the means of cathode temperature and grid voltage. The electron source is followed by a series of electrostatic lenses. This electrical analogue to optical lenses shapes the beam and eventually forms an image (beam spot) of the object (cathode), if setup correctly. The gun is operated by controlling electric potentials on different parts of the gun. Figure 33 shows an electrical scheme of different components. The left side is

dedicated to controlling the electron beam current I_{BEAM} emitted by the source by varying voltage V_{ES} supplied to the cathode. The dynamics of such control is limited by the thermal inertia of the cathode, so it is followed by a grid. The grid serves for fast control of the beam current by applying an electrostatic potential V_{VG} that either partially or fully suppresses the electrons emitted from the cathode. This part can also provide a pulsing effect, if wired accordingly.

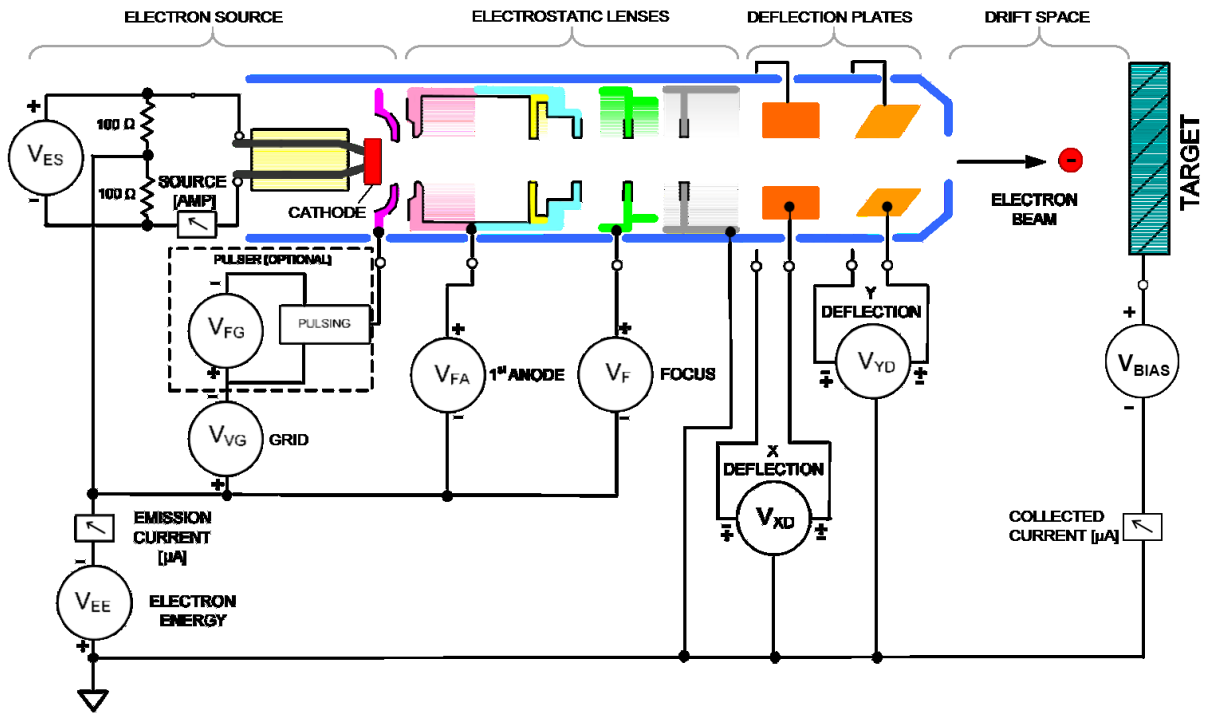


Figure 33: Electrical diagram of the electron gun. Note the main components and multitude of voltages to be controlled. Scheme adapted from device manual by Kimball Physics Inc. [71].

The electron source assembly is followed by a pair of biased apertures called 1st anode and focus and one grounded aperture. A positive electrical potential is applied to bias these apertures in such a way that the resulting potential gradient shapes the electron beam and accelerates it towards the nozzle of the gun. Up till now, all these parts are electrically floating on a potential which determines the resulting energy of electrons. Last subassembly that acts on the electron beam before it exits the gun is the deflection. They apply a potential field transverse to the particles' motion and cause them to deviate from the original axis. Two pairs of plates at equal but opposite voltages are present to deflect in 2 perpendicular directions X and Y.

5.1.1 Parameter space

This set of 7 different voltages and all their possible combinations results into a vast parameter space to operate with, as seen in the Table 5. An insight into the main principles of functioning of the gun can help to reduce this large range of parameters into a much smaller set of variables, which are more or less independent.

Some presumptions can be made for the first approach. For example, the anode and focus voltages V_{FA} and V_F are continuously dependent on the accelerating potential V_{EE} , i.e. the beam energy. The higher the energy of the beam, the more rigid it is, so higher focusing voltage is needed to shape it. As a result, these voltages have to be re-adjusted simultaneously with the electron energy. Other parts, such as deflection plates are dependent on the electron energy in a similar manner. The higher energy, the higher voltage has to be applied on deflection plates to achieve the same deflection. The beam current emitted from the source also depends on the energy, so it should be equally accounted for.

Table 5: Voltages generated by the EGPS-1022 power supply controlling the electron gun.

Parameter	Variable	Range
Accelerating potential (=Electron energy in eV)	V_{EE}	2 ÷ 2000 V
Grid voltage	V_{VG}	0 ÷ -50 V
1 st Anode voltage	V_{FA}	0 ÷ 200 V
Focus voltage	V_F	0 ÷ 2000 V
Electron source	V_{ES}	0 ÷ 3 V
Electrostatic deflection in X and Y axis	V_{XD}, V_{YD}	-150 ÷ 150 V

5.2 Electron source

This electron gun has a thermionic electron source, which emits electrons as a result of thermal motion at high temperatures. The source of electrons is formed by a cathode, which is constructed from a small Tantalum disc and a Tungsten wire placed beneath the disc. The electric current passing through the wire generates Joule heat, which in turn stimulates a thermionic emission of electrons from the disc. The temperature of the cathode determines the number of emitted thermionic electrons, i.e. the electron beam current produced by such source.

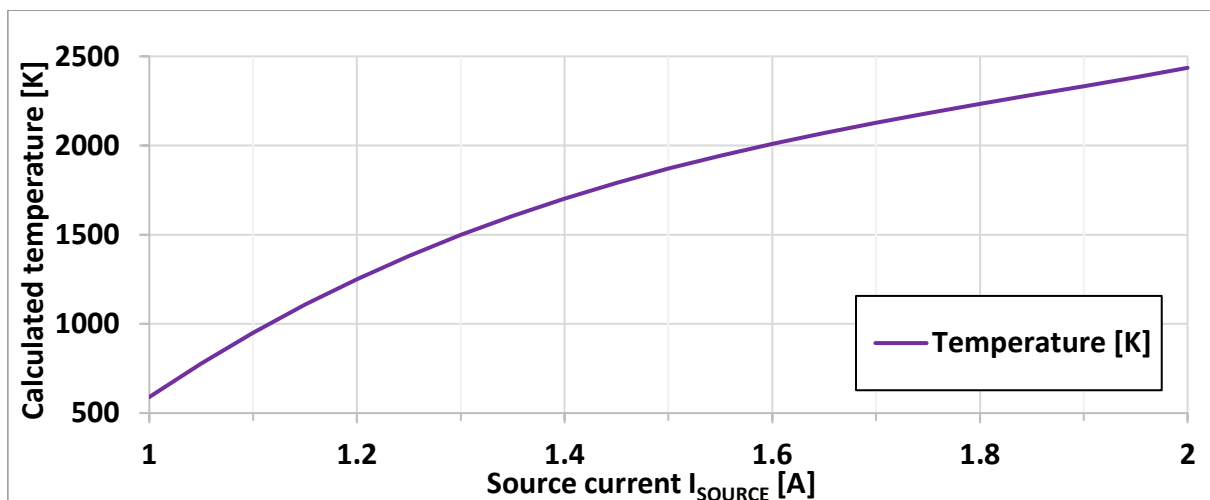


Figure 34: Cathode temperature as a function of source current passing through the filament.

The emission current leaving the cathode is strongly dependent on its temperature, as it is following the Richardson's law, and the temperature itself varies largely with source current passing through the filament. The emission current of the cathode becomes limited at high temperatures by the space-charge effect.

The Tantalum disc has a diameter of 0.84 mm and a thickness of 0.1 mm and is welded on a filament only 0.08 mm thick. Both the tantalum and tungsten have UHV compliant properties of low vapor pressure at high temperatures. The manufacturer claims the tantalum to have a melting point at 3188 K and the work function is claimed to be 4.1 eV. They calculated that the energy spread of thermionic electrons is less than 0.7 eV. The disc is welded on one spot only, which imposes a constant electrical potential over the whole disc. This allows for a direct and precise control, by simply varying the electrical current passing through the filament. The emission current is controlled in the range of $0 \div 10 \mu\text{A}$ by varying the Source current in the filament from $1 \div 2 \text{ A}$. The maximum emission current of $10 \mu\text{A}$ corresponds to the cathode temperature of about 2350 K, as plotted in Figure 34.

5.2.1 Electron beam current levelling using the grid

The next functional part of the electron source assembly is the grid. The grid enables a dynamic control over the current of electrons leaving the source and even allows a total suppression of the beam. The grid voltage V_{VG} is by default set to 0 V, which corresponds to the maximum beam current I_{BEAM} . The beam is totally suppressed at about 20 V, depending on the beam energy, as seen in Figure 35.

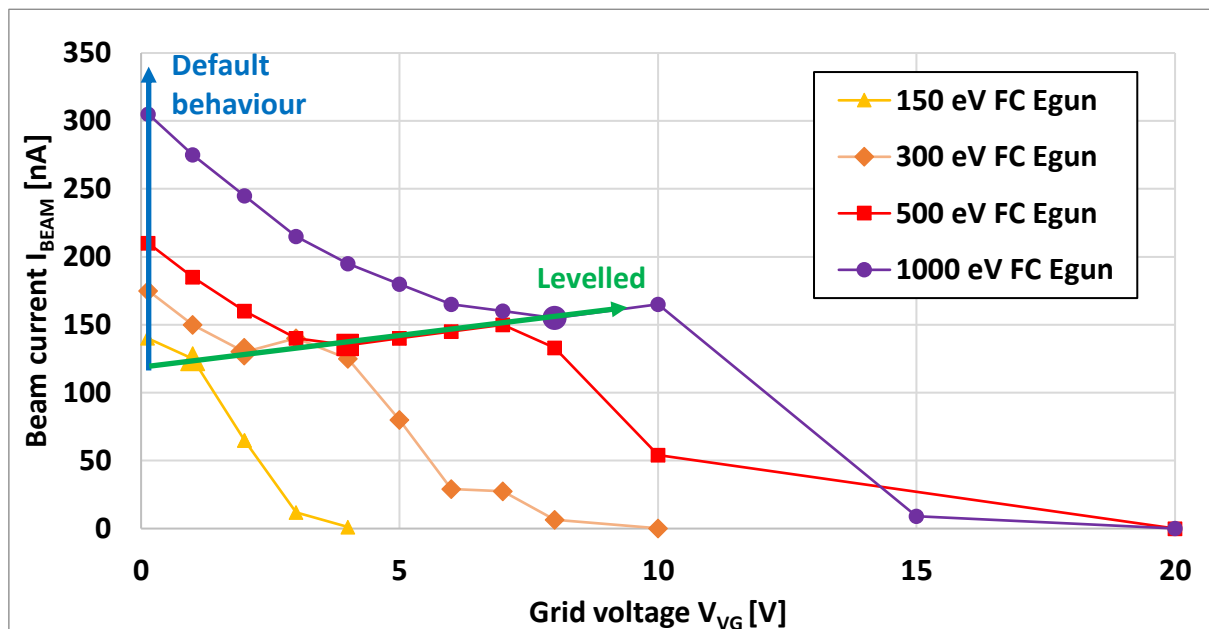


Figure 35: Beam current as a function of grid voltage for various energies. The measurement was done with autofocusing function and on Faraday cup of the electron gun biased to 48 V.

For some reason more electrons are extracted from the cathode at higher energies, so the beam current increases with the electron energy. This default behaviour was measured for $V_{VG} = 0 \text{ V}$ and constant filament temperature and it is illustrated

by the blue arrow marked “Default”. This can be compensated by using the grid thanks to the decreasing dependency of the current on the grid voltage. A green arrow marked “Levelled” connects the highlighted data-points in the characteristics. These points are used to generate a linear dependency of grid voltage needed to maintain approximately constant beam current across different energies.

Figure 36 shows that the levelling feature brought a factor of 5 improvement in the beam current stability for energies between 150 eV and 1000 eV. This improvement is desirable if measurements are to be made at a constant current density over a range of energies. This could be equally achieved by varying the source current, but such changes would take effect at much longer time scales, because of the thermal inertia of the cathode. On top of that, the cathode has a software protection built into the LabVIEW program to prevent thermal shocks, so the source current is slowly ramped up or down, when being turned on or off.

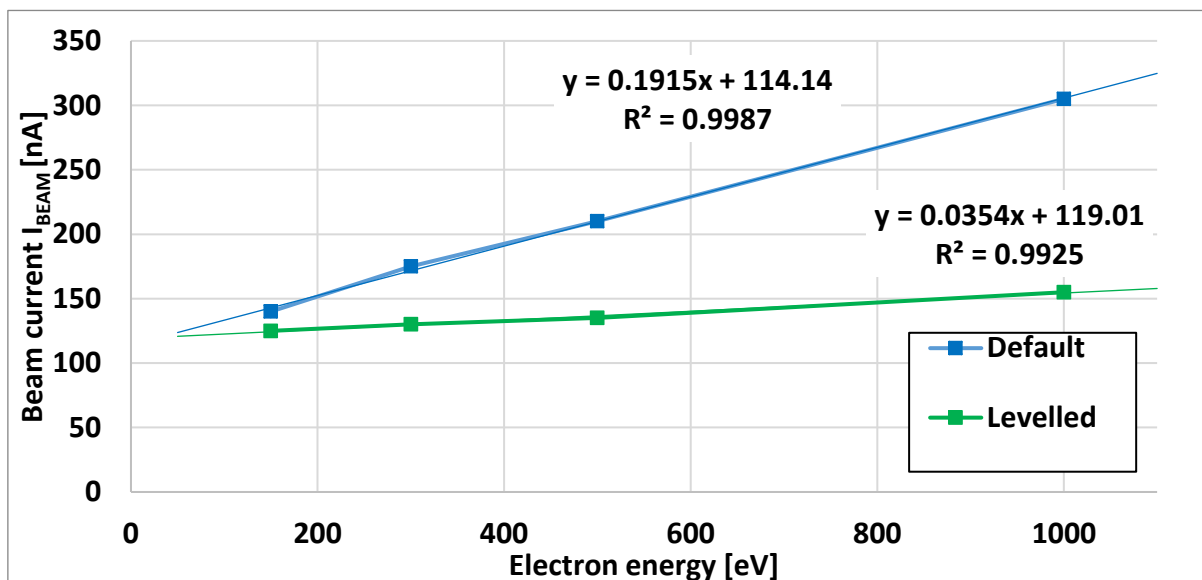


Figure 36: Beam current as a function of electron energy with and without beam current levelling. The measurement was performed with autofocusing.

5.3 Electrostatic optics

The electrons are extracted from the cathode and then enter a system of electrostatic apertures, which form Einzel lens of a sort. This optics bends the electrons in a manner very much similar to that of visible light in ray optics composed of glass lenses. A brief introduction with a good explanation of electrostatic optics is presented by Richard Feynman in his famous lecture series [73]. The topic is further developed e.g. in the works of Reiser [74], Liebl [75] and Egerton [76]. The analogy to optical lenses even includes aberrations, which are caused by various imperfections of the beam and the optics itself and will be addressed later.

An assembly of 3 hollow cylindrically symmetrical parts composes of the 1st Anode, the Focus and the ground potential form an electrostatic lens. This trio can be thought of as Einzel lens. It focuses the electron beam and then accelerates it towards the deflection plates, if tuned properly. Note that the cathode and the electrostatic optics are all floating with respect to the ground potential by the Electron energy voltage V_{EE} . Tuning of the 1st Anode relative to the Focus remains rather constant, when varying the energy by a small amount, or changes smoothly at larger energy differences. Despite being more complicated from the electrotechnical point of view, this scheme with floating electrostatic optics should be easier to maintain in focus, as compared to a layout where everything is separately referenced to the ground potential.

A series of measurements was done using the phosphor target in order to obtain a dataset with correct focus for different energies from 150 eV to 2000 eV. Voltages of anode and focus were found manually for each of the data points. The goal was to find the most focused beam spot for each energy, or the circle of least confusion, as seen from the optical point of view. The entire dataset is plotted in Figure 37 showing a continuous behaviour and a rising tendency with increasing energy. This data was then interpolated by a piecewise 4th order polynomial in order to capture the trend and implement it programmatically later.

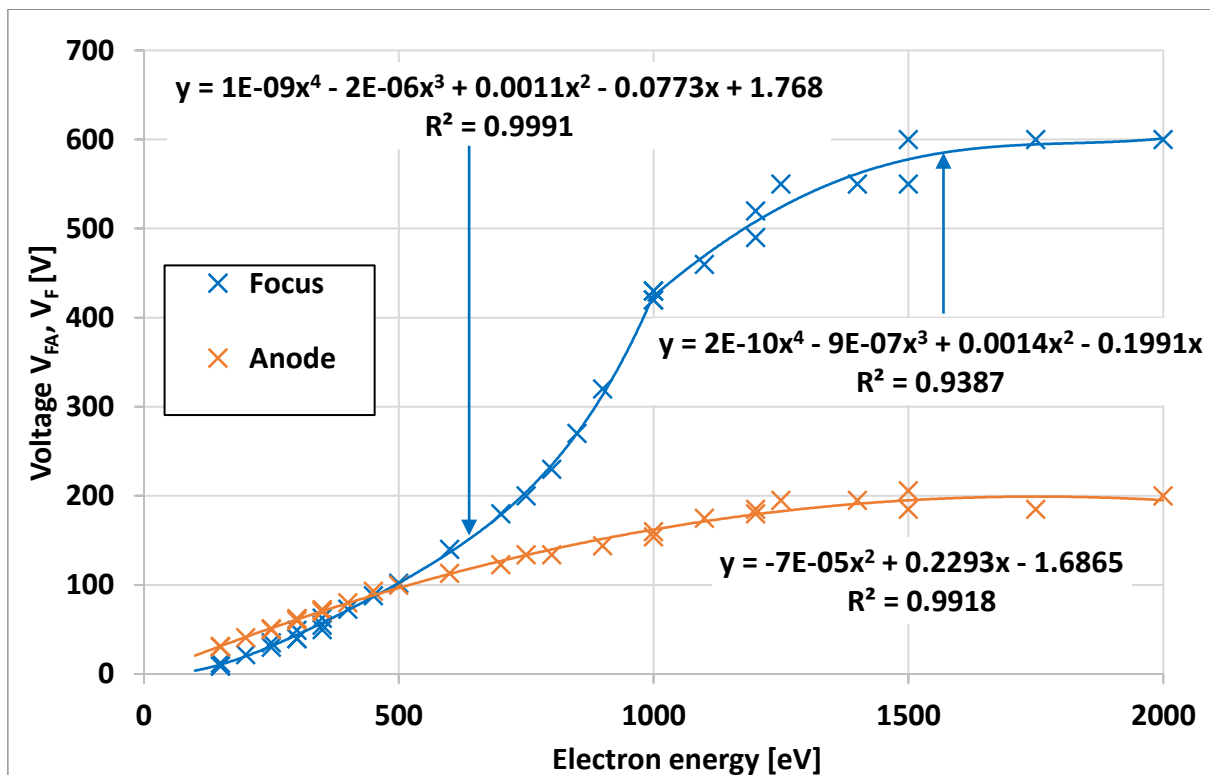


Figure 37: Energy dependence of voltages applied to electrostatic optics leading to a focused beam spot with the least size possible.

5.4 Deflection plates

The nozzle of the gun is equipped with two pairs of deflection planes tilted by 90°. Applying a voltage difference on these plates results into deviation of the electron beam in either X or Y direction. The exact angular deviation of the beam is dependent on the applied voltage, but also on the energy of electron beam. The more energetic the electrons are, the more inertia they have, causing the beam to be more rigid and resistant to the deflecting voltage. The maximum of ± 150 V can be applied on both pairs of deflection plates independently. This brings a unique opportunity to take series measurements in a form of matrix of dots positioned over the sample. The same technique could also give the option of rastering, similar to that formerly used in cathode ray tubes (CRT).

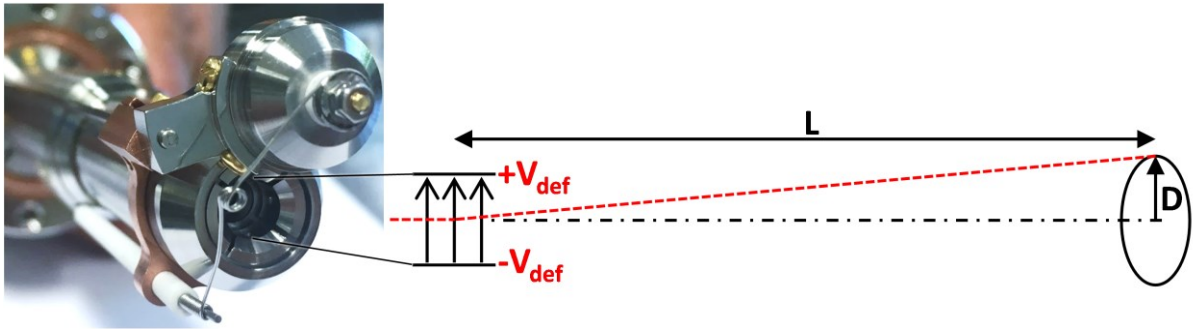


Figure 38.: Scheme of electrostatic deflection of the electron beam.

The following formula represents a first order approximation of the deflection voltage needed to bend a non-relativistic electron beam. The deflection voltage V_{def} is determined by the geometrical proportions given by the ratio D/L , which states that the longer the displacement, the higher deflection voltage is needed. Conversely, the longer the path from nozzle of the gun to the target, the smaller voltage is needed, as the beam drifts over a longer distance. Moreover, when the electron's kinetic energy E_k rises, larger deflection voltage has to be applied to achieve the same displacement.

$$V_{def} = c \cdot \frac{D}{L} \cdot E_k \quad [V] \quad (5.1)$$

It was measured experimentally at 4 different directions, that a deflection voltage of 37 V is needed for a 500 eV beam to reach a border of the phosphor sample. Another trial showed that a deflection voltage of ± 28 V is needed to bend a 400eV beam to the same extremity.

$$c = \frac{L}{D} \cdot \frac{V_{def}}{E_k} = \frac{60}{6.35} \cdot \frac{37}{500} = 0.70 \quad [V/eV] \quad (5.2)$$

$$c = \frac{L}{D} \cdot \frac{V_{def}}{E_k} = \frac{60}{6.35} \cdot \frac{28}{400} = 0.66 \quad [V/eV] \quad (5.3)$$

Evaluation of these measurements allows to calculate the proportionality coefficient c to have an average value $c = 0.68 \text{ V/eV}$. This value is used for further calculations and will be implemented in the LabVIEW program.

$$V_{def} = c \cdot \frac{D}{L} \cdot E_k = 0.68 \frac{D}{L} \cdot E_k \quad [V] \quad (5.4)$$

The resulting formula was evaluated for electron beam energies in a range from 50 eV to 2000 eV and is visualised in a log-log plot in the Figure 39 for this particular configuration of gun and sample. A deflection voltage in the range from $\pm 150 \text{ V}$ can be determined from known beam energy and desired transversal displacement D .

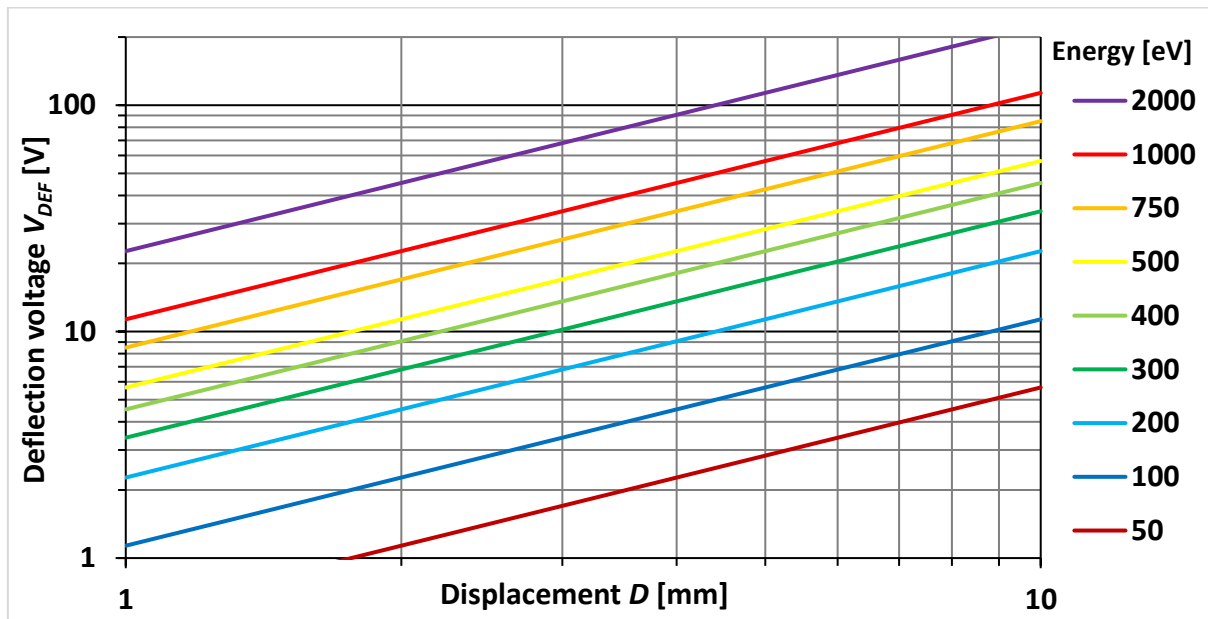


Figure 39: Linear dependence of deflection voltage vs. displacement for a range of electron energies. Values are calculated for nozzle-sample distance $L=60 \text{ mm}$.

5.5 Beam parameters

The electron beam is expected to have the Gaussian shaped profile. The shape was verified experimentally by scanning the beam in X-axis direction with two concentric Faraday cups mounted on the cryomanipulator. Current collected on each of the positively-biased Faraday cups is a direct measure of the number of incoming electrons.

Figure 40 depicts results of such measurement performed with a 300 eV beam impinging on Faraday cups, which are positively biased to $V_{BI}=47.8 \text{ V}$. Starting to move the Faraday cup from the left side, the outer FC collects the most of electron beam current. As the manipulator scans from the left at the rate of 0.1 mm.s^{-1} , the Gaussian peak strikes the inner Faraday cup and consequently decreases the current on the outer one. The situation repeats, as the beam advances to the right, creating a symmetrical image around the vertical axis of the two concentric Faraday cups.

This measurement enables us to conclude that the cross-section of the beam is symmetrical and has a Gaussian profile. To quantify the result of this measurement, the full-width at half-maximum (FWHM) is about 1.2 mm. The same test was performed in the Z-axis direction, which is perpendicular to X-axis and produced a similar result.

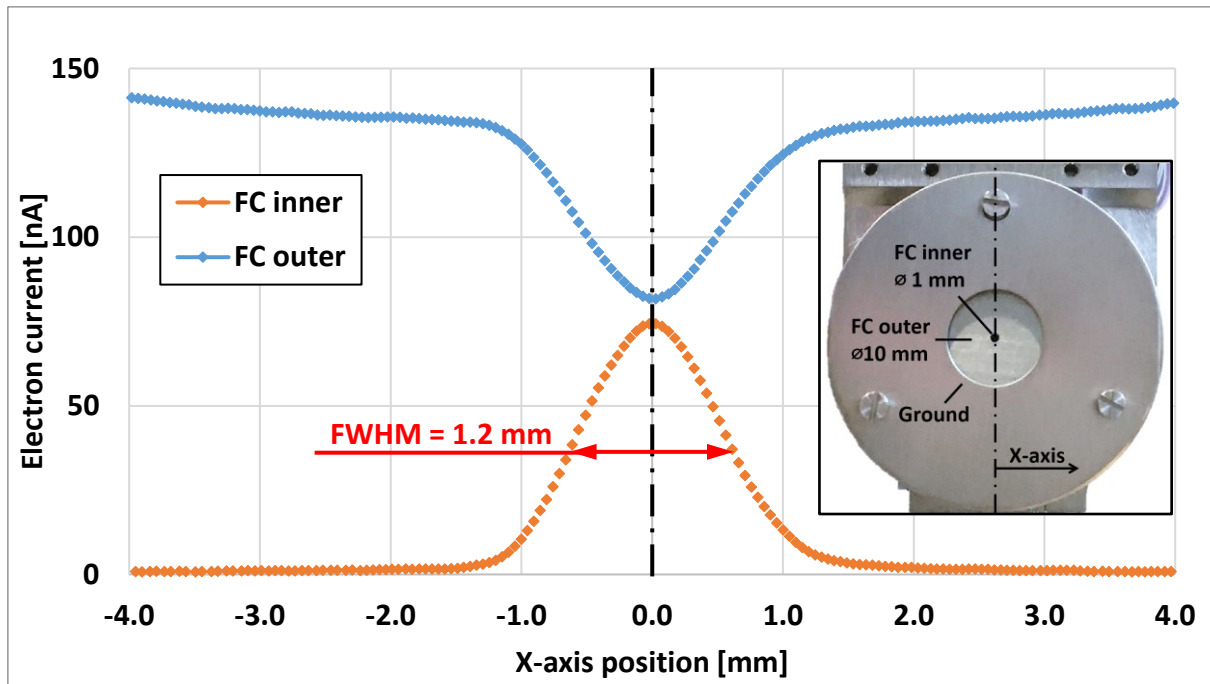


Figure 40: Electron current measured during scanning of the electron beam by two concentric Faraday cups (FC) mounted on the manipulator. The signal is smoothed over 2s period and only ever 4th data-point is displayed for clarity.

The manufacturer states, that the calculated thermal spread of the electron source cathode is as low as 0.7 eV. This value is theoretical and in practice is likely to increase as the electrons propagate downstream of the gun through the extraction grid and electrostatic optics.

For example, Sise et al. [72] simulate various aberrations for the electrostatic optics, which are similar to those commonly observed in optical lenses. These aberrations have been visually observed during operation of the electron, while gun shooting on a phosphor sample. The circle of confusion was observed during the focusing process in a range of energies and the coma effect was only profound when deflecting the beam at energies lower than about 1 keV. The chromatic aberration probably could have been used to estimate the energy spread of the electron beam, but it was not distinguishable behind the other aberrations. Thus, no clear conclusion about the energy spread could be made and the value of 0.7 eV provided by the manufacturer is to be trusted.

5.5.1 Current on Faraday cup vs. bias

The electron beam current can be measured using a faraday cup, which is an electrically insulated target. This electrically floating target faces the electron gun and can be biased to different voltages in the positive and negative sense with respect to the ground. When biased negatively, it repels electrons away, including all secondary electrons which are excited by the impinging beam. Conversely, electrons are attracted when the target is biased positively. This includes all secondary electrons which do not have kinetic energy large enough to escape the potential well given by the bias. Common dividing value between true secondary and backscattered electrons presented in the literature is 50 eV with a peak under 20 eV. It is safe to say that majority of secondary electrons is attracted back to the surface of the target for a bias of 48 V. More details about effects concerning electrons-material interaction are well covered in the article of Suga et al [51] and in the work of Reimer [77], both focusing on the field of scanning electron microscopy.

These underlying phenomena project themselves on the curve of the beam current visible in Figure 41, which saturates around 20 eV. In other words, the most part of secondary electrons have energy below 20 eV and as a result are attracted back to the biased surface even for small bias voltages.

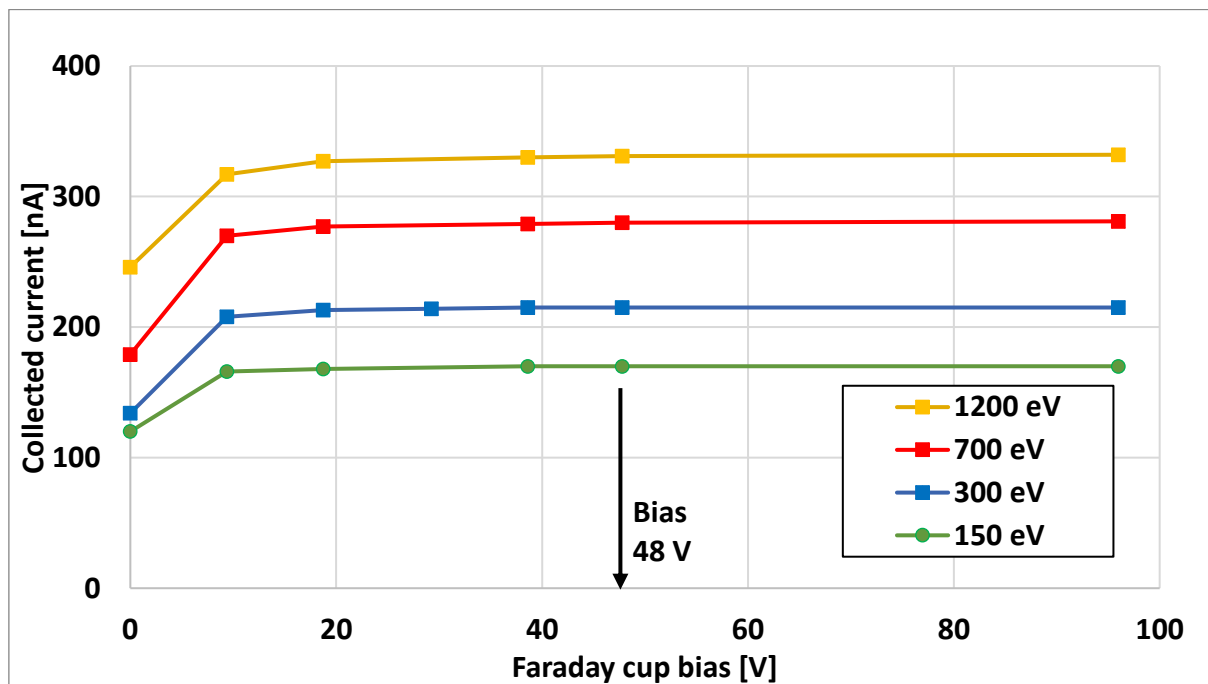


Figure 41: Collected current on a Faraday cup as a function of voltage bias of the gun. Measurement for various energies with autofocusing, without current levelling.

The current collected on the target in the range of nA, which is very small for regular DAQ devices, which usually read voltages in the normalized range of ± 10 V. Thus, it is amplified in a Keithley current amplifier to a normalized range of $0 \div 10$ V. The gain of the current amplifier was adjusted during each measurement and usually was in the range of $10^7 \div 10^{10}$ V/A.

5.6 LabVIEW control

Former measurements of various characteristics of the electron gun will now be transferred to practice and implemented into a LabVIEW application in an easy to use manner. The manufacturer provided an application capable of controlling the electron gun and giving it a rather basic functionality. The application provides a low-level communication with the power supply, reads the actual values of different parameters and offers non-feedback control of voltages. It also offers some advanced features such as pulsing option, data-logging and user-tracking, but the development of more advanced functions are up to the end-customer. This is because the deployment varies with each installation in the wide range of different applications. So, there was a need for in-situ development of advanced control functions, such as focusing of the beam automatically to form spot a certain distance, deflecting the beam, or totally suppressing the beam when it is not needed. An extra feature was developed to level the beam current, so it does not change with electron energy, as it naturally would. All these features are appreciated in order to facilitate performing of scientific tasks in a precise, efficient and repeatable manner. These features can still be disabled at any time and a full control of the gun can be transferred back to an operator. Figure 42 shows the front panel before and after modifications.

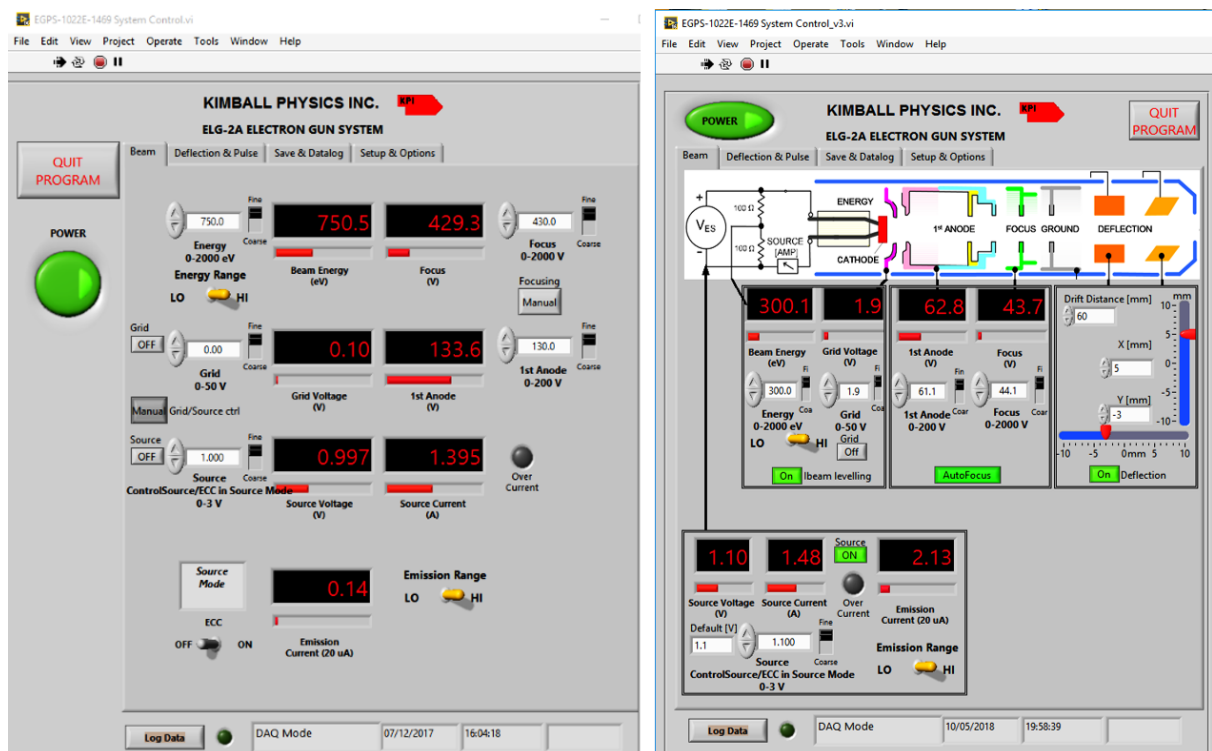


Figure 42: Front panel of LabVIEW GUI supplied by the manufacturer [71] on the left. On the right is the upgraded front panel for this application with automatic features.

5.6.1 Implementation of additional functions

The application supplied by the manufacturer is programmed using a state machine layout. It was modified in a non-invasive manner to avoid problems with functionality. The graphical user interface was enriched with a scheme of the gun inner workings, which was added for better visualisation. All numerical controls remained untouched, but were repositioned and grouped to complement the scheme of the gun. Boolean switches were added to turn all features ON and OFF.

Figure 43 shows a block diagram corresponding to the front panel above. Three case structures were added corresponding to the three main parts of the gun, the electron source, electrostatic optics and deflection. Variable pointers are used to refer to variables and to change their values during the course of each loop.

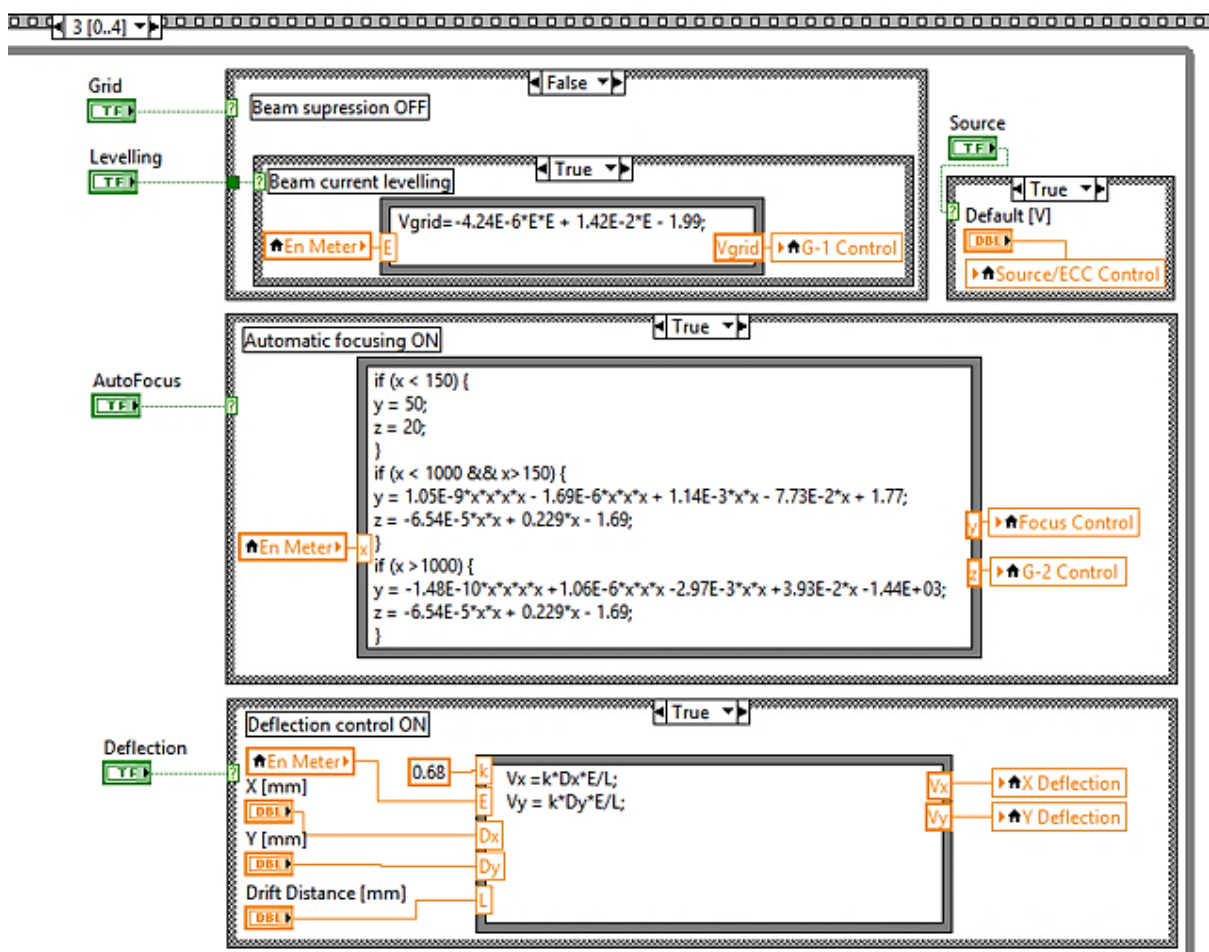


Figure 43: Block diagram of the LabVIEW GUI of the implemented functions. Note the three distinct parts controlling the electron source, optics and deflection.

The small frame on the top right of the image controls the electron source. It takes values from the boolean switch marked “Source” in the front panel and uses it to switch the case structure. The button “Source” turns ON and OFF powering of the filament itself, using the True and False cases. The True case of the adjacent

case structure sets a user-defined “Default” value using a variable reference pointing to the “Source/ECC Control”. The False case sets this value to zero. Another nested case structure in the top left part switches the Grid ON and OFF in the manner. If the “Grid” switch is False it sets a zero value to the “G-1 Control” local variable pointer and if it is True, it sets a voltage $V_{VG} = 50$ V to totally suppress the beam. The inner case structure controls the beam current levelling feature and works only if set True by the “Levelling” switch. In this case, it takes an actual value of electron energy and uses it to calculate grid voltage V_{VG} needed to level the beam current, according to the following equation, which was regressed in Figure 35.

$$V_{VG} = -4.24 \cdot 10^{-6} \cdot E_k^2 + 1.42 \cdot 10^{-2} \cdot E_k - 1.99 \quad [V, eV] \quad (5.5)$$

The case structure in the middle takes care of automatic focusing, if the “AutoFocus” switch is in True state. It reads the latest value of electron energy using a variable pointer “En Meter”. It evaluates the appropriate setting of the voltages V_{FA} and V_F in the Formula node and writes the output to the corresponding variables “Focus Control” and “G-2 Control”. The reading of the latest electron energy ensures that the beam remains in focus even when the energy is changing dynamically or oscillating. The following table summarizes equations that were used for calculations regarding the electrostatic optics. Their values are set constant in the low energy range under 150 eV. Polynomial of the 4th order is used in the mid-energy region under 1000 eV and a different polynomial for energies higher than 1000 eV.

Table 6: Polynomials regressed for different energy ranges that are used for autofocusing.

Energy range [eV]	Polynomial regression for focusing voltages as a function of energy [V, eV]
< 150	$V_F = 50$ $V_{FA} = 20$
150 ÷ 1000	$V_F = 1.05 \cdot 10^{-9} \cdot E^4 - 1.69 \cdot 10^{-6} \cdot E^3 + 1.14 \cdot 10^{-3} \cdot E^2 - 7.73 \cdot 10^{-2} \cdot E + 1.77$ $V_{FA} = -6.54 \cdot 10^{-5} \cdot E^2 + 0.229 \cdot E - 1.69$
> 1000	$V_F = -1.48 \cdot 10^{-10} \cdot E^4 + 1.06 \cdot 10^{-6} \cdot E^3 - 2.97 \cdot 10^{-3} \cdot E^2 + 3.93 \cdot E - 1.44 \cdot 10^3$ $V_{FA} = -6.54 \cdot 10^{-5} \cdot E^2 + 0.229 \cdot E - 1.69$

The last case structure nests a formula node which calculates deflection voltages for a given energy. If the “Deflection” switch is ON in the front panel, the frame executes and proceeds with its inner commands. It first reads desired values of X and Y displacement and calculates a correct voltage setting for a given electron energy and “Drift distance” between the gun and the sample.

5.7 Verification of functionality

The autofocusing feature was verified visually using a high-definition long focal length industrial camera pointed at a fluorescent target through a viewport mounted on the vacuum chamber. The fluorescent target is formed by a substrate coated with Ag-doped ZnS. It responds with a blue glow, when subjected to an energetic beam. Figure 44 shows its reaction to electron beam of different energies using autofocus.

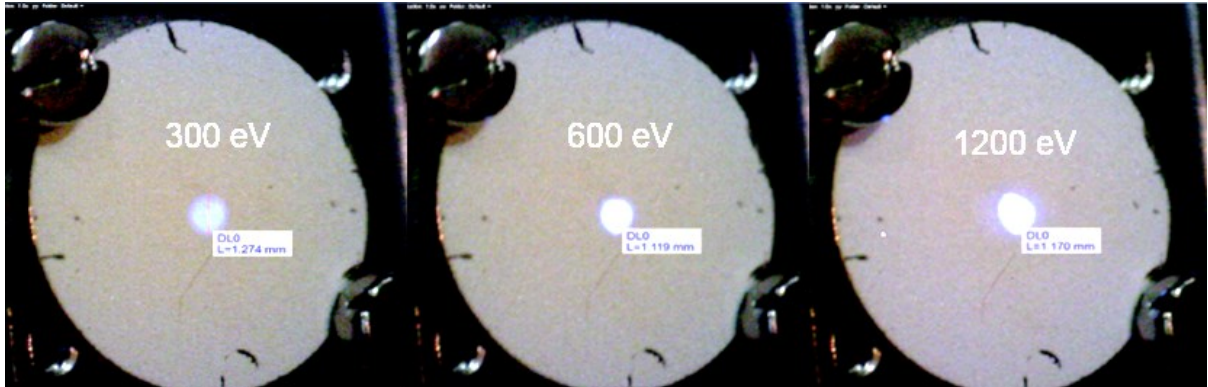


Figure 44: Visual verification of electron gun automatic focusing across different energies.

The difference in luminosity can be at least partially assigned to different beam current for each energy, which increases with energy. The beam remains well focused across energies ranging from 100 eV to about 1500 eV. The circle of least confusion is as low as 1.2 mm as measured by the camera and corresponds to former measurements done with Faraday cups. The beam spot is no longer visible by naked eye or camera for energies lower than 100 eV. Energies higher than 1500 eV were not possible to focus into such a small spot. High energies also suffer from large halo, which could be suppressed using the grid.

A thorough characterization of the source of electrons for this experiment was done. Measured dataset was regressed by a set of polynomial characteristics generalizing the results. These characteristics were used to automate the functioning of the gun in a range of energies between 100 eV and 2 keV. The automation was done by modifying a LabVIEW application supplied by the manufacturer. A set of features, such as autofocusing, current levelling and deflection were implemented in order to facilitate its control for the operator. This automation was verified by series of measurements and observations, e.g. using a phosphorescent target. Finally, it was proven operational by the first dataset acquisition.

6 Commissioning measurements

Commissioning measurements were performed as all partial components have been characterised and tuned for nominal operation. The served mainly to find weaknesses and possibly implement fixes and improvements to fine-tune the setup. Larger datasets can be systematically measured once the setup is consolidated and produces crisp and coherent data.

6.1 Preliminary measurements at cryogenic temperature

Some of the first dataset was acquired with a 200 ML thick N₂ condensate on a cold copper surface. A photo of the setup during measurements can be seen in the Appendix C. The cryomanipulator holding the copper sample was first cooled by liquid Helium from the Dewar to 10 K and gas injection through the conductance was performed to measure the pumping speed and RGA sensitivity for this run. The sample was held at 10 K while the rectangular gas dosing tube was positioned closely above it and injected gas on its previously baked surface, as visible in Figure 23. The injection was stopped when the amount of gas corresponded to the desired coverage of 200 ML of N₂. The cryomanipulator was then moved from the gas dosing position to face the electron gun nozzle, as it is visible in Figure 8.

Width of the electron beam at FWHM was optimised to about 1.5 mm across all energies, so the sample was repositioned by 3 mm in between each energy in order to expose intact pristine ice to the electron beam. Electron bombardment at energies ranging from 50 eV to 2000 eV was performed systematically and resulted into 1 curve in Figure 45, which is marked by blue dots. Each data-point consisted of electron bombardment lasting for couple minutes which enabled to reach quasi-stationary conditions in the chamber for readout of pressure and current. It was calculated that the rate of molecules' removal from the condensate is by far no capable of depleting the 200 ML coverage in such short time-scale. However, some form of the ESD yield conditioning was indeed observed with increasing electron dose.

As one set of data-points was measured, the cryomanipulator cold end was heated to 90 K at a temperature ramp of 10 K/min in order to desorb the N₂. The resulting TPD curve served as a cross-validation of proper injection procedure, reproducing the amount of gas equivalent to 200 ML previously condensed on 1 cm² surface of the copper sample.

The manipulator then repositioned the sample to face the gas dosing tube and the very same measurement process was performed with the bare difference of the copper sample temperature during condensation. It was heated up and maintained at to 14 K, 18 K and 22 K respectively. In the end, the N₂ ice was condensed repeatedly at 4 different temperatures and the ESD yield was measured forming 4 distinct curves. The temperature of the sample during electron

bombardment was systematically at 10 K. Another N₂ injection was done at the end of the measurement run for cross-checking the RGA sensitivity and pumping speed.

6.2 Data evaluation

Taking the Equation 2.5 and rewriting it into a form used for actual evaluation of the ESD yield:

$$\eta_e = \frac{\dot{Q}_j}{k_B \cdot T} \cdot \frac{q_e}{I_e} \quad \left[\frac{\text{Pa} \cdot \text{m}^3 \cdot \text{s}^{-1} \cdot \text{C}^{-1}}{\text{J} \cdot \text{K}^{-1} \cdot \text{K} \cdot \text{A}^{-1}} = 1 \right] \quad (6.1)$$

The gas flow \dot{Q}_j is expressed using the pumping speed S_j and the pressure rise Δp_j :

$$\eta_e = \frac{S_j \cdot \Delta p_j}{k_B \cdot T} \cdot \frac{I_e}{q_e} \quad [1] \quad (6.2)$$

And the pressure rise Δp_j is expressed in terms of the RGA current ΔI_j and its absolute sensitivity k_j . Temperature T is measured directly by a thermocouple. Boltzmann constant k_B as well as the elementary charge q_e are given. All values are taken for a given gas specie j . The pumping speed S_j and RGA absolute sensitivity k_j are measured for the before each run of measurements to have the most precise value possible. Nitrogen shall be used in the first round of measurements for its relatively simple and well-documented behaviour.

$$\eta_e = \frac{S_j \cdot \Delta I_j}{k_j \cdot T} \cdot \frac{I_e}{q_e} \quad [1] \quad (6.3)$$

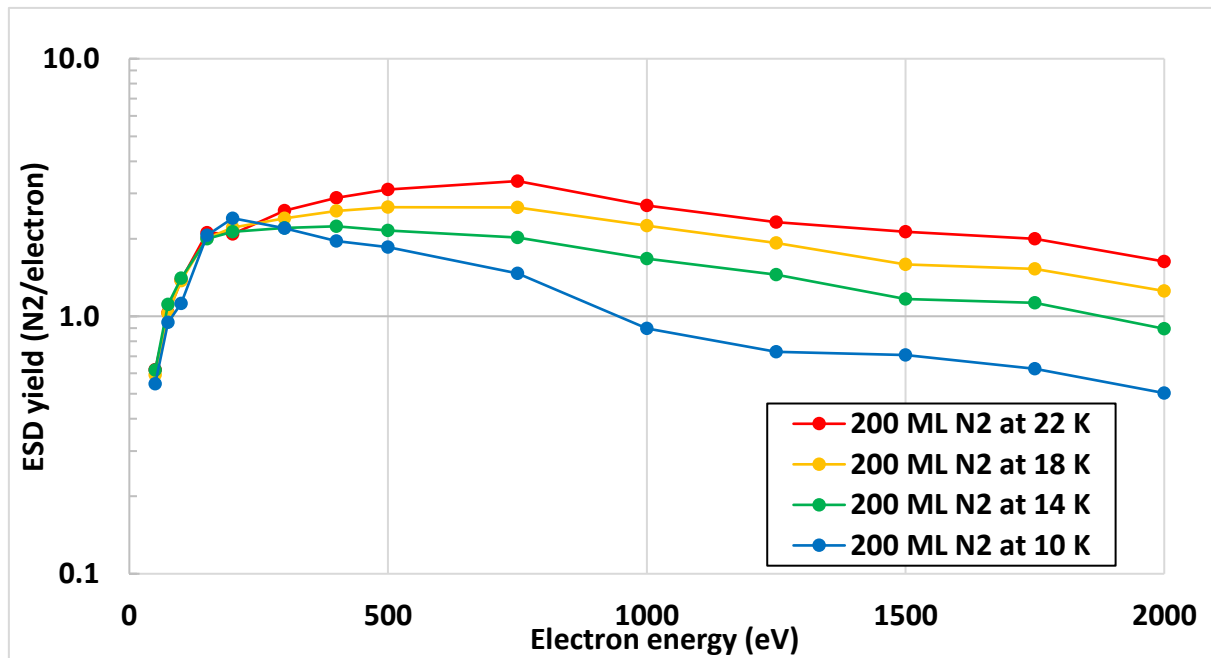


Figure 45: Electron stimulated desorption yield of N₂ as a function of electron energy measured at 10 K on 200 ML coverage of N₂ condensed on Cu substrate at different temperatures. The data was acquired and evaluated in collaboration with R. Dupuy, UPMC, Paris.

The first dataset is well coherent within itself and is in a good agreement with the literature values reviewed at the beginning. The research of Tratnik [28], [29] which was done in a similar experimental arrangement gave about $1\div 3$ N_2/e^- for similar conditions of coverage and energy. The same yield of about 3 N_2/e^- was also presented by Ellegard [34], but was measured by entirely different technique using a microbalance.

Another proof of quality comes from the shape of the ESD curve. It rises rapidly for energies under 200 eV, as the electron beam becomes more energetic, thus desorbs more molecules. This is somewhat counterbalanced at energies higher than 750 eV as the beam depletes its energy deeper in the N_2 condensate. This means that gas molecules close to the surface, where desorption takes place, gain less energy, thus desorb less.

This agreement of results is particularly outstanding when realizing the complexity of the measurement scheme and the logarithmic scale of the studied effects ranging over many orders of magnitude.

Some effect coming from the different temperature of condensation can also be observed. If all systematic errors are eliminated, conclusions can be made e.g. about the effect of condensation temperature on the morphology of the condensate.

6.2.1 Phosphorescence in N_2

Phosphorescence was observed as a by-product of ESD measurements being taken on a 150 ML thick N_2 condensed at 10 K on a Cu sample. A green glow was visible by naked eye while bombarding the sample with electrons with energies from around 300 eV and it was gradually becoming brighter as energy reached the maximum of 2000 eV. The green phosphorescence remained for couple seconds after irradiation. The energy maximum also corresponds to the maximum of beam current produced by the gun, so it is unclear, whether it was the energy or the amount of electrons increasing the apparent brightness. This effect was first observed as early as 1935, when described by Vegard [78].

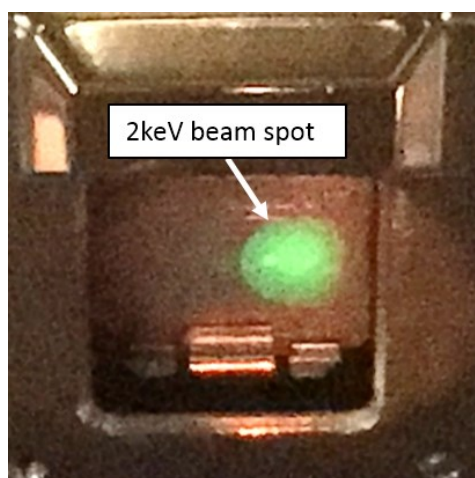


Figure 46: Phosphorescence visible in 150 ML of N_2 on Cu sample.

7 Summary and conclusions

7.1 Findings of the theoretical part

An extensive literature research was done throughout commonly accessible resources in order to support the commissioning process and to compare experimental observations with the theory and other experiments. The research showed that, except for some isolated cases, the literature lacks systematic ESD measurements in the desired range of conditions, especially at cryogenic temperatures. Hence, there is a knowledge gap to be filled by this newly assembled setup in the field of electron stimulated desorption measurements and possibly others as well.

7.2 Results of the commissioning

In the first phase, new measurement setup was assembled from hi-end components for the purpose of research in vacuum science. The installation of components, out of which many were custom-made, was followed by thorough characterisation and calibration.

A 4-axis cryogenic manipulator was seated on top of the mu-metal vacuum chamber and put into operation. Different working schemes were tried on the open-cycle liquid Helium cryogenic cooling in order to tune its performance. The consumption and cool-down time to 10 K was optimized to such an extent, that at the end of the process, a week worth of measurements could be performed with one 110 litres LHe Dewar container. The absolute accuracy and repeatability of micro-positioning was measured to be in μm range with engaged anti-backlash mechanism, which is better than needed for the foreseen measurement. Regulation of the sample temperature and its ramp-up function was also verified to be sufficient.

Assembled vacuum components were equipped with bakeout heaters and thermocouples for regulation. The bakeout procedure was performed using a programmable PLC-controlled power supply with customized temperature profiles. This resulted into an ultra-high vacuum in the 10^{-11} mbar range with H_2 dominating the residual gas. Helium leak-testing method proved the leak-tightness of the vacuum setup up to 10^{-10} mbar.l.s⁻¹ leak rate. UHV in the main chamber is supposed to remain intact when a material sample is inserted through a 2-stage Load-lock, so an electro-pneumatic interlocking mechanism was implemented. This prevents accidental venting or degradation of the UHV, if misused by an operator.

Once in the UHV range, instruments such as the Pfeiffer QGM 700 residual gas analyser and Kimball ELG-2 electron gun were put into operation and their characteristics were explored. These measurements were evaluated, generalized and used for optimization of instruments' functionality. The electron gun was automated in energy range of 100 ÷ 2000 eV by modification of the LabVIEW program provided by the manufacturer. Now the operator can use the gun at different energies

with levelled beam current, as well as deflect the beam, without having to set parameters manually for each energy. An industrial camera was installed in front a viewport, which faces the sample and provides an easy visual reference, that even enables a certain degree of a remote control of the experiment.

Gas injection manifold was attached to introduce gases from a known volume and conductance into the vacuum chamber. This served for measurements of pumping speed and RGA sensitivity under different conditions. Retractable gas dosing was installed to condense layers of gases directly onto the cold sample. This is done at precisely controlled conditions of pressure, temperature, quantity and composition. Temperature programmed desorption method was employed to analyse and cross-validate the accuracy of gas injection procedure. The Bayard-Alpert vacuum gauge was used as absolute reference for RGA sensitivity calibration at different pressures and different accelerating potentials on its secondary electron multiplier. The mass spectrometer was used to measure fragmentation patterns in gases, such as N_2 , CO, CO_2 , CH_4 and C_2H_6 . These patterns were compared to the NIST mass spectral database.

As a result, all instruments incorporated into the setup performed nominally and reproducibly. Technical difficulties that arose in the process were quickly solved, which accelerated the whole project into its second phase. This led to a fast acquisition of a crisp preliminary dataset, whose detailed analysis is underway.

7.3 Summary of the experimental results

The commissioning was succeeded by preliminary dataset measurement in N_2 and later in CO condensates created at various temperatures and coverages. A sample of first results is presented for a 200 monolayer coverage of N_2 condensed on a Copper sample at temperatures from 10 K to 22 K, while taking 10^{15} molecules.cm⁻² as one monolayer. The yield of electron stimulated desorption measured in this arrangement ranges from 0.5 N_2/e^- to 4 N_2/e^- for electron energy between 50 and 2000 eV, with a blunt peak around 500 eV. The yield is somewhat lower when N_2 is condensed at lower temperature. The temperature was kept systematically at 10 K during electron bombardment of the sample.

The first data are in an excellent agreement with general theoretical assumptions and with former results obtained in similar experiments. Researches most closely related to this thesis present ESD yield values in the order of units of molecules per incident electron measured using two distinct methods of measurements, thus cross-validating the experimental results and proving the quality of commissioning. The agreement is particularly good while accounting for the wide range of orders of magnitude, which is encompassed in measurements related to the vacuum science. Further analysis of the first dataset is ongoing and shows promising preliminary results. These measurements serving for final consolidation of the setup, as well as the data analysis were done in collaboration between the CERN-TE-VSC-VSM section and UPMC, Paris.

7.4 My contribution

As much as this was a collaborative effort of the expert team from TE-VSC-VSM section, particularly in the design phase and during results interpretation, I was given the hands-on opportunity and a large degree of autonomy in this project. This consisted of a piece-wise manual assembly of the entire experimental setup, that includes UHV components and instruments, cryogenics, electro-pneumatic circuits, SCADA system installation, sub-systems characterisation and data analysis. All this was performed in a successive manner detailed in the previous paragraphs.

The project was reported and discussed on a daily basis with the rest of the team. This led to a rapid advancement of the whole project and meeting of target milestones as foreseen. This complex setup was assembled, commissioned and produced first experimental data within 1 year after first components arrived into the laboratory.

7.5 Conclusion of the thesis

Objectives of the thesis have been accomplished. Extensive literature research provided a solid reference for the entire commissioning process of the new setup. The theoretical background behind the ESD phenomena is explained sufficiently for understanding and effective operation of the setup. Its relation to the accelerator science is also outlined to support the applicability of results.

Hardware and instrumentation used within the setup were finally operated at their nominal performance. Characteristics of various instruments and assemblies were measured and used for further automation of the measurement process.

The effectivity of this commissioning process was supported by acquisition of preliminary dataset, that complies with the literature in an outstanding manner. The new setup already serves its fundamental purpose in the scientific expertise of the group and a systematic research is currently ongoing.

The measurement principle and the its essential components and instruments are described to provide a clear understanding of the measurement process and various intervening factors. More detailed description and analysis would be possible, but surely would exceed the range available in the scope of this thesis.

7.6 Application of results and suggestion for further study

The Large Hadron Collider, as well as other parts of the CERN accelerator complex are being continuously upgraded in order to reach higher beam energy and intensity. The dynamic vacuum phenomena is currently one of their main limiting factors. Thus, a thorough understanding of dynamic vacuum and its mitigation is an absolute must, if these resource-demanding machines are to be successfully operated. An effectively operating accelerator storage ring should provide a high energy and high luminosity particle beam to various experiments, allowing them to produce as much high-quality data as possible.

The experimental data produced by this setup should enhance the understanding of materials' behaviour in the harsh conditions within accelerators. These conditions can now be reproduced in the laboratory with precisely controlled parameters, Materials with different surface treatments and coatings can now be tested and qualified for their engineering application. Different parts of the accelerator can be simulated in terms of pressure, temperature, condensate composition and electron energy.

The scientific data which shall be produced by this setup has much broader scientific potential than accelerator physics. For instance, electrons' interaction with material is also essential in electron microscopy or astrophysics.

Proceeding with systematic measurements across materials, coatings, condensate coverages and electron energies is ongoing, justifying the purpose of the setup by production of high-quality scientific data.

8 References

- [1] Baglin, V., Bregliozzi, G., Lanza, G. and Jimenez, J.M., 2011. *Synchrotron radiation in the LHC vacuum system* (No. CERN-ATS-2011-245). Available from: cds.cern.ch/record/1407539?ln=en.
- [2] Arduini, G., Baglin, V., Benedetto, E., Cimino, R., Collier, P., Collins, I., Cornelis, K., Henrist, B., Hilleret, N., Jenninger, B. and Jimenez, M., 2003, May. Present understanding of electron cloud effects in the Large Hadron Collider. In *Particle Accelerator Conference, 2003. PAC 2003. Proceedings of the* (Vol. 3, pp. 1727-1729). IEEE. DOI: 10.1109/PAC.2003.1288650.
- [3] Iadarola, G. and Rumolo, G., 2013. Electron cloud in the CERN accelerators (PS, SPS, LHC). *arXiv preprint arXiv:1309.6795*. Available from: arxiv.org/abs/1309.6795.
- [4] Furman, M.A., 2013. Electron cloud effects in accelerators. *arXiv preprint arXiv:1310.1706*. Available from: arxiv.org/abs/1310.1706.
- [5] Cimino, R., Collins, I.R., Furman, M.A., Pivi, M., Ruggiero, F., Rumolo, G. and Zimmermann, F., 2004. Can low-energy electrons affect high-energy physics accelerators?. *Physical review letters*, 93(1), p.014801. DOI: 10.1103/PhysRevLett.93.014801
- [6] Cimino, R. and Demma, T., 2014. Electron cloud in accelerators. *International Journal of Modern Physics A*, 29(17), p.1430023. DOI: 10.1142/S0217751X1430023
- [7] Rossi, A., 2004. *VASCO (VACuum Stability COde): multi-gas code to calculate gas density profile in a UHV system* (No. LHC-Project-Note-341). Available from: cds.cern.ch/record/728512?ln=sv
- [8] IUPAC. Compendium of Chemical Terminology, 2nd ed. (the "Gold Book"). Compiled by A. D. McNaught and A. Wilkinson. Blackwell Scientific Publications, Oxford (1997). XML on-line corrected version: <http://goldbook.iupac.org> (2006-) created by M. Nic, J. Jirat, B. Kosata; updates compiled by A. Jenkins. ISBN: 0-9678550-9-8. Available from: doi.org/10.1351/goldbook.
- [9] Ramsier, R.D. and Yates Jr, J.T., 1991. Electron-stimulated desorption: principles and applications. *Surface Science Reports*, 12(6-8), pp.246-378. DOI: 10.1016/0167-5729(91)90013-N.
- [10] Menzel, D., 1975. Electron stimulated desorption: Principles and recent developments. *Surface Science*, 47(1), pp.370-383. DOI: 10.1016/0039-6028(75)90301-5.
- [11] Melius, C.F., Noell, J.O. and Stulen, R.H., 1982. A theoretical study of stimulated desorption of protons from transition metal surfaces. *Journal of Vacuum Science and Technology*, 20(3), pp.559-561. DOI: 10.1116/1.571432.
- [12] Redhead, P.A., 1997. The first 50 years of electron stimulated desorption (1918-1968). *Vacuum*, 48(6), pp.585-596. DOI: 10.1016/S0042-207X(97)00030-4.
- [13] Malyshev, O.B., Hogan, B.T. and Pendleton, M., 2014. Effect of surface polishing and vacuum firing on electron stimulated desorption from 316LN stainless steel. *Journal of Vacuum Science & Technology A: Vacuum, Surfaces, and Films*, 32(5), p.051601. DOI: 10.1116/1.4887035.
- [14] Ding, M.Q. and Williams, E.M., 1989. Electron Stimulated Desorption of gases at technological surfaces of aluminium. *Vacuum*, 39(5), pp.463-469. DOI: 10.1016/0042-207X(89)90269-8.
- [15] Billard, F., Hilleret, N. and Vorlaufer, G., 2000. Some results on the electron induced desorption yield of OFHC copper. *Vacuum Technical Note 00-32, CERN*.

- [16] Kúkol'ová, A., 2017. *Experimental study of electronic properties of manganites and electron stimulated desorption*. (Master thesis, Brno, Masaryk U.). Available from: is.muni.cz/th/jg5xp.
- [17] Nishiwaki, M. and Kato, S., 2001. Electron stimulated gas desorption from copper material and its surface analysis. *Applied surface science*, 169, pp.700-705. DOI: 10.1016/S0169-4332(00)00764-9.
- [18] Vorlaufer, G., 2002. *Modification of ultra-high vacuum surfaces using free radicals* (Doctoral dissertation, Vienna, Tech. U.). Available from: cds.cern.ch/record/547706.
- [19] Yin Vallgren, C., 2011. *Low secondary electron yield carbon coatings for electron cloud mitigation in modern particle accelerators* (No. CERN-THESIS-2011-063). CERN. Available from: cds.cern.ch/record/1374938.
- [20] Yin Vallgren, C et al., 2010. Low secondary electron yield carbon coatings for electron cloud mitigation in modern particle accelerators. IPAC 2010. Available from: cds.cern.ch/record/1309161.
- [21] Benvenuti, C., Chiggiato, P., Cicoira, F. and Ruzinov, V., 1998. Decreasing surface outgassing by thin film getter coatings. *Vacuum*, 50(1-2), pp.57-63. DOI: 10.1016/S0042-207X(98)00017-7.
- [22] Malyshev, O.B., Valizadeh, R., Hogan, B.T. and Hannah, A.N., 2014. Electron-stimulated desorption from polished and vacuum fired 316LN stainless steel coated with Ti-Zr-Hf-V. *Journal of Vacuum Science & Technology A: Vacuum, Surfaces, and Films*, 32(6), p.061601. DOI: 10.1116/1.4897932.
- [23] Le Pimpec, F. (2000). *Etude de la désorption moléculaire induite par transitions électroniques dans les surfaces techniques* (Doctoral dissertation, Paris U., VI-VII). Available from: www.researchgate.net/publication/41215984.
- [24] Malyshev, O.B. and Naran, C., 2012. Electron stimulated desorption from stainless steel at temperatures between– 15 and+ 70° C. *Vacuum*, 86(9), pp.1363-1366. DOI: 10.1016/j.vacuum.2012.01.002.
- [25] Gómez-Goñi, J. and Mathewson, A.G., 1997. Temperature dependence of the electron induced gas desorption yields on stainless steel, copper and aluminum. *Journal of Vacuum Science & Technology A: Vacuum, Surfaces and Films*, 15(6), pp.3093-3103. DOI: 10.1116/1.580852.
- [26] Malyshev, O.B., Jones, R.M., Hogan, B.T. and Hannah, A., 2013. Electron stimulated desorption from the 316 L stainless steel as a function of impact electron energy. *Journal of Vacuum Science & Technology A: Vacuum, Surfaces, and Films*, 31(3), p.031601. DOI: 10.1116/1.4798256.
- [27] Malyshev, O.B., Smith, A.P., Valizadeh, R. and Hannah, A., 2011. Electron stimulated desorption from aluminium alloy and aluminium coated stainless steel. *Vacuum*, 85(12), pp.1063-1066. DOI: 10.1016/j.vacuum.2011.01.028.
- [28] Tratnik, H., 2005. *Electron stimulated desorption of condensed gases on cryogenic surfaces* (No. CERN-THESIS-2006-038). Available from: cds.cern.ch/record/976630.
- [29] Tratnik, H., Hilleret, N. and Störi, H., 2007. The desorption of condensed noble gases and gas mixtures from cryogenic surfaces. *Vacuum*, 81(6), pp.731-737. DOI: 10.1016/j.vacuum.2005.11.064.
- [30] Kuzucan, A., Neupert, H., Tadorelli, M. and Störi, H., 2012. Secondary electron yield on cryogenic surfaces as a function of physisorbed gases. *Journal of Vacuum Science & Technology A: Vacuum, Surfaces, and Films*, 30(5), p.051401. DOI: 10.1116/1.4736552.

- [31] Neupert, H., Tadorelli, M., Kuzucan, A. and Stoeri, H., 2011. Secondary Electron Yield on Cryogenic Surfaces as a Function of Physisorbed Gases. In *Conf. Proc.* (Vol. 110904, No. IPAC-2011-TUPS023, pp. 1575-1577). Available from: accelconf.web.cern.ch/AccelConf/IPAC2011/papers/tups023.pdf.
- [32] Kuzucan, A., 2011. Secondary Electron Yield on Cryogenic Surfaces as a Function of Physisorbed Gases Asena (Vienna, Tech. U.; CERN). Available from: cds.cern.ch/record/1374182.
- [33] Schou, J., Tratnik, H., Thestrup, B. and Hilleret, N., 2008. Desorption of cryogenic layers of the solid hydrogens by electron bombardment: The role of the metal substrate. *Surface Science*, 602(20), pp.3172-3176. DOI: 10.1016/j.susc.2007.06.081.
- [34] Ellegaard, O., Schou, J., Sørensen, H. and Børgesen, P., 1986. Electronic sputtering of solid nitrogen and oxygen by keV electrons. *Surface science*, 167(2-3), pp.474-492. DOI: 10.1016/0039-6028(86)90718-1.
- [35] Ellegaard, O., Pedrys, R., Schou, J., Sørensen, H. and Børgesen, P., 1988. Sputtering of solid argon by keV electrons. *Applied Physics A*, 46(4), pp.305-312. DOI: 10.1007/BF01210351.
- [36] Schou, J., 1991. Erosion of Volatile Elemental Condensed Gases by keV Electron and Light-Ion Bombardment. Available from: orbit.dtu.dk/files/53858874/ris_r_591.pdf.
- [37] Svendsen, W., Thestrup, B., Schou, J. and Ellegaard, O., 1995. Sputtering of thin and intermediately thick films of solid deuterium by keV electrons. *Nuclear Instruments and Methods in Physics Research Section B: Beam Interactions with Materials and Atoms*, 101(1-2), pp.174-178. DOI: 10.1016/0168-583X(95)00300-2.
- [38] Outlaw, R.A., Peregoy, W.K., Hoflund, G.B. and Corallo, G.R., 1987. Electron stimulated desorption of atomic oxygen from silver. DOI: 10.1016/0169-4332(87)90125-5.
- [39] Arakawa, I. and Tuzi, Y., 1984. Desorption of physisorbed and condensed gases on cold surfaces by electron irradiation. *Journal of Nuclear Materials*, 128, pp.779-783. DOI: 10.1016/0022-3115(84)90456-2.
- [40] Adachi, T., Hirayama, T., Miura, T., Arakawa, I. and Sakurai, M., 2003. Absolute measurements of the total PSD and ESD yields at the surface of solid krypton. *Surface Science*, 528(1-3), pp.60-66. DOI: 10.1016/S0039-6028(02)02611-0.
- [41] Sieger, M.T. and Orlando, T.M., 1997. Effect of surface roughness on the electron-stimulated desorption of D⁺ from microporous D₂O ice. *Surface science*, 390(1-3), pp.92-96. DOI: 10.1016/S0039-6028(97)00523-2.
- [42] Sieger, M.T. and Orlando, T.M., 2000. Probing low-temperature water ice phases using electron-stimulated desorption. *Surface science*, 451(1-3), pp.97-101. DOI: 10.1016/S0039-6028(00)00013-3.
- [43] Grieves, G.A. and Orlando, T.M., 2005. The importance of pores in the electron stimulated production of D₂ and O₂ in low temperature ice. *Surface science*, 593(1-3), pp.180-186. DOI: 10.1016/j.susc.2005.06.059.
- [44] Azria, R., Le Coat, Y., Lachgar, M., Tronc, M., Parenteau, L. and Sanche, L., 1999. Effects of morphology in electron-stimulated desorption: O⁻ from O₂ condensed on D₂O films grown at 15–150 K on Pt. *Surface science*, 436(1-3), pp.L671-L676. DOI: 10.1016/S0039-6028(99)00642-1.

- [45] Azria, R., Le Coat, Y., Lachgar, M., Tronc, M., Parenteau, L. and Sanche, L., 2000. Morphology effects in anion electron-stimulated desorption. *Surface science*, 451(1-3), pp.91-96. DOI: 10.1016/S0039-6028(00)00012-1.
- [46] Tronc, M. and Azria, R., 2001. Role of morphology of D2O ice (20–160 K) in low energy electron stimulated desorption of D⁻ and O⁻ anions, and x-ray photon stimulated desorption of D⁺ cations1. *International Journal of Mass Spectrometry*, 205(1-3), pp.325-331. DOI: 10.1016/S1387-3806(00)00269-4.
- [47] Vichnevetski, E., Bass, A.D. and Sanche, L., 2003. Measuring the porosity of thin films by the electron stimulated desorption of metastable species. *Nuclear Instruments and Methods in Physics Research Section B: Beam Interactions with Materials and Atoms*, 208, pp.210-214. DOI: 10.1016/S0168-583X(03)00651-7.
- [48] Arumainayagam, C.R., Lee, H.L., Nelson, R.B., Haines, D.R. and Gunawardane, R.P., 2010. Low-energy electron-induced reactions in condensed matter. *Surface Science Reports*, 65(1), pp.1-44. DOI: 10.1016/j.surfrep.2009.09.001.
- [49] Bass, A.D. and Sanche, L., 2003. Reactions induced by low energy electrons in cryogenic films. *Low Temperature Physics*, 29(3), pp.202-214. DOI: 10.1063/1.1542441
- [50] Hovington, P., Drouin, D. and Gauvin, R., 1997. CASINO: A new Monte Carlo code in C language for electron beam interaction—Part I: Description of the program. *Scanning*, 19(1), pp.1-14. DOI: 10.1002/sca.4950190101.
- [51] Suga, M., Asahina, S., Sakuda, Y., Kazumori, H., Nishiyama, H., Nokuo, T., Alfredsson, V., Kjellman, T., Stevens, S.M., Cho, H.S. and Cho, M., 2014. Recent progress in scanning electron microscopy for the characterization of fine structural details of nano materials. *Progress in Solid State Chemistry*, 42(1-2), pp.1-21. DOI: 10.1016/j.progsolidstchem.2014.02.001.
- [52] Jiles, D., 2015. *Introduction to magnetism and magnetic materials*. CRC press. ISBN: 9781482238877.
- [53] McMahan, H.O. and Gifford, W.E., 1960. A new low-temperature gas expansion cycle. In *Advances in Cryogenic Engineering* (pp. 354-367). Springer, Boston, MA. DOI: 10.1007/978-1-4757-0537-9_43.
- [54] Weston, G.F., 2013. *Ultrahigh vacuum practice*. Elsevier. ISBN: 9781483103327.
- [55] Jousten, K. ed., 2016. *Handbook of vacuum technology*. John Wiley & Sons. DOI: 10.1002/9783527688265.
- [56] Yates Jr, J.T., 1998. Experimental innovations in surface science. *Springer, New York*, 27, pp.181-0013. ISBN 978-1-4612-7493-3.
- [57] Oerlikon-Leybold Vacuum GmbH. 2017. Fundamentals of Vacuum Technology. Cologne. Available from: www.leybold.com/en/documentation-downloads.
- [58] National Institute of Standards and Technology. 2010. Standard reference database. REFERENCE fluid PROPERTIES (REFPROP). Version 9.0.
- [59] National Institute of Standards and Technology. 2008. Mass Spectral Database. NIST 08 MS and AMDIS Software. Demo version 2.0f.
- [60] Redhead, P.A., 1962. Thermal desorption of gases. *Vacuum*, 12(4), pp.203-211. DOI: 10.1016/0042-207X(62)90978-8.
- [61] Madey, T.E. and Yates Jr, J.T., 1977. Desorption methods as probes of kinetics and bonding at surfaces. *Surface science*, 63, pp.203-231. DOI: 10.1016/0039-6028(77)90339-9.
- [62] King, D.A., 1975. Thermal desorption from metal surfaces: A review. *Surface Science*, 47(1), pp.384-402. DOI: 10.1016/0039-6028(75)90302-7.

- [63] De Jong, A.M. and Niemantsverdriet, J.W., 1990. Thermal desorption analysis: Comparative test of ten commonly applied procedures. *Surface Science*, 233(3), pp.355-365. DOI: 10.1016/0039-6028(90)90649-S.
- [64] Engelhart, D.P., Wagner, R.J., Meling, A., Wodtke, A.M. and Schäfer, T., 2016. Temperature programmed desorption of weakly bound adsorbates on Au (111). *Surface Science*, 650, pp.11-16. DOI: 10.1016/j.susc.2015.06.010.
- [65] Wallén, E., 1996. *Adsorption isotherms of H₂ and mixtures of H₂, CH₄, CO and CO₂ on copper plated stainless steel at 4.2 K and the large hadron collider vacuum system*. Chalmers University of Technology. DOI: 10.1116/1.580245.
- [66] Wallen, E., 1997. Adsorption isotherms of He and H₂ at liquid He temperatures. *Journal of Vacuum Science & Technology A: Vacuum, Surfaces, and Films*, 15(2), pp.265-274. DOI: 10.1116/1.580523.
- [67] Moulard, G., Jenninger, B. and Saito, Y., 2001. Industrial surfaces behaviour related to the adsorption and desorption of hydrogen at cryogenic temperature. *Vacuum*, 60(1-2), pp.43-50. DOI: 10.1016/S0042-207X(00)00244-X.
- [68] Bayard, R.T. and Alpert, D., 1950. Extension of the low pressure range of the ionization gauge. *Review of Scientific Instruments*, 21(6), pp.571-572. DOI: 10.1063/1.1745653.
- [69] Redhead, P.A., 1960. Modulated Bayard-Alpert Gauge. *Review of Scientific Instruments*, 31(3), pp.343-344. DOI: 10.1063/1.1716973
- [70] Redhead, P.A., 1969. The Sensitivity of Bayard-Alpert Gauges. *Journal of Vacuum Science and Technology*, 6(5), pp.848-854. DOI: 10.1116/1.1492719.
- [71] Kimball physics. 2017. ELG-2/EGPS-1022 electron gun and power supply system manual. Wilton, USA.
- [72] Sise, O., Manura, D.J. and Dogan, M., 2008. Exploring focal and aberration properties of electrostatic lenses through computer simulation. *European journal of physics*, 29(6), p.1165. DOI: 10.1088/0143-0807/29/6/005.
- [73] Feynman, R. P., Leighton, R. B., & Sands, M., 1963. *The Feynman lectures on physics, Vol. 1* (Vol. 47). ISBN: 9788131792131.
- [74] Reiser, M., 2008. *Theory and design of charged particle beams*. John Wiley & Sons. DOI: 10.1002/9783527622047.
- [75] Liebl, H., 2008. *Applied charged particle optics* (Vol. 2012). Berlin: Springer. ISBN: 9781420045543.
- [76] Egerton, R.F., 2005. *Physical principles of electron microscopy* (p. 41). New York: Springer. DOI 10.1007/b136495
- [77] Reimer, L., 1998. *Scanning electron microscopy: physics of image formation and microanalysis*. Springer. DOI: 10.1007/978-3-540-38967-5.
- [78] Vegard, L., 1935. The Phosphorescence Process as Revealed by the Luminescence from Solid Nitrogen. *Nature*, 135(3426), p.1073. DOI: 10.1038/1351073a0.

9 List of figures

FIGURE 1. CALCULATED SYNCHROTRON RADIATION SPECTRA FOR LHC DIPOLE MAGNET AT ENERGIES FROM INJECTION TO NOMINAL. IMAGE KINDLY REPRODUCED AFTER V. BAGLIN ET AL. [1].	10
FIGURE 2: SECONDARY ELECTRON YIELD AS A FUNCTION OF INCIDENT ELECTRON ENERGY. THE CU SURFACE EXHIBITS A CONDITIONING EFFECT OF THE ACCUMULATED DOSE OF ELECTRONS. IMAGE CREDIT: [6].	11
FIGURE 3. SCHEME OF BASIC DESORPTION MECHANISMS WITHIN A BEAM TUBE. IMAGE CREDIT: [7].	12
FIGURE 4: IDEALIZED SCHEME OF THE ELECTRON STIMULATED DESORPTION PHENOMENA.	14
FIGURE 5: MEASUREMENT OF THE SAMPLE CURRENT USING A BIAS VOLTAGE AND CURRENT AMPLIFIER.	17
FIGURE 6: A SIMULATION IN CASINO KINDLY REPRODUCED FROM THE WORK OF SUGA ET AL. [51].	23
FIGURE 7: SIMPLIFIED SCHEME OF THE EXPERIMENTAL SETUP: HELIUM COOLED SAMPLE WITH A LAYER OF CONDENSED GAS IS BOMBARDED BY ELECTRONS. DESORBED GAS (GREEN DASHED LINE) IS MEASURED BY THE MASS SPECTROMETER AND BAYARD-ALPERT GAUGE. PUMPING IS DONE BY A TURBOPUMP AND A GETTER.	26
FIGURE 8: VIEW INSIDE OF THE EXPERIMENTAL CHAMBER.	28
FIGURE 9: THE MU-METAL VACUUM CHAMBER DURING ITS INSTALLATION INTO THE SETUP. THE 2 STAGE LOAD-LOCK SYSTEM IS ASSEMBLED ON THE RIGHT SIDE OF THE IMAGE. NOTE THAT FLANGES ARE POSITIONED WITHIN THE CHAMBER IN 4 PRINCIPAL PLANES MARKED B TO E.	29
FIGURE 10: CRYOMANIPULATOR DURING INSTALLATION AND IN PLACE ON TOP OF THE VACUUM CHAMBER.	31
FIGURE 11: PFEIFFER HiPACE80 TURBOMOLECULAR PUMP AND SILVER-COATED GASKET USED IN CF FLANGES.	32
FIGURE 12 : NEXTORR 500: A NEG PUMP COMBINED WITH SMALL ION PUMP. CARTRIDGE FILLED WITH SINTERED METAL PELLETS IS VISIBLE ON THE RIGHT.	33
FIGURE 13: MEASURED PUMP-DOWN CURVE OF THE NEWLY ASSEMBLED SETUP. NOTE THE LOG-LOG SCALE.	34
FIGURE 14: VIEW OF THE EXPERIMENTAL VACUUM CHAMBER DURING BAKEOUT EQUIPMENT INSTALLATION.	35
FIGURE 15: TEMPERATURE PROFILE DURING BAKEOUT AND DEGASSING PLATEAU. NOTE THAT UHV INSTRUMENTS ARE ALWAYS THE HOTTEST PART OF THE WHOLE SETUP TO ENSURE CLEANLINESS.	36
FIGURE 16: EVOLUTION OF PRESSURE AND TEMPERATURE DURING 1 DAY LONG BAKEOUT AT 150 °C. NOTE THE SEMI-LOG SCALE AND THE PRESSURE GAIN OF ROUGHLY 1.7 ORDERS OF MAGNITUDE.	37
FIGURE 17: MASS SCAN BEFORE AND AFTER A BAKEOUT. NOTE THAT THE DOMINANT RESIDUAL GAS IS H ₂ O BEFORE BAKEOUT AND H ₂ AFTERWARDS.	38
FIGURE 18: VIEW OF LHe DEWAR AND CRYOMANIPULATOR WITH A TRANSFER LINE IN BETWEEN.	39
FIGURE 19: PIPING AND INSTRUMENTATION DIAGRAM OF THE OPEN CYCLE LIQUID HELIUM COOLING.	40
FIGURE 20: REFRIGERATION DIAGRAM OF OPEN CYCLE LHe COOLING. ADAPTED FROM NIST REFPROP [58].	41
FIGURE 21: PIPING AND INSTRUMENTATION DIAGRAM OF THE GAS DOSING SYSTEM.	42
FIGURE 22: VACUUM CONDUCTANCE OF A 10.34 MM CIRCULAR ORIFICE CALCULATED FOR DIFFERENT MASSES AND TEMPERATURES.	43
FIGURE 23: VIEW OF RETRACTABLE GAS DOSING SYSTEM APPROACHING CLOSELY ABOVE THE SAMPLE.	46
FIGURE 24: TEMPERATURE PROGRAMMED DESORPTION CURVES MEASURED IN N ₂ ADSORBED ON BAKED CU SURFACE. RATE OF TEMPERATURE RISE IS 10 K/MIN. BACKGROUND SIGNAL WAS SUBTRACTED.	48
FIGURE 25: DETAILED VIEW OF BAYARD-ALPERT IONIZATION GAUGE. NOTE THE FINE FILAMENT IN THE CENTRE.	49
FIGURE 26: SCHEME OF QUADRUPOLE MASS SPECTROMETER IN ITS SIMPLEST ARRANGEMENT. SCHEME ADAPTED FROM LEYBOLD GMBH: FUNDAMENTALS OF VACUUM TECHNOLOGY [57].	51
FIGURE 27: SENSITIVITY OF THE GAUGE AS MEASURED BY ION CURRENT AS A FUNCTION OF SEM VOLTAGE.	52
FIGURE 28: ION CURRENT FOR VARIOUS FRAGMENTS OF N ₂ AS A FUNCTION OF PRESSURE. BACKGROUND SIGNAL WAS SUBTRACTED.	53
FIGURE 29: RGA SPECTRA FOR N ₂ , CO AND CH ₄ . SEM VOLTAGE IS SET TO 1600 V.	54
FIGURE 30: MODULAR EMBEDDED CONTROLLER NI PXIE-8840 USED IN THE SCADA SYSTEM.	55
FIGURE 31: SCHEME OF THE DAQ CHAIN DIRECTLY RELATED TO ESD MEASUREMENTS. DASHED LINES ARE DIGITAL, FULL LINES ANALOGUE, ARROWS MARK THE DIRECTION OF COMMUNICATION.	56
FIGURE 32: THE ELECTRON GUN BEFORE MOUNTING INTO A DN40CF FLANGE OF THE EXPERIMENTAL CHAMBER.	57

FIGURE 33: ELECTRICAL DIAGRAM OF THE ELECTRON GUN. NOTE THE MAIN COMPONENTS AND MULTITUDE OF VOLTAGES TO BE CONTROLLED. SCHEME ADAPTED FROM DEVICE MANUAL BY KIMBALL PHYSICS INC. [71].	58
FIGURE 34: CATHODE TEMPERATURE AS A FUNCTION OF SOURCE CURRENT PASSING THROUGH THE FILAMENT.	59
FIGURE 35: BEAM CURRENT AS A FUNCTION OF GRID VOLTAGE FOR VARIOUS ENERGIES. THE MEASUREMENT WAS DONE WITH AUTOFOCUSING FUNCTION AND ON FARADAY CUP OF THE ELECTRON GUN BIASED TO 48 V.	60
FIGURE 36: BEAM CURRENT AS A FUNCTION OF ELECTRON ENERGY WITH AND WITHOUT BEAM CURRENT LEVELLING. THE MEASUREMENT WAS PERFORMED WITH AUTOFOCUSING.	61
FIGURE 37: ENERGY DEPENDENCE OF VOLTAGES APPLIED TO ELECTROSTATIC OPTICS LEADING TO A FOCUSED BEAM SPOT WITH THE LEAST SIZE POSSIBLE.	62
FIGURE 38.: SCHEME OF ELECTROSTATIC DEFLECTION OF THE ELECTRON BEAM.	63
FIGURE 39: LINEAR DEPENDENCE OF DEFLECTION VOLTAGE VS. DISPLACEMENT FOR A RANGE OF ELECTRON ENERGIES. VALUES ARE CALCULATED FOR NOZZLE-SAMPLE DISTANCE L=60 MM.	64
FIGURE 40: ELECTRON CURRENT MEASURED DURING SCANNING OF THE ELECTRON BEAM BY TWO CONCENTRIC FARADAY CUPS (FC) MOUNTED ON THE MANIPULATOR. THE SIGNAL IS SMOOTHED OVER 2S PERIOD AND ONLY EVER 4 TH DATA-POINT IS DISPLAYED FOR CLARITY.	65
FIGURE 41: COLLECTED CURRENT ON A FARADAY CUP OF THE GUN AS A FUNCTION OF VOLTAGE BIAS OF THE GUN. MEASUREMENT FOR VARIOUS ENERGIES WITH AUTOFOCUSING, WITHOUT CURRENT LEVELLING.	66
FIGURE 42: FRONT PANEL OF LABVIEW GUI SUPPLIED BY THE MANUFACTURER [71] ON THE LEFT. ON THE RIGHT IS THE UPGRADED FRONT PANEL FOR THIS APPLICATION WITH AUTOMATIC FEATURES.	67
FIGURE 43: BLOCK DIAGRAM OF THE LABVIEW GUI OF THE IMPLEMENTED FUNCTIONS. NOTE THE THREE DISTINCT PARTS CONTROLLING THE ELECTRON SOURCE, OPTICS AND DEFLECTION.	68
FIGURE 44: VISUAL VERIFICATION OF ELECTRON GUN AUTOMATIC FOCUSING ACROSS DIFFERENT ENERGIES.	70
FIGURE 45: ELECTRON STIMULATED DESORPTION YIELD OF N ₂ AS A FUNCTION OF ELECTRON ENERGY MEASURED AT 10 K ON 200 ML COVERAGE OF N ₂ CONDENSED ON CU SUBSTRATE AT DIFFERENT TEMPERATURES. THE DATA WAS ACQUIRED AND EVALUATED IN COLLABORATION WITH R. DUPUY, UPMC, PARIS.	72
FIGURE 46: PHOSPHORESCENCE VISIBLE IN 150 ML OF N ₂ ON CU SAMPLE.	73

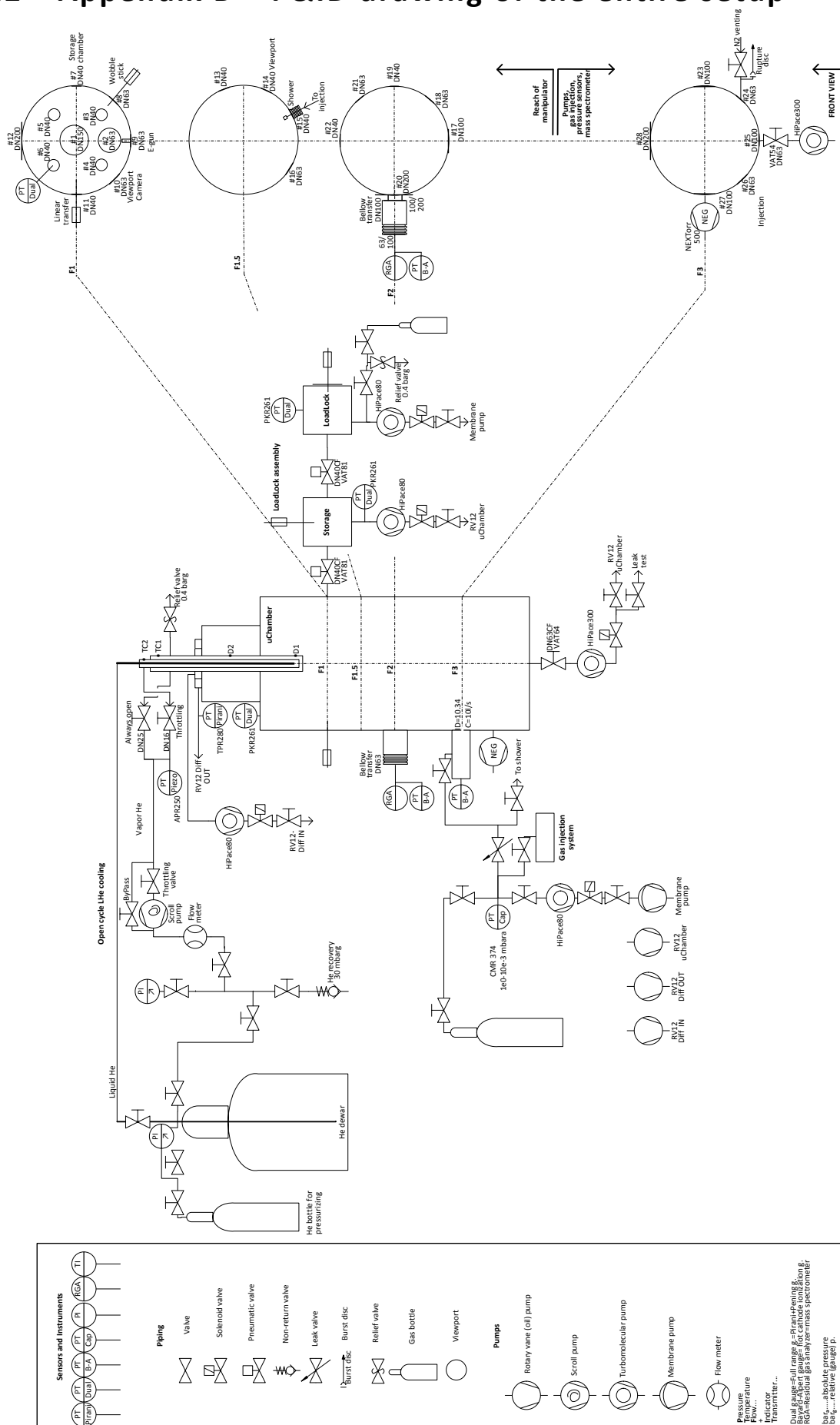
10 List of tables

TABLE 1. TARGET PROCESS AND DESIGN PARAMETERS OF THE EXPERIMENTAL SETUP.	25
TABLE 2: LIST OF USED BAKEOUT PROGRAMS	36
TABLE 3: SENSITIVITY OF THE GAUGE FOR DIFFERENT GASES RELATIVE TO NITROGEN.	50
TABLE 4: MEASURED CRACKING PATTERNS REFERENCED TO NIST MASS SPECTRUM LIBRARY[61].	54
TABLE 5: VOLTAGES GENERATED BY THE EGPS-1022 POWER SUPPLY CONTROLLING THE ELECTRON GUN.	59
TABLE 6: POLYNOMIALS REGRESSED FOR DIFFERENT ENERGY RANGES THAT ARE USED FOR AUTOFOCUSING.	69

11 Appendix A – Enclosed CD

The enclosed CD contains electronic version of this work in *.docx* and *.pdf* formats and processed data stored in *.xls* sheet.

12 Appendix B – P&ID drawing of the entire setup



13 Appendix C – Photograph of entire experimental setup

